TECHNISCHE UNIVERSITÄT WIEN
Vienna University of Technology

HEPHY
Institut für Hochenergiephysik

DISSERTATION

Quark Flavour Violating Decays in Supersymmetry

Ausgeführt zum Zwecke der Erlangung des akademischen Grades eines Doktors der Naturwissenschaften unter der Leitung von

Univ. Prof. Dr. Walter Majerotto
E136
Institut für Theoretische Physik
und
Institut für Hochenergiephysik der ÖAW

eingereicht an der Technischen Universität Wien
Fakultät für Physik

von

DI Sebastian Frank
9756154
Beatrixgasse 5/17, A-1030 Wien
sebastian.frank@oeaw.ac.at

Wien, Mai 2014

For Pınar and Julia Mina

0.1 Abstract

Extensions of the Standard Model (SM) of elementary particle physics like the Minimal Supersymmetric Standard Model (MSSM) can potentially contain new sources of quark flavour violation (QFV). Since these possible non-minimal QFV effects can influence various MSSM particle decays they can have a significant impact on MSSM particle searches at the Large Hadron Collider (LHC), among other things. Thus calculating these general QFV decays with high precision is necessary.

In this thesis we calculate for the first time all squark and gluino two-body decay widths in the MSSM with general QFV at full one-loop level. We follow the SPA convention using the $\overline{\text{DR}}$ renormalisation scheme and include soft and hard photon/gluon bremsstrahlung to our decays. Based on our calculations we develop the first publicly available program package called FVSFOLD (Flavour Violating Squark Full One Loop Decays), which computes automatically all aforementioned non-minimal QFV decays at full one-loop level and uses the SLHA2 input/output format. We present a case study consisting of two scenarios to demonstrate the QFV functionality and usefulness of our code by comparing our full one-loop results with our supersymmetric-QCD (SUSY-QCD) and tree-level calculations and with the results from the program SPheno. In both scenarios we assume non-minimal QFV mixing between the second and third up-type squark generations and take the most important experimental constraints into account. We obtain significant deviations of decay widths and branching ratios from the quark flavour conserving case up to $\sim 54\%$ ($\sim 23\%$) in squark (gluino) decays, depending on the QFV parameters. Moreover, we observe that the electroweak contributions can become even larger than the SUSY-QCD corrections (sometimes with opposite sign) and thus cannot be neglected. We conclude that it is important to account for possible non-minimal QFV effects in squark and gluino decays since they can have an influence on the squark and gluino searches at the LHC. Furthermore, it is necessary to include also electroweak corrections when calculating these QFV decays to attain an adequate accuracy.

We further present an additional aspect of QFV decays by studying the uncertainties in the calculation of the rare B meson decay $\overline{B} \to X_s \gamma$ (an important constraint for general studies of the MSSM). In particular, we assess the uncertainties caused by different implementations via a numerical study comparing various public codes within the phenomenological MSSM (pMSSM). The impact of these uncertainties on global parameter fits of the pMSSM is explored via a global Bayesian analysis using Markov Chain Monte Carlo (MCMC) techniques. We obtain relative differences of the various BR($\overline{B} \to X_s \gamma$) MSSM predictions of $\sim 10\%$. When comparing the SUSY contributions alone the relative differences drop down to $\sim 3\%$, since the discrepancies in the SM predictions are quite large. When comparing programs with similar implementations we observe that the impact on global fits of the pMSSM is rather small (i.e. probability predictions differ only slightly).

0.2 Zusammenfassung

Erweiterungen des Standardmodells (SM) der Elementarteilchenphysik wie dem Minimal Supersymmetrischen Standardmodell (MSSM) können prinzipiell neue Quellen für Quark-Flavour-Verletzungen (QFV) enthalten. Da diese möglichen nicht-minimalen QFV Effekte verschiedene MSSM Teilchenzerfälle beeinflussen können, können sie unter anderem einen erheblichen Einfluss auf die Suche nach MSSM Teilchen am Large Hadron Collider (LHC) haben. Deshalb ist die Berechnung dieser allgemeinen QFV Zerfälle mit hoher Genauigkeit notwendig.

Wir berechnen in dieser Doktorarbeit zum ersten Mal alle Squark und Gluino Zweikörperzerfallsbreiten im MSSM mit allgemeiner QFV auf vollem Einschleifenniveau. Wir berücksichtigen die SPA Konvention, benutzen das $\overline{\text{DR}}$ Renormierungsschema und beziehen die weichen und harten Photon/Gluon-Bremsstrahlungsprozesse mit ein. Basierend auf unseren Berechnungen entwickeln wir das erste öffentlich verfügbare Programmpaket namens FVSFOLD (Flavour Violating Squark Full One Loop Decays), welches automatisch alle bereits erwähnten nicht-minimalen QFV Zerfälle auf vollem Einschleifenniveau berechnet und dabei das SLHA2 Eingabe-/Ausgabeformat benutzt. Wir präsentieren eine Fallstudie bestehend aus zwei Szenarien, um die QFV Funktionalität und Nützlichkeit unseres Programms anhand eines Vergleichs unseres kompletten Einschleifenresultats mit unseren supersymmetrischen-QCD (SUSY-QCD) und Born Resultaten sowie mit den Ergebnissen des Programms SPheno zu demonstrieren. In beiden Szenarien nehmen wir eine nicht-minimale QFV Mischung zwischen der zweiten und dritten Squark-Generation an und berücksichtigen die wichtigsten experimentellen Einschränkungen. Wir erhalten signifikante Abweichungen bei Zerfallsbreiten und Verzweigungsverhältnissen von dem Fall mit Quark-Flavour-Erhaltung, welche abhängig von den QFV Parametern bis zu $\sim 54\%$ ($\sim 23\%$) bei Squark (Gluino) Zerfällen betragen können. Darüber hinaus beobachten wir, dass die elektroschwachen Beiträge sogar größer als die SUSY-QCD Korrekturen werden können (manchmal mit umgekehrtem Vorzeichen) und man sie somit nicht vernachlässigen kann. Wir schließen daraus, dass es wichtig ist, mögliche nicht-minimale QFV Effekte in Squark und Gluino Zerfällen zu berücksichtigen, da sie einen Einfluss auf die Suche nach Squarks und Gluinos am LHC haben können. Außerdem ist es notwendig, auch die elektroschwachen Korrekturen bei den Berechnungen dieser QFV Zerfälle miteinzubeziehen, um eine angemessene Genauigkeit zu erreichen.

Des Weiteren präsentieren wir einen zusätzlichen Aspekt von QFV Zerfällen, indem wir die Unsicherheiten in der Berechnung des seltenen B-Meson Zerfalls $\overline{B} \to X_s\gamma$ untersuchen. (Dieser Zerfall dient als wichtige Einschränkung für allgemeine Studien des MSSM.) Insbesondere schätzen wir die Unsicherheiten aufgrund der unterschiedlichen Implementierungen mittels einer numerischen Studie ab, welche verschiedene öffentlich verfügbare Programme innerhalb des phenomenologischen MSSM (pMSSM) miteinander vergleicht. Die Auswirkungen dieser Unsicherheiten auf globale Parameterfits des pMSSM werden über eine globale Bayes-Analyse unter Verwendung von Markov-Ketten-Monte-Carlo-Verfahren (MCMC) untersucht. Wir erhalten relative Unterschiede der verschiedenen BR($\overline{B} \to X_s\gamma$) MSSM Berechnungen von $\sim 10\%$. Beim Vergleich der alleinigen SUSY-Beiträge fallen die relativen Unterschiede auf $\sim 3\%$, da die Unterschiede in den SM Berechnungen recht groß sind. Beim Vergleich von Programmen mit ähnlichen

Implementierungen beobachten wir, dass die Auswirkungen auf globale Parameterfits des pMSSM gering ausfallen (d.h. die Wahrscheinlichkeitsprognosen unterscheiden sich kaum).

0.3 Acknowledgements

Contents

II   Computational uncertainties in public $\mathrm{BR}(\overline{B} \to X_s\gamma)$ codes   61

Chapter 1

General introduction

The study of quark flavour violating (QFV) particle decays is an excellent probe for the flavour structure of the Standard Model (SM) of elementary particle physics and beyond.

In particular is the study of general QFV decays within the promising SM extension called Minimal Supersymmetric Standard Model (MSSM) quite relevant, since its flavour structure can contain possible new QFV sources which can become quite large (despite very strong constraints from experimental data on B mesons). Especially possible non-minimal QFV effects in squark and gluino decays are of importance since they can have a significant influence on the squark and gluino searches at the Large Hadron Collider (LHC). In order to accurately predict any deviations from the flavour conserving MSSM particle decays a precise calculation of these arbitrary QFV decays at full one-loop level is necessary.

In this dissertation we calculate for the first time all squark and gluino two-body decay widths in the MSSM with general QFV at full one-loop level (i.e. including all electroweak corrections). We follow the SPA convention using the $\overline{\text{DR}}$ renormalisation scheme and include soft and hard photon/gluon bremsstrahlung to our processes. Based on our calculations we develop the first publicly available program package in Fortran called FVSFOLD (Flavour Violating Squark Full One Loop Decays), which computes fully automatically all above-mentioned non-minimal QFV decays. We conclude with a case study demonstrating the QFV functionality and usefulness of our code by comparing our full one-loop results with our SUSY-QCD and tree-level calculations and with the results from the program SPheno.

Furthermore, we present an additional aspect of QFV decays by studying the uncertainties in the calculation of the rare B meson decay $\overline{B} \to X_s \gamma$, which is an important constraint for general studies of the MSSM. In particular, we assess the uncertainties caused by different implementations via a numerical study comparing various public codes within the phenomenological MSSM (pMSSM). The impact of these uncertainties on global parameter fits is explored via a global Bayesian analysis using Markov Chain Monte Carlo (MCMC) techniques.

Part I

Quark flavour violating two-body decays at full one-loop level

Chapter 2

Introduction

The Standard Model (SM) of elementary particle physics is an exceptionally successful theory of the currently known particles as well as electroweak and strong forces. However, the are several theoretical and phenomenological problems that cannot be addressed by the SM, resulting in the need to extend the SM to resolve these issues. A very promising extension of the SM is to introduce supersymmetry (SUSY) in the simplest form as Minimal Supersymmetric Standard Model (MSSM), which can solve many of the open problems.

The MSSM introduces many new particles and interactions with a large number of new model parameters. These parameters can induce possible new flavour violating effects which can become quite large (despite very strong constraints from experimental data on B mesons). Especially possible general (i.e. non-minimal) quark flavour violating effects in squark and gluino decays are of importance since they can have an influence on the squark and gluino searches at the Large Hadron Collider (LHC) [1, 2, 3, 4], among other things.

Furthermore, due to the precision measurements done at the LHC and especially at any future linear collider, all calculations of various observables within the MSSM need to be carried out with matching precision. This generally involves the elaborate calculation of radiative corrections at one-loop level and beyond. There are a few program packages and tools available for the computation of various processes at one-loop level in the renormalised flavour conserving MSSM: SFOLD [5] and HFOLD[6] are both program packages for calculating fully automatically all sfermion and all Higgs boson two-body decay widths at full one-loop level within the MSSM. FeynArts [7, 8] and FormCalc [9] are Mathematica tools which – combined – provide the squared matrix element of a given process at full one-loop level within the complex MSSM. GRACE/SUSY-loop [10, 11] is a program package for the automatic calculation of amplitudes of various processes at full one-loop level in the MSSM. SloopS [12, 13] is an automatised program package which computes various processes at one-loop level in the MSSM.

However, there is currently no program package publicly available which provides precision calculations at full one-loop level (i.e. including all electroweak corrections) in the MSSM with general quark flavour violation. This situation was the starting point and the motivation of our work.

In this thesis we calculate for the first time all squark and gluino two-body decay

widths in the MSSM with general quark flavour violation (QFV) at full one-loop level. We follow the SPA convention using the $\overline{\text{DR}}$ renormalisation scheme and include soft and hard photon/gluon bremsstrahlung to our processes. Based on our calculations we develop the first publicly available program package called FVSFOLD (Flavour Violating Squark Full One Loop Decays), which computes fully automatically all above-mentioned QFV decays at full one-loop level and makes use of the SLHA2 input/output format. Furthermore, we present a case study to demonstrate the QFV functionality and general usefulness of our code by comparing our full one-loop results with our SUSY-QCD and tree-level calculations and with the results from the code SPheno.

The work is organised as follows: in Chapter 3 we present the SM and its limitations, introduce SUSY as a possible extension and conclude with supersymmetric Lagrangians. In Chapter 4 we introduce the MSSM along with the relevant mass matrices and their rotation matrices. In Chapter 5 we present the concept of regularisation and renormalisation and derive renormalisation constants needed for our work. Chapter 6 contains our calculation of all squark and gluino two-body decay widths at full one-loop level. In Chapter 7 we present our QFV case study and conclude our results. Appendix A comprises all Feynman diagrams contributing to the exemplary $\tilde{g} \to \tilde{u}_i \, \bar{u}_g$ decay. At last, in Appendix B we provide further details about our program package, its installation and basic usage, and list our extensive checks.

Chapter 3

Supersymmetry

In this chapter we briefly introduce the Standard Model, supersymmetric theories as promising candidates for physics beyond the Standard Model, and supersymmetric Lagrangians.

3.1 The Standard Model and beyond

The Standard Model (SM) of elementary particle physics [14, 15, 16] is a remarkably successful theory of the presently known particles as well as electroweak and strong forces. The SM is a specific quantum field theory, where the gauge group $SU(3)_C \times SU(2)_L \times U(1)_Y$ is spontaneously broken to $SU(3)_C \times U(1)_{EM}$ by the non-vanishing vacuum expectation value (VEV) of the fundamental scalar Higgs field at energies $\mathcal{O}(100\,\mathrm{GeV})$.

The successful discovery of the associated Higgs boson by the CMS [17] and AT-LAS [18] collaboration in July 2012 (with subsequent studies indicating that it is currently a SM-like Higgs boson, see e.g. [19, 20, 21, 22]) with a mass of $m_h = 125.9 \pm 0.4$ GeV [23] and many more experimental results further confirm the SM as a correct description of particle physics at currently accessible energy scales.

Despite these successes there are theoretical and phenomenological issues that the SM cannot address properly [24]:

- *Electroweak symmetry breaking.* In the SM electroweak symmetry breaking is achieved by setting $\mu^2 < 0$ in the Higgs potential $V = \mu^2|h|^2 + \lambda|h|^4$ by hand, which is rather artificial and dissatisfying.

- *Hierarchy problem.* Radiative corrections to the Higgs boson mass are quadratically dependent on the ultraviolet cutoff Λ, leading to a "natural" value of the Higgs mass of $\mathcal{O}(\Lambda)$ instead of ~ 126 GeV. The destabilization of the Higgs mass and the hierarchy of the mass scales can be prevented by fine-tuning the scalar mass-squared parameter of the ultraviolet theory with very high precision, which is considered unnatural.

- *Fermion masses and family structure.* The SM cannot explain the hierarchical values of the quark and lepton masses. Furthermore it does not explain the existence

of three generations of fermions. Since the SM only contains massless, left-handed neutrinos it has to be extended to allow for massive neutrinos and their mixing.

- *Gauge coupling unification.* The idea of grand unified theories (GUTs) is that the gauge couplings undergoing renormalisation group evolution meet at a point at a high energy scale. However, the SM cannot describe gauge coupling unification precisely enough (see e.g. [25]) to connote that it is more than pure chance.

- *Cosmology.* The SM does not provide a viable candidate for the cold dark matter of the universe, nor a viable inflaton. Furthermore, it cannot explain the baryon asymmetry of the universe and does not include the fourth fundamental force, gravity.

As a result, the SM needs to be extended to resolve the aforementioned open problems. One very strong candidate for physics beyond the SM are theories with *low energy supersymmetry.* The main concept behind supersymmetry (SUSY) is a fundamental symmetry between bosons and fermions. In the simplest case, each SM particle obtains a superpartner which differs only in the spin by $1/2$ and is related to the SM particle by a supersymmetry transformation. Not having discovered superpartners yet means that they must have a significant higher mass than their SM partners, which can be explained by breaking SUSY.

Supersymmetric extensions of the SM can solve many of the previously mentioned issues: it provides an explanation of the origin of electroweak symmetry breaking by deriving rather than assuming the "Mexican hat" potential of the Higgs field, its superpartners protect the Higgs mass by (partly) cancelling large radiative corrections coming from heavy particles, it allows for the unification of the gauge couplings at an energy scale $\mathcal{O}(10^{16}\,\mathrm{GeV})$, the lightest stable supersymmetric particle is an ideal nonbaryonic cold dark matter candidate (with its relic density matching the observed amount in the universe), and it may help explain the baryon asymmetry of the universe by providing additional sources of CP violation.

Certainly, these successes may just be remarkable coincidences since there is up to now no direct experimental evidence for SUSY (see for example the experimental SUSY mini review from September 2013 in [23]). However, since the life span of the Large Hadron Collider (LHC) at CERN is expected to end in 2030 (with several planned upgrades in energy and luminosity), the searches for SUSY and other possible extensions of the SM are still in an early stage. It is also important to note that all recent experimental results and especially the discovery of the currently SM-like Higgs boson with its mass of 125.9 GeV are still consistent with many SUSY models.

In our work we use the Minimal Supersymmetric Standard Model (MSSM), a $N = 1$ supersymmetry with the smallest particle content possible. The single-particle states fall into irreducible representations of the SUSY algebra called supermultiplets. Each supermultiplet contains an equal number of fermionic and bosonic degrees of freedom which are called superpartners. There exist in total two possible types of supermultiplets, the so called chiral supermultiplet (consisting of a two-component spin-1/2 Weyl fermion and a complex spin-0 boson) and the gauge supermultiplet (including a spin-1/2 Weyl fermion named gaugino and a spin-1 gauge boson). These particles inhabiting the same

irreducible supermultiplet possess the same mass and are in the same representation of the gauge group. We will provide more details about the MSSM in the next chapter but first briefly introduce the general supersymmetric Lagrangian density and the soft SUSY breaking terms.

3.2 Supersymmetric Lagrangians

We briefly comment on the derivation of the complete Lagrangian $\mathcal{L} = \mathcal{L}_{\text{SUSY}} + \mathcal{L}_{\text{soft}}$ of a realistic and renormalisable supersymmetric theory with the full supersymmetric Lagrangian $\mathcal{L}_{\text{SUSY}}$ as well as the soft supersymmetry breaking Lagrangian $\mathcal{L}_{\text{soft}}$ (for a detailed derivation see [26, 27]), and simply quote the final Lagrangian with a short description of the relevant terms.

The basic approach is always to write down a Lagrangian and derive the appropriate SUSY transformations so that the action is invariant under these transformations. Furthermore, it is important to ensure that the SUSY algebra closes (i.e. the commutator of two SUSY transformations is another symmetry of the theory) on-shell as well as off-shell.

One usually begins with the massless, non-interacting Wess-Zumino model [28] which describes a single chiral supermultiplet. In order to close the SUSY algebra also off-shell one has to add an auxiliary (complex) scalar field F, which is later eliminated using its classical equation of motion. Then one takes a collection of these supermultiplets and adds masses as well as non-gauge interactions to arrive at a general renormalisable (and supersymmetric) interaction Lagrangian $\mathcal{L}_{\text{int}}$. This Lagrangian can be expressed by the superpotential W, a single function which encodes all mass and Yukawa interaction terms. The Lagrangian is further rewritten to define the scalar potential V. Then one adds gauge supermultiplets with auxiliary (real) scalar fields D^a (again to close the SUSY algebra also off-shell), which are later eliminated using their equations of motion like in the F_i case. Adding supersymmetric gauge interactions by replacing ordinary with covariant derivatives in chiral supermultiplets couple the vector bosons in the gauge supermultiplets to the scalars and fermions in the chiral supermultiplets. Finally, one adds additional possible gauge invariant and renormalisable interactions which couple the gauginos in the gauge supermultiplet to the scalars and fermions in the chiral supermultiplets, and arrives at the full supersymmetric Lagrangian $\mathcal{L}_{\text{SUSY}}$.

In order to obtain a phenomenologically realistic theory one further adds general soft SUSY breaking terms in the Lagrangian $\mathcal{L}_{\text{soft}}$ at a low energy scale (since the exact spontaneous SUSY breaking mechanism at high energies is still unknown). Since broken SUSY is still providing a solution to the hierarchy problem it is named "soft" SUSY breaking.

The full SUSY Lagrangian of the complete Lagrangian $\mathcal{L} = \mathcal{L}_{\text{SUSY}} + \mathcal{L}_{\text{soft}}$ takes the

form

$$\begin{aligned}
\mathcal{L}_{\text{SUSY}} =\ & i\psi^{\dagger i}\bar{\sigma}^\mu D_\mu\psi_i + D^\mu\phi^{*i}D_\mu\phi_i - \frac{1}{4}F^a_{\mu\nu}F^{\mu\nu a} + i\lambda^{\dagger a}\bar{\sigma}^\mu D_\mu\lambda^a \\
& -V(\phi,\phi^*) - \frac{1}{2}M^{ij}\psi_i\psi_j - \frac{1}{2}M^*_{ij}\psi^{\dagger i}\psi^{\dagger j} - \frac{1}{2}y^{ijk}\phi_i\psi_j\psi_k - \frac{1}{2}y^*_{ijk}\phi^{*i}\psi^{\dagger j}\psi^{\dagger k} \\
& -\sqrt{2}g\left((\phi^*T^a\psi)\lambda^a + \lambda^{\dagger a}(\psi^\dagger T^a\phi)\right) .
\end{aligned} \tag{3.1}$$

The first line shows the kinetic terms of fermions ψ_i and scalars ϕ_i as well as the self-interaction of gauge fields $F^a_{\mu\nu}$ and the kinetic term of gauginos λ^a. The second line contains the scalar potential V as well as fermion mass M^{ij} and Yukawa coupling y^{ijk} terms derived from the superpotential W. The last line contains additional supersymmetric gauge interactions with gauginos.
The scalar potential reads

$$V(\phi,\phi^*) = W^*_i W^i + \frac{1}{2}\sum_a g^2_a(\phi^*T^a\phi)^2 , \tag{3.2}$$

where we already eliminated the auxiliary fields F_i and D^a using their classical equations of motion. W^i denotes the derivative $W^i = \delta W/\delta\phi_i$ of the superpotential W, which contains the most general case of mass and non-gauge interaction terms of chiral supermultiplets in a single function:

$$W = \frac{1}{2}M^{ij}\phi_i\phi_j + \frac{1}{6}y^{ijk}\phi_i\phi_j\phi_k . \tag{3.3}$$

The associated interaction Lagrangian can be written as

$$\mathcal{L}_{\text{int}} = \left(-\frac{1}{2}W^{ij}\psi_i\psi_j - W^i W^*_i\right) + \text{c.c.} \tag{3.4}$$

with $W^{ij} = \delta^2 W/\delta\phi_i\delta\phi_j$.
Finally, the soft SUSY breaking Lagrangian in its general form at low energy reads

$$\mathcal{L}_{\text{soft}} = -\left(\frac{1}{2}M_a\,\lambda^a\lambda^a + \frac{1}{6}a^{ijk}\phi_i\phi_j\phi_k + \frac{1}{2}b^{ij}\phi_i\phi_j\right) + \text{c.c.} - (m^2)^i_j\phi^{j*}\phi_i \tag{3.5}$$

with gaugino masses M_a, scalar masses $(m^2)^j_i$ and b^{ij}, and couplings of three scalars a^{ijk}.

Chapter 4

The Minimal Supersymmetric Standard Model

In this chapter we introduce the particle spectrum of the Minimal Supersymmetric Standard Model (MSSM) and further present the relevant mass matrices and their rotation matrices needed for our work.

4.1 Particle spectrum

The MSSM expands the particle content of the SM by enlarging the Higgs sector with two complex Higgs doublets and by introducing a superpartner to each particle [26, 27].

Particles and their superpartners are distributed in the chiral and gauge supermultiplets as shown in Table 4.1 and 4.2, with the naming convention adding the prefix "s" (scalar) for spin $= 0$ and the suffix "-ino" for spin $= 1/2$ superpartners to the names of the SM particles.

Names		spin 0	spin 1/2	$SU(3)_C$, $SU(2)_L$, $U(1)_Y$
squarks, quarks	$\tilde{Q}$	$(\widetilde{u}_L \ \ \widetilde{d}_L)$	$(u_L \ \ d_L)$	$(\ \mathbf{3},\ \mathbf{2}\ ,\ \frac{1}{6})$
($\times 3$ families)	$\overline{u}$	$\widetilde{u}_R^*$	$u_R^\dagger$	$(\ \overline{\mathbf{3}},\ \mathbf{1}\ ,\ -\frac{2}{3})$
	$\overline{d}$	$\widetilde{d}_R^*$	$d_R^\dagger$	$(\ \overline{\mathbf{3}},\ \mathbf{1}\ ,\ \frac{1}{3})$
sleptons, leptons	$\tilde{L}$	$(\widetilde{\nu} \ \ \widetilde{e}_L)$	$(\nu \ \ e_L)$	$(\ \mathbf{1},\ \mathbf{2}\ ,\ -\frac{1}{2})$
($\times 3$ families)	$\overline{e}$	$\widetilde{e}_R^*$	$e_R^\dagger$	$(\ \mathbf{1},\ \mathbf{1},\ 1)$
Higgs, higgsinos	H_u	$(H_2^1 \ \ H_2^2)$	$(\widetilde{H}_2^1 \ \ \widetilde{H}_2^2)$	$(\ \mathbf{1},\ \mathbf{2}\ ,\ +\frac{1}{2})$
	H_d	$(H_1^1 \ \ H_1^2)$	$(\widetilde{H}_1^1 \ \ \widetilde{H}_1^2)$	$(\ \mathbf{1},\ \mathbf{2}\ ,\ -\frac{1}{2})$

Table 4.1: Chiral supermultiplets in the MSSM. The spin $= 0$ fields are complex scalars and the spin $= 1/2$ fields are left-handed two-component Weyl fermions.

Names	spin 1/2	spin 1	$SU(3)_C$, $SU(2)_L$, $U(1)_Y$
gluino, gluon	$\widetilde{g}$	g	(**8**, **1**, 0)
winos, W bosons	$\widetilde{\lambda}^{\pm}$ $\widetilde{\lambda}^3$	$W^{\pm}$ W^0	(**1**, **3**, 0)
bino, B boson	$\widetilde{\lambda}'$	B^0	(**1**, **1**, 0)

Table 4.2: Gauge supermultiplets in the MSSM.

Due to spontaneous electroweak symmetry breaking are the mass eigenstates no longer identical to the gauge eigenstates but mixtures of them. As a result one has to account for this mixing of the fields and derive mass matrices, which are then diagonalised by rotation matrices in order to obtain mass eigenstates. In addition, we assume general quark flavour violation (QFV) in the squark sector and derive as well as rotate all relevant mass matrices in the following sections (for detailed derivations see again [26, 27]). In Table 4.3 we present the mass eigenstates and corresponding interaction eigenstates of the new particles introduced by the MSSM.

Names	Spin	P_R	Gauge Eigenstates	Mass Eigenstates
Higgs bosons	0	+1	H_2^0 H_1^0 H_2^+ H_1^-	h^0 H^0 A^0 $H^{\pm}$
squarks	0	−1	$\widetilde{u}_L$ $\widetilde{u}_R$ $\widetilde{c}_L$ $\widetilde{c}_R$ $\widetilde{t}_L$ $\widetilde{t}_R$ $\widetilde{d}_L$ $\widetilde{d}_R$ $\widetilde{s}_L$ $\widetilde{s}_R$ $\widetilde{b}_L$ $\widetilde{b}_R$	$\widetilde{u}_1$ $\widetilde{u}_2$ $\widetilde{u}_3$ $\widetilde{u}_4$ $\widetilde{u}_5$ $\widetilde{u}_6$ $\widetilde{d}_1$ $\widetilde{d}_2$ $\widetilde{d}_3$ $\widetilde{d}_4$ $\widetilde{d}_5$ $\widetilde{d}_6$
sleptons	0	−1	$\widetilde{e}_L$ $\widetilde{e}_R$ $\widetilde{\nu}_e$ $\widetilde{\mu}_L$ $\widetilde{\mu}_R$ $\widetilde{\nu}_\mu$ $\widetilde{\tau}_L$ $\widetilde{\tau}_R$ $\widetilde{\nu}_\tau$	$\widetilde{e}_1$ $\widetilde{e}_2$ $\widetilde{\nu}_e$ $\widetilde{\mu}_1$ $\widetilde{\mu}_2$ $\widetilde{\nu}_\mu$ $\widetilde{\tau}_1$ $\widetilde{\tau}_2$ $\widetilde{\nu}_\tau$
neutralinos	1/2	−1	$\widetilde{\lambda}'$ $\widetilde{\lambda}^3$ $\widetilde{H}_2^2$ $\widetilde{H}_1^1$	$\widetilde{\chi}_1^0$ $\widetilde{\chi}_2^0$ $\widetilde{\chi}_3^0$ $\widetilde{\chi}_4^0$
charginos	1/2	−1	$\widetilde{\lambda}^{\pm}$ $\widetilde{H}_2^1$ $\widetilde{H}_1^2$	$\widetilde{\chi}_1^{\pm}$ $\widetilde{\chi}_2^{\pm}$
gluino	1/2	−1	$\widetilde{g}$	$\widetilde{g}$

Table 4.3: Mass eigenstates and corresponding interaction eigenstates of the additional particles including QFV in the squark sector in the MSSM.

4.2   Squark sector

Within the SM, the only source of quark flavour violation (QFV) stems from the rotation of up-type (down-type) quark interaction eigenstates $q_{L,R}^0$ to their physical mass eigenstates $q_{L,R}$

$$u_L^0 = V_u\,u_L\,, \quad d_L^0 = V_d\,d_L\,, \quad u_R^0 = U_u\,u_R\,, \quad d_R^0 = U_d\,d_R\,, \tag{4.1}$$

causing the charged-current interactions to be proportional to the unitary CKM matrix $V_{\mathrm{CKM}} = V_u^\dagger V_d$. Within the MSSM, the squark interaction eigenstates undergo the same rotations at high energies as their quark partners, so that their charged-current interactions are proportional to the SM CKM matrix as well. However, softly broken SUSY can induce a misalignment of quarks and squarks in flavour space at low energies, rendering the squark mass matrices to effectively become non-diagonal. This general QFV can be conveniently expressed in the super-CKM basis with the Lagrangian

$$\mathcal{L}_{\tilde{q}} = -\tilde{u}_0^\dagger \, \mathcal{M}_{\tilde{u}}^2 \, \tilde{u}_0 - \tilde{d}_0^\dagger \, \mathcal{M}_{\tilde{d}}^2 \, \tilde{d}_0 \,, \tag{4.2}$$

where $\tilde{u}_0 = (\tilde{u}_L, \tilde{c}_L, \tilde{t}_L, \tilde{u}_R, \tilde{c}_R, \tilde{t}_R)$ and $\tilde{d}_0 = (\tilde{d}_L, \tilde{s}_L, \tilde{b}_L, \tilde{d}_R, \tilde{s}_R, \tilde{b}_R)$. The relevant terms for the 6×6 squark mass matrices are derived from the soft SUSY breaking terms and the auxiliary field terms. The matrices read [29, 3]

$$\mathcal{M}_{\tilde{u}}^2 \;=\; \begin{pmatrix} V_{\mathrm{CKM}} \, \hat{M}_{\tilde{Q}}^2 \, V_{\mathrm{CKM}}^\dagger + \hat{m}_u^2 + D_{\tilde{u}\,LL} & v_2 \hat{T}_U^\dagger / \sqrt{2} - \mu \, \hat{m}_u \cot \beta \\[2mm] v_2 \hat{T}_U / \sqrt{2} - \mu^* \, \hat{m}_u \cot \beta & \hat{M}_{\tilde{u}}^2 + \hat{m}_u^2 + D_{\tilde{u}\,RR} \end{pmatrix} \,, \tag{4.3}$$

$$\mathcal{M}_{\tilde{d}}^2 \;=\; \begin{pmatrix} \hat{M}_{\tilde{Q}}^2 + \hat{m}_d^2 + D_{\tilde{d}\,LL} & v_1 \hat{T}_D^\dagger / \sqrt{2} - \mu \, \hat{m}_d \tan \beta \\[2mm] v_1 \hat{T}_D / \sqrt{2} - \mu^* \, \hat{m}_d \tan \beta & \hat{M}_{\tilde{d}}^2 + \hat{m}_d^2 + D_{\tilde{d}\,RR} \end{pmatrix} \,. \tag{4.4}$$

The matrices $\hat{m}_u$ ($\hat{m}_d$) are the diagonal up-type (down-type) quark masses, μ is the higgsino mass, and $\tan \beta = v_2/v_1$ is the ratio of the vacuum expectation values of the two neutral Higgs fields defined as $v_{1,2} = \sqrt{2} \, \langle H_{1,2}^{1,2} \rangle$. In the equations above we introduced the 3×3 matrices (given in the super-CKM basis)

$$\hat{M}_{\tilde{Q}}^2 \equiv V_d^\dagger \, M_{\tilde{Q}}^2 \, V_d \,, \quad \hat{M}_{\tilde{u}}^2 \equiv U_u^\dagger \, M_{\tilde{u}}^{2\,T} \, U_u \,, \quad \hat{M}_{\tilde{d}}^2 \equiv U_d^\dagger \, M_{\tilde{d}}^{2\,T} \, U_d \,, \tag{4.5}$$

$$\hat{T}_U \equiv U_u^\dagger \, T_U^T \, V_u \,, \quad \hat{T}_D \equiv U_d^\dagger \, T_D^T \, V_d \,, \tag{4.6}$$

where the un-hatted $M_{\tilde{Q},\bar{u},\bar{d}}^2$ are the hermitian soft SUSY breaking mass matrices and the un-hatted $T_{U,D}$ are the soft SUSY breaking trilinear coupling matrices (defined as $\mathcal{L}_{\mathrm{soft}} \supset -(T_{U\alpha\beta} \tilde{u}_{R\alpha}^* \tilde{u}_{L\beta} H_2^2 + T_{D\alpha\beta} \tilde{d}_{R\alpha}^* \tilde{d}_{L\beta} H_1^1)$ with $\alpha, \beta = 1, 2, 3$), both given in the interaction basis. The terms $D_{\tilde{q}\,LL,RR}$ are defined as

$$D_{\tilde{q}\,LL} \;=\; \cos 2\beta \, m_Z^2 \left(T_q^3 - Q_q \sin^2 \theta_W \right) \mathbb{1}_3 \,, \tag{4.7}$$

$$D_{\tilde{q}\,RR} \;=\; \cos 2\beta \, m_Z^2 Q_q \sin^2 \theta_W \, \mathbb{1}_3 \,, \tag{4.8}$$

where Q_q and T_q^3 are the electric charge and the third component of the weak isospin of the quarks/squarks, respectively, and θ_W denotes the weak mixing angle. The squark mass matrices are diagonalised by the 6×6 unitary rotation matrices $R^{\tilde{q}}$ ($\tilde{q} = \tilde{u}, \tilde{d}$) such that

$$R^{\tilde{q}} \mathcal{M}_{\tilde{q}}^2 R^{\tilde{q}\dagger} = \mathrm{diag}(m_{\tilde{q}_1}^2, \ldots, m_{\tilde{q}_6}^2) \tag{4.9}$$

with $m_{\tilde{q}_i} < m_{\tilde{q}_j}$ ($i < j$). The physical mass eigenstates $\tilde{q}_i$ are then given by $\tilde{q}_i = R_{ij}^{\tilde{q}} \tilde{q}_{0j}$.

For our case study in Chapter 7 we define the QFV parameters $\delta_{\alpha\beta}^{uLL}$, $\delta_{\alpha\beta}^{uRR}$, $\delta_{\alpha\beta}^{uRL}$, and $\delta_{\alpha\beta}^{uLR}$ ($\alpha, \beta = 1, 2, 3$ denoting the quark flavours u, c, t) for up-type squarks as

$$\delta_{\alpha\beta}^{uLL} = \hat{M}_{\tilde{Q}\alpha\beta}^2 / \sqrt{\hat{M}_{\tilde{Q}\alpha\alpha}^2 \hat{M}_{\tilde{Q}\beta\beta}^2}, \tag{4.10}$$

$$\delta_{\alpha\beta}^{uRR} = \hat{M}_{\tilde{u}\alpha\beta}^2 / \sqrt{\hat{M}_{\tilde{u}\alpha\alpha}^2 \hat{M}_{\tilde{u}\beta\beta}^2}, \tag{4.11}$$

$$\delta_{\alpha\beta}^{uRL} = \delta_{\beta\alpha}^{uLR*} = (v_2/\sqrt{2})\hat{T}_{U\alpha\beta} / \sqrt{\hat{M}_{\tilde{u}\alpha\alpha}^2 \hat{M}_{\tilde{Q}\beta\beta}^2}. \tag{4.12}$$

As an illustrative example, the parameters δ_{23}^{uRR} and δ_{23}^{uRL} characterise the $\tilde{c}_R - \tilde{t}_R$ and $\tilde{c}_R - \tilde{t}_L$ mixing, respectively.

4.3   Neutralino sector

The neutral gauginos $\widetilde{\lambda}'$ and $\widetilde{\lambda}^3$ as well as the neutral higgsinos $\widetilde{H}_1^1$ and $\widetilde{H}_2^2$ mix to form four mass eigenstates called neutralinos. We denote them with $\tilde{\chi}_i^0$ ($i = 1, \ldots, 4$) in the Majorana representation with the convention $m_{\tilde{\chi}_i^0} < m_{\tilde{\chi}_j^0}$ ($i < j$).

The relevant terms for the neutralino mass matrix are obtained from the soft SUSY breaking terms, the SUSY gauge interaction terms and the Yukawa interaction terms (which can be derived from the superpotential). The combined mass term in the basis $\psi^0 = (-i\widetilde{\lambda}', -i\widetilde{\lambda}^3, \widetilde{H}_1^1, \widetilde{H}_2^2)$ reads

$$\mathcal{L}_{\chi^0} = -\frac{1}{2}(\psi^0)^T Y \psi^0 + h.c. \tag{4.13}$$

with the mass matrix

$$Y = \begin{pmatrix} M_1 & 0 & -m_Z s_{\theta_W} c_\beta & m_Z s_{\theta_W} s_\beta \\ 0 & M_2 & m_Z c_{\theta_W} c_\beta & -m_Z c_{\theta_W} s_\beta \\ -m_Z s_{\theta_W} c_\beta & m_Z c_{\theta_W} c_\beta & 0 & -\mu \\ m_Z s_{\theta_W} s_\beta & -m_Z c_{\theta_W} s_\beta & -\mu & 0 \end{pmatrix}, \tag{4.14}$$

using the abbreviations $s_\alpha := \sin\alpha$ and $c_\alpha := \cos\alpha$. M_1 and M_2 are the SUSY breaking mass parameters of the gauginos $\widetilde{\lambda}'$ and $\widetilde{\lambda}^3$, respectively, and the parameter μ denotes the higgsino mass. The matrix is diagonalised using the unitary rotation matrix Z

$$Y_D = Z^* Y Z^{-1} = \text{diag}(m_{\tilde{\chi}_1^0}, m_{\tilde{\chi}_2^0}, m_{\tilde{\chi}_3^0}, m_{\tilde{\chi}_4^0}). \tag{4.15}$$

Applying the rotation matrix Z to the gauge eigenstates ψ_j^0 one obtains the mass eigenstates χ_i^0 and vice versa:

$$\chi_i^0 = Z_{ij}\psi_j^0 \qquad \psi_j^0 = Z_{ij}^*\chi_i^0. \tag{4.16}$$

Finally, we define the neutralinos as Majorana spinors

$$\tilde{\chi}_i^0 = \begin{pmatrix} \chi_i^0 \\ \bar{\chi}_i^0 \end{pmatrix}. \tag{4.17}$$

4.4 Chargino sector

The charged gauginos $\widetilde{\lambda}^{\pm}$ as well as the charged higgsinos $\widetilde{H}_2^1$ and $\widetilde{H}_1^2$ mix to form two mass eigenstates with charge ± 1 called charginos. We denote them with $\tilde{\chi}_i^{\pm}$ ($i = 1, 2$) in the Dirac representation with the convention $m_{\tilde{\chi}_1^{\pm}} < m_{\tilde{\chi}_2^{\pm}}$.

The relevant terms for the chargino mass matrix are obtained from the soft SUSY breaking terms, the SUSY gauge interaction terms and the Yukawa interaction terms (which can be derived from the superpotential). The combined mass term in the basis $\psi^+ = (-i\widetilde{\lambda}^+, \widetilde{H}_2^1)$, $\psi^- = (-i\widetilde{\lambda}^-, \widetilde{H}_1^2)$ reads

$$\mathcal{L}_{\chi^{\pm}} = -\frac{1}{2}(\psi^+ \, \psi^-)^T \cdot \begin{pmatrix} 0 & X^T \\ X & 0 \end{pmatrix} \cdot \begin{pmatrix} \psi^+ \\ \psi^- \end{pmatrix} + h.c. \tag{4.18}$$

with the mass matrix

$$X = \begin{pmatrix} M_2 & \sqrt{2}m_W \sin\beta \\ \sqrt{2}m_W \cos\beta & \mu \end{pmatrix}. \tag{4.19}$$

The matrix is diagonalised using two unitary rotation matrices U and V

$$X_D = U^* X V^{-1} = \text{diag}(m_{\tilde{\chi}_1^{\pm}}, m_{\tilde{\chi}_2^{\pm}}). \tag{4.20}$$

Applying the rotation matrices U and V to the gauge eigenstates $\psi_j^{\pm}$ one obtains the mass eigenstates $\chi_i^{\pm}$ and vice versa:

$$\chi_i^+ = V_{ij}\psi_j^+ \qquad \chi_i^- = U_{ij}\psi_j^- \tag{4.21}$$

$$\psi_j^+ = V_{ij}^*\chi_i^+ \qquad \psi_j^- = U_{ij}^*\chi_i^-. \tag{4.22}$$

Finally, we define the charginos as Dirac spinors

$$\tilde{\chi}_i^+ = \begin{pmatrix} \chi_i^+ \\ \bar{\chi}_i^- \end{pmatrix} \qquad \tilde{\chi}_i^- = \begin{pmatrix} \chi_i^- \\ \bar{\chi}_i^+ \end{pmatrix}. \tag{4.23}$$

Chapter 5

Renormalisation

When calculating higher order radiative corrections to physical observables in quantum field theory one usually encounters ultraviolet (UV) and infrared (IR) divergences. The systematic treatment to cure these divergences is a two-step process called regularisation and renormalisation, which we introduce in this chapter. Ultimately we will provide here a minimal set of 'building blocks' (so called renormalisation constants), which we will use for our calculation of quark flavour violating squark and gluino decays (as well as on-shell masses) at full one-loop level in the following chapter.

5.1   Regularisation

The first crucial step to cure divergences occurring in higher order radiative corrections is to properly define otherwise divergent Feynman integrals over internal loop momenta. This step is called regularisation and should ideally preserve all symmetries (e.g. Poincaré group, gauge invariance, supersymmetry) of the theory. There are two types of divergences which need different regularisation techniques and different second steps to arrive at a physically meaningful result.

The IR divergence arises as soon as a massless particle (photon, gluon) appears in a closed loop, causing the integral to diverge when the loop momentum approaches zero. This can be prevented by introducing a small, nonzero regulator mass for the photon/gluon. The second step consists of adding photon/gluon radiation from the initial and final states (so called bremsstrahlung) to the process so that one obtains an IR convergent result independent of the regulator mass. We provide more details about the soft and hard photon/gluon bremsstrahlung of our decays in Section 6.2.4 and 6.2.5.

The UV divergence arises when the integral diverges because of the integration momentum approaching infinity. Several regularisation procedures have been formulated. For supersymmetric quantum field theories like the MSSM the dimensional reduction regularisation scheme ($\overline{\text{DR}}$) is widely used, because it does not spoil supersymmetry. The $\overline{\text{DR}}$ regularisation scheme [30] lowers the dimension of the integration momenta to $D = 4 - \epsilon$ dimensions and by that renders the Feynman integrals finite. The UV divergences arise as poles in the limit $\epsilon \to 0$. Since all other tensors and vector fields are kept 4-dimensional the number of bosonic and fermionic degrees of freedom in each superfield remains equal and thus supersymmetry is preserved. The second step then

consists of reparameterising the parameters in the Lagrangian to give them a physical meaning. This step is called renormalisation and is covered in detail in the next section.

For the actual calculation of Feynman integrals we use the technique of Passarino-Veltman integrals (PaVe) [31, 32] at one-loop level. A generic one-loop integral can be written as

$$T^N_{\mu_1\dots\mu_M}(p_1,\dots,p_{N-1},m_0,\dots,m_{N-1}) = \frac{(2\pi\mu)^{4-D}}{i\pi^2}\int d^D q$$

$$\frac{q_{\mu_1}\dots q_{\mu_M}}{[q^2 - m_0^2 + i\epsilon][(q+p_1)^2 - m_1^2 + i\epsilon]\dots[(q+p_{N-1})^2 - m_{N-1}^2 + i\epsilon]} \,, \quad (5.1)$$

where N denotes the number of particles in the loop and M the order of the tensor. The mass parameter μ has been introduced to retain the initial dimensionality of the integral. The scalar integrals up to three particles in the loop are defined as

$$
\begin{aligned}
T^1 &= A_0(m_0^2) \,, & (5.2)\\
T^2 &= B_0(p_1^2, m_0^2, m_1^2) \,, & (5.3)\\
T^3 &= C_0(p_1^2, (p_1 - p_2)^2, p_2^2, m_0^2, m_1^2, m_2^2) \,. & (5.4)
\end{aligned}
$$

The tensor integrals ($N \leq 3$ and $M = 1, 2$) are defined via tensor reduction as

$$
\begin{aligned}
A^\mu &= p^\mu A_1 \,, & (5.5)\\
A^{\mu\nu} &= g^{\mu\nu} A_{00} + p^\mu p^\nu A_{11} \,, & (5.6)\\
B^\mu &= p_1^\mu B_1 \,, & (5.7)\\
B^{\mu\nu} &= g^{\mu\nu} B_{00} + p_1^\mu p_1^\nu B_{11} \,, & (5.8)\\
C^\mu &= p_1^\mu C_1 + p_2^\mu C_2 \,, & (5.9)\\
C^{\mu\nu} &= g^{\mu\nu} C_{00} + p_1^\mu p_1^\nu C_{11} + p_2^\mu p_2^\nu C_{22} + (p_1^\mu p_2^\nu + p_2^\mu p_1^\nu) C_{12} \,. & (5.10)
\end{aligned}
$$

The coefficient functions A_1, A_{00}, A_{11}, B_1, B_{00}, B_{11}, C_1, C_2, C_{00}, C_{11}, C_{22}, and C_{12} can be expressed in terms of the scalar integrals A_0, B_0 and C_0. For a detailed analytic derivation and useful relations we refer to [33].

The UV divergence is denoted with the parameter Δ and is defined as

$$\Delta = \frac{2}{\epsilon} - \gamma_E + \ln 4\pi \qquad (5.11)$$

analogue to the modified minimal subtraction scheme ($\overline{\text{MS}}$). The parameter $\gamma_E \sim 0.577216$ is known as the Euler-Mascheroni constant. A listing of all UV divergent parts of these PaVe one-loop integrals can be found in [33].

5.2   Renormalisation of the MSSM

We employ the $\overline{\text{DR}}$ renormalisation scheme at one-loop level, where the tree-level input parameters (masses, fields, and parameters in couplings) in the Lagrangian are UV finite but defined on the scale Q, and where the divergence Δ is set to zero everywhere. As

a result, the tree-level couplings and its parameters therein are exactly defined at the above-mentioned scale and thus do not receive any finite shifts due to loop corrections. The $\overline{\text{DR}}$ masses and fields are then reparameterised to be the scale-independent physical masses and fields (needed for the LSZ reduction formula, see e.g. [34]) via on-shell (OS) renormalisation conditions. Please note that these OS renormalisation conditions within the $\overline{\text{DR}}$ renormalisation scheme are not to be confused with the OS renormalisation scheme itself, where the input parameters in the Lagrangian are UV divergent bare quantities whose divergences are canceled with UV divergent renormalisation constants.

We derive the renormalisation constants (RCs) of the MSSM in detail for scalar particles and for the sfermion sector along the lines of [33]. The RCs for fermions and for the neutralino and chargino sector are briefly quoted from [33, 35]. Since we currently calculate decays into Higgses at tree-level only we omit the RCs of the Higgs sector. For the remaining RCs of the SM we again refer to [33, 35].

5.2.1 Renormalisation of scalars

We begin with the tree-level Lagrangian in the $\overline{\text{DR}}$ renormalisation scheme

$$\mathcal{L}^{\overline{\text{DR}}} = \tilde{f}_i^{*\,\overline{\text{DR}}} \delta_{ij} (\partial_\mu \partial^\mu - m_{\tilde{f}_i}^{2\,\overline{\text{DR}}}) \tilde{f}_j^{\overline{\text{DR}}} \tag{5.12}$$

where the unrenormalised scalar fields $\tilde{f}^{\,\overline{\text{DR}}}$ and masses $m_{\tilde{f}}^{2\,\overline{\text{DR}}}$ are UV finite but implicitly dependent on the scale Q. The field $\tilde{f}$ represents all flavour violating up- and down-type squarks $\tilde{u}_i$ and $\tilde{d}_i$ ($i = 1, \ldots, 6$) as well as all flavour conserving sleptons $\tilde{l}_i$ and $\tilde{\nu}_l$ ($l = e, \mu, \tau$, $i = 1, 2$). Then we reparametrise these fields and masses via multiplicative wave function and mass renormalisation at one-loop level (always implicitly summing over recurring indices):

$$\tilde{f}_j^{\overline{\text{DR}}} = \sqrt{Z_{jk}^{\tilde{f}}} \tilde{f}_k = (\delta_{jk} + \frac{1}{2} \delta Z_{jk}^{\tilde{f}}) \tilde{f}_k , \tag{5.13}$$

$$\tilde{f}_i^{*\,\overline{\text{DR}}} = \tilde{f}_l^* \sqrt{Z_{li}^{\tilde{f}*}} = \tilde{f}_l^* (\delta_{li} + \frac{1}{2} \delta Z_{li}^{\tilde{f}*}) , \tag{5.14}$$

$$m_{\tilde{f}_i}^{2\,\overline{\text{DR}}} = m_{\tilde{f}_i}^2 + \delta m_{\tilde{f}_i}^2 . \tag{5.15}$$

We denote the renormalised (i.e. now scale-independent) fields and masses with $\tilde{f}$ and $m_{\tilde{f}}^2$, respectively. The wave function renormalisation (WFR) constants $\delta Z^{\tilde{f}}$ and the mass renormalisation constants $\delta m_{\tilde{f}}^2$ are both UV finite but scale-dependent and are defined so that they cancel the scale dependence of the $\overline{\text{DR}}$ input parameters and furthermore give the renormalised parameters a physical meaning (see below). Expanding the Lagrangian, keeping the terms up to $\mathcal{O}(\delta Z, \delta m^2)$, taking proper care with all Kronecker deltas and renaming free indices yields

$$\mathcal{L}^{\overline{\text{DR}}} = \tilde{f}_i^* \left[\delta_{ij}(p^2 - m_{\tilde{f}_i}^2) + \frac{1}{2}(p^2 - m_{\tilde{f}_i}^2)\delta Z_{ij}^{\tilde{f}} + \frac{1}{2}(p^2 - m_{\tilde{f}_j}^2)\delta Z_{ij}^{\tilde{f}*} - \delta_{ij}\delta m_{\tilde{f}_i}^2 \right] \tilde{f}_j . \tag{5.16}$$

Now we use the renormalisation ansatz $\mathcal{L}^{\overline{\text{DR}}} = \mathcal{L}^{\text{ren}} + \delta\mathcal{L}$ and define the contribution coming from the selfenergy as $\delta\mathcal{L} = -\tilde{f}_i^* \Pi_{ij}^{\tilde{f}}(p^2) \tilde{f}_j$. Transforming this ansatz and inserting

$\mathcal{L}^{\overline{\mathrm{DR}}}$ and $\delta\mathcal{L}$ results in the renormalised, physical Lagrangian

$$
\begin{aligned}
\mathcal{L}^{\mathrm{ren}} &= \mathcal{L}^{\overline{\mathrm{DR}}} - \delta\mathcal{L} \\
&= \tilde{f}_i^* \Big[\delta_{ij}(p^2 - m_{\tilde{f}_i}^2) \\
&\qquad + \underbrace{\Pi_{ij}^{\tilde{f}}(p^2) + \frac{1}{2}(p^2 - m_{\tilde{f}_i}^2)\delta Z_{ij}^{\tilde{f}} + \frac{1}{2}(p^2 - m_{\tilde{f}_j}^2)\delta Z_{ij}^{\tilde{f}*} - \delta_{ij}\delta m_{\tilde{f}_i}^2}_{\hat{\Pi}_{ij}^{\tilde{f}}(p^2)} \Big] \tilde{f}_j \\
&= \tilde{f}_i^* \Big[\underbrace{\delta_{ij}(p^2 - m_{\tilde{f}_i}^2) + \hat{\Pi}_{ij}^{\tilde{f}}(p^2)}_{\hat{\Gamma}_{ij}^{\tilde{f}}(p^2)} \Big] \tilde{f}_j
\end{aligned}
\tag{5.17}
$$

where we have defined the renormalised selfenergy $\hat{\Pi}_{ij}^{\tilde{f}}$ as well as the renormalised two-point vertex function $\hat{\Gamma}_{ij}^{\tilde{f}}$. By inverting this two-point vertex function we obtain the renormalised propagator $-(\hat{\Gamma}_{ij}^{\tilde{f}})^{-1}$.

We fix the renormalised masses to be the physical, on-shell masses. Since the propagator $-(\hat{\Gamma}_{ij}^{\tilde{f}})^{-1}(p^2)$ has a pole at $p^2 = m_{\tilde{f}\,\mathrm{ph}}^2$, and since we set $m_{\tilde{f}}^2 = m_{\tilde{f}\,\mathrm{ph}}^2$, we arrive at the on-shell renormalisation condition

$$
\widetilde{\mathrm{Re}}\,\hat{\Gamma}_{ij}^{\tilde{f}}(p^2)\Big|_{p^2 = m_{\tilde{f}_j}^2} = 0 \ .
\tag{5.18}
$$

This condition determines all masses and all off-diagonal WFR constants. We introduced the operator $\widetilde{\mathrm{Re}}$ which takes the real part of the PaVe integrals so that the above condition is also fulfilled for unstable particles (which develop an imaginary part in the selfenergy). Now we fix the renormalised fields to be the physical fields. This means that the probability of a scalar propagating from one point to another needs to remain exactly one. In other words, we set the residue of the propagator at the pole to one:

$$
\lim_{p^2 \to m_{\tilde{f}_i}^2} \frac{1}{p^2 - m_{\tilde{f}_i}^2} \widetilde{\mathrm{Re}}\,\hat{\Gamma}_{ii}^{\tilde{f}}(p^2) = 1 \ .
\tag{5.19}
$$

This is the second on-shell renormalisation condition which fixes the remaining diagonal WFR constants.

Inserting $\hat{\Gamma}_{ij}^{\tilde{f}}$ and $\hat{\Pi}_{ij}^{\tilde{f}}$ from Eq. (5.17) into Eq. (5.18) and setting $i = j$ yields the mass renormalisation constants

$$
\delta m_{\tilde{f}_i}^2 = \widetilde{\mathrm{Re}}\,\Pi_{ii}^{\tilde{f}}(m_{\tilde{f}_i}^2) = \widetilde{\mathrm{Re}}\,\Pi_{ii}^{\tilde{f}}(m_{\tilde{f}_i}^{2\,\overline{\mathrm{DR}}}) + \mathcal{O}(\mathrm{two-loop}) \ .
\tag{5.20}
$$

In the last step we substituted the derived on-shell masses $m_{\tilde{f}_i}^2$ with the $\overline{\mathrm{DR}}$ input parameters $m_{\tilde{f}_i}^{2\,\overline{\mathrm{DR}}}$. This replacement is allowed since it produces a discrepancy at two-loop level[1]. If we set $i \neq j$ we obtain the off-diagonal WFR constants

$$
\delta Z_{ij}^{\tilde{f}} = \frac{2}{m_{\tilde{f}_i}^{2\,\overline{\mathrm{DR}}} - m_{\tilde{f}_j}^{2\,\overline{\mathrm{DR}}}} \widetilde{\mathrm{Re}}\,\Pi_{ij}^{\tilde{f}}(m_{\tilde{f}_j}^{2\,\overline{\mathrm{DR}}}) \quad (i \neq j)
\tag{5.21}
$$

---

[1]Since $\Pi_{ii}^{\tilde{f}}$ is calculated at one-loop level, we see by looking at Eq. (5.15) and (5.20) that the difference between $m_{\tilde{f}_i}^2$ and $m_{\tilde{f}_i}^{2\,\overline{\mathrm{DR}}}$ is also at one-loop level. Thus replacing $m_{\tilde{f}_i}^2$ with $m_{\tilde{f}_i}^{2\,\overline{\mathrm{DR}}}$ as the argument of $\Pi_{ii}^{\tilde{f}}$ results in a deviation at two-loop level.

where we used the same mass substitution as before. In order to derive the diagonal WFR constants we expand the diagonal, renormalised selfenergy $\hat{\Pi}_{ii}^{\tilde{f}}$ in a Taylor series around $m_{\tilde{f}_i}^2$:

$$\widetilde{\mathrm{Re}}\,\hat{\Pi}_{ii}^{\tilde{f}}(p^2) = \underbrace{\widetilde{\mathrm{Re}}\,\hat{\Pi}_{ii}^{\tilde{f}}(m_{\tilde{f}_i}^2)}_{=0\ (\mathrm{Eq.}(5.18))} + \frac{\partial}{\partial p^2}\widetilde{\mathrm{Re}}\,\hat{\Pi}_{ii}^{\tilde{f}}(p^2)|_{p^2=m_{\tilde{f}_i}^2}\,(p^2 - m_{\tilde{f}_i}^2) + \mathcal{O}(\mathrm{two-loop})\ . \quad (5.22)$$

Inserting this expansion into Eq. (5.19) and using $\hat{\Gamma}_{ii}^{\tilde{f}}$ as well as $\hat{\Pi}_{ii}^{\tilde{f}}$ from Eq. (5.17) results in the diagonal WFR constants

$$\delta Z_{ii}^{\tilde{f}} = -\widetilde{\mathrm{Re}}\,\dot{\hat{\Pi}}_{ii}^{\tilde{f}}(m_{\tilde{f}_i}^{2\,\overline{\mathrm{DR}}}) \quad (5.23)$$

where we used the abbreviation $\dot{\hat{\Pi}}_{ii}^{\tilde{f}}(m_{\tilde{f}_i}^{2\,\overline{\mathrm{DR}}}) = (\partial \Pi_{ii}^{\tilde{f}}(p^2)/\partial p^2)_{p^2=m_{\tilde{f}_i}^{2\,\overline{\mathrm{DR}}}}$ and the mass substitution as before.

At last, we renormalise the sfermion rotation matrix $R^{\tilde{f}}$ in Section 5.2.3.

5.2.2 Renormalisation of fermions

We reparametrise the $\overline{\mathrm{DR}}$ fermion fields and masses at one-loop level as

$$f_i^{\overline{\mathrm{DR}}} = (\delta_{ij} + \frac{1}{2}\delta Z_{ij}^{f\,L}P_L + \frac{1}{2}\delta Z_{ij}^{f\,R}P_R)f_j\ , \quad (5.24)$$

$$m_{f_i}^{\overline{\mathrm{DR}}} = m_{f_i} + \delta m_{f_i}\ . \quad (5.25)$$

The field f stands for all gluinos $\tilde{g}$, neutralinos $\tilde{\chi}_i^0$, charginos $\tilde{\chi}_i^+$, as well as all (flavour conserving) SM quarks and leptons. Inserting these substitutions into the tree-level Lagrangian $\mathcal{L}^{\overline{\mathrm{DR}}}$, expanding it and taking the renormalisation ansatz $\mathcal{L}^{\overline{\mathrm{DR}}} = \mathcal{L}^{\mathrm{ren}} + \delta\mathcal{L}$ (where $\delta\mathcal{L}$ denotes the contribution coming from the unrenormalised selfenergy Π_{ij}^f) yields the renormalised Lagrangian $\mathcal{L}^{\mathrm{ren}}$. This Lagrangian can be further expressed in terms of the renormalised selfenergy $\hat{\Pi}_{ij}^f$ as well as the renormalised two-point vertex function $\hat{\Gamma}_{ij}^f$

$$\hat{\Gamma}_{ij}^f(p) = \delta_{ij}(\not{p} - m_{f_i}) + \hat{\Pi}_{ij}^f(p)\ , \quad (5.26)$$

$$\hat{\Pi}_{ij}^f(p) = \not{p}P_L\hat{\Pi}_{ij}^{f\,L}(p) + \not{p}P_R\hat{\Pi}_{ij}^{f\,R}(p) + P_L\hat{\Pi}_{ij}^{f,S\,L}(p) + P_R\hat{\Pi}_{ij}^{f,S\,R}(p) \quad (5.27)$$

with the left- and right-handed parts

$$\hat{\Pi}_{ij}^{f\,L/R} = \Pi_{ij}^{f\,L/R} + \frac{1}{2}(\delta Z_{ij}^{f\,L/R} + \delta Z_{ji}^{f\,L/R\dagger})\ , \quad (5.28)$$

$$\hat{\Pi}_{ij}^{f,S\,L/R} = \Pi_{ij}^{f,S\,L/R} - \frac{1}{2}(m_{f_i}\delta Z_{ij}^{f\,L/R} + m_{f_j}\delta Z_{ji}^{f\,R/L\dagger}) - \delta_{ij}m_{f_i}\ . \quad (5.29)$$

We require the on-shell renormalisation conditions to be

$$\widetilde{\mathrm{Re}}\,\hat{\Gamma}_{ij}^f(p)u_j(p)\Big|_{p^2=m_{f_j}^2} = 0\ , \quad (5.30)$$

$$\lim_{p^2\to m_{f_i}^2}\frac{1}{\not{p} - m_{f_i}}\widetilde{\mathrm{Re}}\,\hat{\Gamma}_{ii}^f(p)u_i(p) = u_i(p)\ . \quad (5.31)$$

These conditions determine the mass and wave function renormalisation constants to be

$$
\delta m_{f_i} = \frac{1}{2}\widetilde{\mathrm{Re}}\left(m_{f_i}^{\overline{\mathrm{DR}}}\Big(\Pi_{ii}^{f\,L}(m_{f_i}^{\overline{\mathrm{DR}}})+\Pi_{ii}^{f\,R}(m_{f_i}^{\overline{\mathrm{DR}}})\Big)\right.
$$

$$
\left.+\Pi_{ii}^{f,S\,L}(m_{f_i}^{\overline{\mathrm{DR}}})+\Pi_{ii}^{f,S\,R}(m_{f_i}^{\overline{\mathrm{DR}}})\right)\,,\tag{5.32}
$$

$$
\delta Z_{ij}^{f\,L/R} = \frac{2}{m_{f_i}^{2\,\overline{\mathrm{DR}}}-m_{f_j}^{2\,\overline{\mathrm{DR}}}}\widetilde{\mathrm{Re}}\left(m_{f_j}^{2\,\overline{\mathrm{DR}}}\Pi_{ij}^{f\,L/R}(m_{f_j}^{\overline{\mathrm{DR}}})+m_{f_i}^{\overline{\mathrm{DR}}}m_{f_j}^{\overline{\mathrm{DR}}}\Pi_{ij}^{f\,R/L}(m_{f_j}^{\overline{\mathrm{DR}}})\right.
$$

$$
\left.+m_{f_i}^{\overline{\mathrm{DR}}}\Pi_{ij}^{f,S\,L/R}(m_{f_j}^{\overline{\mathrm{DR}}})+m_{f_j}^{\overline{\mathrm{DR}}}\Pi_{ij}^{f,S\,R/L}(m_{f_j}^{\overline{\mathrm{DR}}})\right)\quad(i\neq j)\,,\tag{5.33}
$$

$$
\delta Z_{ii}^{f\,L/R} = -\widetilde{\mathrm{Re}}\,\Pi_{ii}^{f\,L/R}(m_{f_i}^{\overline{\mathrm{DR}}})+\frac{1}{2m_{f_i}^{\overline{\mathrm{DR}}}}\widetilde{\mathrm{Re}}\left(\Pi_{ii}^{f,S\,L/R}(m_{f_i}^{\overline{\mathrm{DR}}})-\Pi_{ii}^{f,S\,R/L}(m_{f_i}^{\overline{\mathrm{DR}}})\right)
$$

$$
-m_{f_i}^{\overline{\mathrm{DR}}}\widetilde{\mathrm{Re}}\left(m_{f_i}^{\overline{\mathrm{DR}}}\Big(\dot{\Pi}_{ii}^{f\,L/R}(m_{f_i}^{\overline{\mathrm{DR}}})+\dot{\Pi}_{ii}^{f\,R/L}(m_{f_i}^{\overline{\mathrm{DR}}})\Big)\right.
$$

$$
\left.+\dot{\Pi}_{ii}^{f,S\,L/R}(m_{f_i}^{\overline{\mathrm{DR}}})+\dot{\Pi}_{ii}^{f,S\,R/L}(m_{f_i}^{\overline{\mathrm{DR}}})\right)\,,\tag{5.34}
$$

where we substituted the on-shell with the $\overline{\mathrm{DR}}$ mass.

Since we define both SM quarks and leptons to be flavour conserving (i.e. we set the CKM and PMNS matrix diagonal), we only need to renormalise the rotation matrices of the neutralinos and charginos. We perform this renormalisation in Section 5.2.4.

5.2.3   Sfermion sector

We renormalise the sfermion rotation matrix $R^{\tilde{f}\,\overline{\mathrm{DR}}}$ in the $\overline{\mathrm{DR}}$ renormalisation scheme in a similar way to the CKM matrix by starting with the equation

$$
\tilde{f}_j^{I\,\overline{\mathrm{DR}}}=R_{kj}^{\tilde{f}*\,\overline{\mathrm{DR}}}\tilde{f}_k^{\overline{\mathrm{DR}}}\tag{5.35}
$$

which relates the interaction eigenstates $\tilde{f}_j^{I\,\overline{\mathrm{DR}}}$ to the mass eigenstates $\tilde{f}_k^{\overline{\mathrm{DR}}}$. The matrix $R^{\tilde{f}}$ generally denotes both squark and slepton rotation matrices. However, for our quark flavour violating squark and gluino decays we need to focus solely on the 6×6 rotation matrices $R^{\tilde{u}}$ and $R^{\tilde{d}}$ of the flavour violating up- and down-type squarks which we defined in Eq. (4.9). Then we use the following substitutions:

$$
R_{kj}^{\tilde{f}*\,\overline{\mathrm{DR}}} = R_{kj}^{\tilde{f}*}+\delta R_{kj}^{\tilde{f}*}\,,\tag{5.36}
$$

$$
\tilde{f}_k^{\overline{\mathrm{DR}}} = (\delta_{ki}+\frac{1}{2}\delta Z_{ki}^{\tilde{f}})\tilde{f}_i\,.\tag{5.37}
$$

Please note that in the $\overline{\mathrm{DR}}$ scheme the tree-level couplings (and thus also the rotation matrices) are exactly defined at the scale Q, implying that there are no finite shifts. And since the $\overline{\mathrm{DR}}$ renormalisation condition sets the divergence zero ($\Delta=0$) everywhere there are also no divergences in the renormalisation constants. Therefore, $\delta R^{\tilde{f}}$ in Eq. (5.36) is actually zero and its calculation can be omitted. However, we initially keep

$\Delta \neq 0$ and calculate $\delta R^{\tilde{f}}$ since it is a useful possibility to check for RGE invariance of the $\overline{\text{DR}}$ scheme (for more details see the remark in Section 6.2).

We insert these two substitutions into Eq. (5.35) and obtain (for now omitting the $\overline{\text{DR}}$ label to reduce clutter)

$$
\begin{aligned}
\tilde{f}_j^I &= R_{kj}^{\tilde{f}*} \tilde{f}_k \\
&= (R_{kj}^{\tilde{f}*} + \delta R_{kj}^{\tilde{f}*})(\delta_{ki} + \frac{1}{2}\delta Z_{ki}^{\tilde{f}})\tilde{f}_i \\
&= R_{kj}^{\tilde{f}*} \tilde{f}_k + \frac{1}{2}R_{kj}^{\tilde{f}*}\delta Z_{ki}^{\tilde{f}}\tilde{f}_i + \delta R_{ij}^{\tilde{f}*}\tilde{f}_i + \mathcal{O}(\text{two} - \text{loop}) \,.
\end{aligned}
\tag{5.38}
$$

Since every squared matrix can be divided into a hermitian and an anti-hermitian part we take $\delta Z = \frac{1}{2}(\delta Z + \delta Z^{\dagger}) + \frac{1}{2}(\delta Z - \delta Z^{\dagger})$ and arrive at

$$
\begin{aligned}
\tilde{f}_j^I &= R_{kj}^{\tilde{f}*} \tilde{f}_k + \frac{1}{4}R_{kj}^{\tilde{f}*}(\delta Z_{ki}^{\tilde{f}} + \delta Z_{ik}^{\tilde{f}*})\tilde{f}_i + \frac{1}{4}R_{kj}^{\tilde{f}*}(\delta Z_{ki}^{\tilde{f}} - \delta Z_{ik}^{\tilde{f}*})\tilde{f}_i + \delta R_{ij}^{\tilde{f}*}\tilde{f}_i \\
&= \left(R_{kj}^{\tilde{f}*} + \frac{1}{4}R_{ij}^{\tilde{f}*}(\delta Z_{ik}^{\tilde{f}} + \delta Z_{ki}^{\tilde{f}*})\right)\tilde{f}_k + \left(\delta R_{ij}^{\tilde{f}*} + \frac{1}{4}R_{kj}^{\tilde{f}*}(\delta Z_{ki}^{\tilde{f}} - \delta Z_{ik}^{\tilde{f}*})\right)\tilde{f}_i
\end{aligned}
\tag{5.39}
$$

where we swapped the free indices $k \leftrightarrow i$ in the second term of the first line. Now we demand that the rotation of sfermions from interaction to mass eigenstates remains the same at one-loop level. This can be achieved by compensating any additional rotation induced by the WFR constant δZ via δR, i.e. we cancel the anti-hermitian part of δZ with δR and thus set the second term of Eq. (5.39) zero. As a result the renormalisation constant for the sfermion rotation matrix is defined as

$$
\delta R_{ij}^{\tilde{f}} = \frac{1}{4}(\delta Z_{ik}^{\tilde{f}\,\Delta} - \delta Z_{ki}^{\tilde{f}*\,\Delta})R_{kj}^{\tilde{f}\,\overline{\text{DR}}} \,.
\tag{5.40}
$$

Here we denote with δZ^{Δ} that one has to take only the UV divergent part of the WFR constant so that the $\overline{\text{DR}}$ renormalisation condition ($\Delta = 0$ and thus $\delta R^{\tilde{f}} = 0$) is always fulfilled.

5.2.4 Neutralino and chargino sector

We renormalise the neutralino and chargino rotation matrices analogue to the sfermion rotation matrix in Section 5.2.3, i.e. we cancel the anti-hermitian part of the WFR constant with the rotation matrix renormalisation constant. For the neutralino rotation matrix Z defined in Eq. (4.15) we get

$$
\delta Z_{ij} = \frac{1}{4}(\delta Z_{ik}^{\tilde{\chi}^0, L\,\Delta} - \delta Z_{ki}^{\tilde{\chi}^0, L*\,\Delta})Z_{kj}^{\overline{\text{DR}}}
\tag{5.41}
$$

with $k = 1, \dots, 4$ and for the chargino rotation matrices U and V defined in Eq. (4.20) we have

$$
\begin{aligned}
\delta U_{ij} &= (\delta Z_{il}^{\tilde{\chi}^-, L\,\Delta} - \delta Z_{li}^{\tilde{\chi}^-, L*\,\Delta})U_{lj}^{\overline{\text{DR}}} \tag{5.42} \\
\delta V_{ij} &= (\delta Z_{il}^{\tilde{\chi}^-, R*\,\Delta} - \delta Z_{li}^{\tilde{\chi}^-, R\,\Delta})V_{lj}^{\overline{\text{DR}}} \tag{5.43}
\end{aligned}
$$

with $l = 1, 2$. We again take only the UV divergent part of the WFR constants to fulfill the $\overline{\text{DR}}$ renormalisation condition.

Chapter 6

Squark and gluino two-body decays

In this chapter we calculate all squark and gluino two-body decay widths in the MSSM with general quark flavour violation at full one-loop level.[1] Since these decays involve hundreds of Feynman diagrams it is necessary to use tools which (at least partially) automate the generation of the respective amplitudes. We use the Mathematica packages FeynArts 3.7 (FA) [7] for the generation of Feynman diagrams and amplitudes, FormCalc 7.3 (FC) [9] for the further evaluation of these amplitudes and for computing the squared matrix element for a given process, and LoopTools 2.7 (LT) [9] for the evaluation of the Passarino-Veltman (PaVe) one-loop integrals.[2]

Since calculating decays at next-to-leading order lead to UV and IR divergent results we compensate these divergences automatically with our original approach. For this we adopt the SPA convention [36] with the $\overline{\text{DR}}$ renormalisation scheme and use the renormalisation constants (RCs) defined in the previous chapter. To obtain an IR finite result we include soft and hard bremsstrahlung to our decays. Please note that the general quark flavour violation (QFV) in our decays refers to the squark sector only, since we set the Cabibbo-Kobayashi-Maskawa (CKM) matrix diagonal.

Based on our calculations we developed the first publicly available program package `FVSFOLD` (Flavour Violating Squark Full One Loop Decays), which computes fully automatically all above-mentioned QFV decays at full one-loop level (for further details, especially about our original work, see Appendix B).

6.1 Decay patterns

In Table 6.1 we present all possible squark and gluino decays in the MSSM which we implemented in our program. The squark mass indices i, j and the quark generation index g indicate that the decays are quark flavour violating. If the squark decay into a gluino is kinematically allowed it will dominate due to the strong interaction.

---

[1]Currently all decays into Higgses are calculated at tree-level only.

[2]Since FA 3.9 [8] an implementation of the renormalised complex MSSM is now available. However, UV-finite one-loop calculations in that version are still limited to flavour conserving processes.

$\tilde{u}_i$	$\to$	$u_g\, \tilde{\chi}_k^0$	$\tilde{d}_i$	$\to$	$d_g\, \tilde{\chi}_k^0$	$\tilde{g}$	$\to$	$\tilde{u}_i\, \bar{u}_g$
$\tilde{u}_i$	$\to$	$d_g\, \tilde{\chi}_l^+$	$\tilde{d}_i$	$\to$	$u_g\, \tilde{\chi}_l^-$	$\tilde{g}$	$\to$	$\tilde{d}_i\, \bar{d}_g$
$\tilde{u}_i$	$\to$	$u_g\, \tilde{g}$	$\tilde{d}_i$	$\to$	$d_g\, \tilde{g}$			
$\tilde{u}_i$	$\to$	$\tilde{u}_j\, Z^0$	$\tilde{d}_i$	$\to$	$\tilde{d}_j\, Z^0$			
$\tilde{u}_i$	$\to$	$\tilde{d}_j\, W^+$	$\tilde{d}_i$	$\to$	$\tilde{u}_j\, W^-$			
$\tilde{u}_i$	$\to$	$\tilde{u}_j\, h^0$	$\tilde{d}_i$	$\to$	$\tilde{d}_j\, h^0$			
$\tilde{u}_i$	$\to$	$\tilde{u}_j\, H^0$	$\tilde{d}_i$	$\to$	$\tilde{d}_j\, H^0$			
$\tilde{u}_i$	$\to$	$\tilde{u}_j\, A^0$	$\tilde{d}_i$	$\to$	$\tilde{d}_j\, A^0$			
$\tilde{u}_i$	$\to$	$\tilde{d}_j\, H^+$	$\tilde{d}_i$	$\to$	$\tilde{u}_j\, H^-$			

Table 6.1: All possible squark and gluino decays which are implemented in our code. The indices are $i, j = 1, \ldots, 6$, $k = 1, \ldots, 4$, $l = 1, 2$, and $g = 1, 2, 3$.

6.2   Calculation at full one-loop level

We will demonstrate the general procedure of calculating a renormalised two-body decay at full one-loop level by using the $\tilde{g} \to \tilde{u}_i\, \bar{u}_g$ decay as an illustrative example. We start with the tree-level interaction Lagrangian in the $\overline{\text{DR}}$ renormalisation scheme

$$\mathcal{L}_{\tilde{g}\,u\,\tilde{u}}^{\overline{\text{DR}}} = \bar{\tilde{g}}^{\overline{\text{DR}}}(g_L^{\overline{\text{DR}}}P_L + g_R^{\overline{\text{DR}}}P_R)u_g^{\overline{\text{DR}}}\tilde{u}_i^{*\,\overline{\text{DR}}} \tag{6.1}$$

with the coupling matrices

$$g_L^{\overline{\text{DR}}} = -\sqrt{2}\, g_s^{\overline{\text{DR}}} T R_{i\,g}^{\tilde{u}\,\overline{\text{DR}}} \quad \text{and} \quad g_R^{\overline{\text{DR}}} = \sqrt{2}\, g_s^{\overline{\text{DR}}} T R_{i\,g+3}^{\tilde{u}\,\overline{\text{DR}}} \,. \tag{6.2}$$

$g_s^{\overline{\text{DR}}}$ is the strong coupling constant, T denotes the generator of the $SU(3)_C$ group, and $R^{\tilde{u}\,\overline{\text{DR}}}$ is the squark rotation matrix defined in Eq. (4.9). Then we insert the following substitutions due to multiplicative wave function and coupling renormalisation:

$$\tilde{u}_i^{*\,\overline{\text{DR}}} = \tilde{u}_j^*(\delta_{ji} + \frac{1}{2}\delta Z_{ji}^{\tilde{u}*}) \,, \tag{6.3}$$

$$\bar{\tilde{g}}^{\overline{\text{DR}}} = \bar{\tilde{g}}(1 + \frac{1}{2}\delta Z^{\tilde{g}R*}P_L + \frac{1}{2}\delta Z^{\tilde{g}L*}P_R) \,, \tag{6.4}$$

$$u_g^{\overline{\text{DR}}} = (\delta_{gl} + \frac{1}{2}\delta Z_{gl}^{uL}P_L + \frac{1}{2}\delta Z_{gl}^{uR}P_R)u_l \,, \tag{6.5}$$

$$g_{L,R}^{\overline{\text{DR}}} = g_{L,R}^{\overline{\text{DR}}} + \delta g_{L,R}^c \,. \tag{6.6}$$

The wave function renormalisation constants $\delta Z^{\tilde{u}}$, $\delta Z^{\tilde{g}L,R}$, and $\delta Z^{uL,R}$ can be deduced from Section 5.2.1 and 5.2.2. We calculate the coupling counter term $\delta g_{L,R}^c$ (which is actually zero in the $\overline{\text{DR}}$ scheme with $\Delta = 0$, see below) in Section 6.2.2. Expanding the Lagrangian, keeping the terms up to $\mathcal{O}(\delta g, \delta Z)$, using the relations $P_{L,R}^2 = P_{L,R}$ as well

as $P_{L,R}P_{R,L} = 0$, taking proper care with all Kronecker deltas and renaming free indices in the last step yields

$$
\begin{aligned}
\mathcal{L}_{\tilde{g}\,u\,\tilde{u}}^{\overline{\text{DR}}} = {} & \bar{\tilde{g}}\bigg(\Big(g_L^{\overline{\text{DR}}} + \delta g_L^c + \underbrace{\frac{1}{2}(\delta Z^{\tilde{g}R*} + \delta Z_{ij}^{\tilde{u}*} + \delta Z_{lg}^{uL})g_L^{\overline{\text{DR}}}}_{\delta g_L^w} \Big) P_L \\
& + \Big(g_R^{\overline{\text{DR}}} + \delta g_R^c + \underbrace{\frac{1}{2}(\delta Z^{\tilde{g}L*} + \delta Z_{ij}^{\tilde{u}*} + \delta Z_{lg}^{uR})g_R^{\overline{\text{DR}}}}_{\delta g_R^w} \Big) P_R \bigg) u_g \tilde{u}_i^* \ . \quad (6.7)
\end{aligned}
$$

We define the coupling corrections $\delta g_{L,R}^w$ which contain all wave function corrections of our decay.[3] Now we use the renormalisation ansatz $\mathcal{L}^{\overline{\text{DR}}} = \mathcal{L}^{\text{ren}} + \delta\mathcal{L}$ and define the contribution coming from all vertex corrections as

$$
\delta\mathcal{L} = -\delta\mathcal{L}^v = -\bar{\tilde{g}}(\delta g_L^v P_L + \delta g_R^v P_R)u_g \tilde{u}_i^* \ . \quad (6.8)
$$

Transforming this ansatz and inserting Eq. (6.7) and (6.8) results in the renormalised, physical Lagrangian

$$
\begin{aligned}
\mathcal{L}^{\text{ren}} = {} & \mathcal{L}^{\overline{\text{DR}}} - \delta\mathcal{L} \\
= {} & \bar{\tilde{g}}\bigg(\big(g_L^{\overline{\text{DR}}} + \underbrace{\delta g_L^v + \delta g_L^w + \delta g_L^c}_{\Delta g_L} \big) P_L + \big(g_R^{\overline{\text{DR}}} + \underbrace{\delta g_R^v + \delta g_R^w + \delta g_R^c}_{\Delta g_R} \big) P_R \bigg) u_g \tilde{u}_i^* \ (6.9)
\end{aligned}
$$

with the renormalised coupling constants

$$
g_{L,R}^{\text{ren}} = g_{L,R}^{\overline{\text{DR}}}(Q) + \Delta g_{L,R}(Q) \ , \quad (6.10)
$$

defined as the sum of the $\overline{\text{DR}}$ coupling constants $g_{L,R}^{\overline{\text{DR}}}$ and its finite one-loop shifts $\Delta g_{L,R}$ (both at the same scale Q) induced by all vertex and wave function corrections as well as all coupling counter terms. We calculate these coupling corrections $\delta g_{L,R}^v$, $\delta g_{L,R}^w$, and $\delta g_{L,R}^c$ for our specific $\tilde{g} \to \tilde{u}_i\, \bar{u}_g$ decay in the subsequent sections.

Before relating the renormalised interaction Lagrangian $\mathcal{L}^{\text{ren}}$ to the decay width Γ we have to remark on these coupling corrections, on the $\overline{\text{DR}}$ renormalisation scheme and on UV finiteness. Since we are working in the $\overline{\text{DR}}$ scheme (where the divergence Δ is set to zero everywhere) the tree-level couplings $g_{L,R}^{\overline{\text{DR}}}$ are exactly defined at the scale Q and thus do not receive any finite shifts due to loop corrections. As a result, the coupling counter term $\delta g_{L,R}^c$ is zero and its calculation can be omitted. However, we initially keep $\Delta \neq 0$ so that the terms proportional to Δ in $\delta g_{L,R}^c$ as well as in $\delta g_{L,R}^v$ and $\delta g_{L,R}^w$ remain. By keeping all UV divergent parts in all contributions we have a possibility to check for RGE invariance of the $\overline{\text{DR}}$ scheme (i.e. that physical quantities like masses are invariant under RG shifts). Since at one-loop level both the divergence Δ and the (log of the) scale Q always share the same prefactor $\beta(\Delta + \log Q)$, checking for RGE invariance is

---

[3]Please note that this definition is simplified for the sake of brevity and strictly speaking only applies to the case of diagonal wave function corrections δZ. In the case of off-diagonal corrections see Section 6.2.3.

equivalent to showing that $\Delta g_{L,R}$ is UV finite when $\Delta \gg 1$. In our program one can perform this UV check numerically by setting Δ to a very high value (e.g. 10^7 instead of the default zero); the value of the decay width should remain the same except for small numerical deviations $\mathcal{O}(10^{-7})$ (see also Appendix B).

Using $\mathcal{L}^{\text{ren}}$ in Eq. (6.9) of our exemplary $\tilde{g}(k_0) \to \tilde{u}_i(k_1) \bar{u}_g(k_2)$ decay we derive the matrix element $\mathcal{M} = \mathcal{M}_0 + \mathcal{M}_1$ of the process, the sum of the tree-level amplitude and the renormalised one-loop contribution (see Figure 6.1 for a schematic illustration of $\mathcal{M}_1$):

$$\mathcal{M}_0 = i\,\bar{u}(k_0)(g_L^{\overline{\text{DR}}}P_L + g_R^{\overline{\text{DR}}}P_R)v(k_2)\,, \tag{6.11}$$

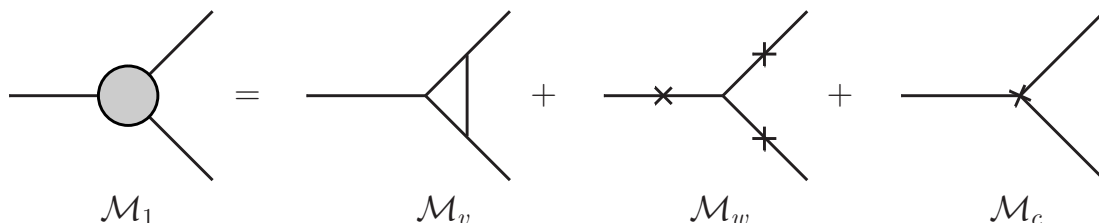$$\mathcal{M}_1 = i\,\bar{u}(k_0)(\Delta g_L P_L + \Delta g_R P_R)v(k_2)\,. \tag{6.12}$$

Figure 6.1: Schematic calculation of a renormalised one-loop contribution to an $1 \to 2$ process, including vertex corrections $\mathcal{M}_v$, wave function corrections $\mathcal{M}_w$ and coupling counter terms $\mathcal{M}_c$. The graph for $\mathcal{M}_w$ is understood as the sum of three diagrams each with a wave function renormalisation constant sitting on an external leg.

Finally, the two-body decay width can be written as

$$\Gamma = \frac{\kappa(m_0^2, m_1^2, m_2^2)N_c}{16\pi m_0^3}\left(|\mathcal{M}_0|^2 + 2\operatorname{Re}(\mathcal{M}_0^\dagger \mathcal{M}_1)\right) \tag{6.13}$$

with the Källen function $\kappa(x,y,z) = \sqrt{(x-y-z)^2 - 4yz}$ and the colour factor N_c. For a fermion-scalar-fermion (FSF) decay we have

$$|\mathcal{M}_0|^2 = (m_0^2 - m_1^2 + m_2^2)(|g_L^{\overline{\text{DR}}}|^2 + |g_R^{\overline{\text{DR}}}|^2) + 2m_0 m_2(g_L^{*\overline{\text{DR}}}g_R^{\overline{\text{DR}}} + g_L^{\overline{\text{DR}}}g_R^{*\overline{\text{DR}}})\,. \tag{6.14}$$

We set for our $\tilde{g} \to \tilde{u}_i \bar{u}_g$ decay the physical on-shell masses $m_0 = m_{\tilde{g}}$, $m_1 = m_{\tilde{u}_i}$, $m_2 = m_{u_g}$ as well as $N_c = 1/8$. We defined the coupling constants already in Eq. (6.2). For the other decay patterns we have for $|\mathcal{M}_0|^2$

$$\text{SSS} \;:\; |g^{\overline{\text{DR}}}|^2\,,$$

$$\text{SSV} \;:\; |g^{\overline{\text{DR}}}|^2\left(m_0^4 - 2m_0^2(m_1^2 + m_2^2) + (m_1^2 - m_2^2)^2\right)/m_2^2\,,$$

$$\text{SFF} \;:\; (m_0^2 - m_1^2 - m_2^2)(|g_L^{\overline{\text{DR}}}|^2 + |g_R^{\overline{\text{DR}}}|^2) - 2m_1 m_2(g_L^{*\overline{\text{DR}}}g_R^{\overline{\text{DR}}} + g_L^{\overline{\text{DR}}}g_R^{*\overline{\text{DR}}})\,. \tag{6.15}$$

This whole procedure of calculating a renormalised $\tilde{g} \to \tilde{u}_i \bar{u}_g$ decay can be straightforwardly used to calculate all other two-body decays listed in Table 6.1.

However, the decay width Γ in Eq. (6.13) is UV finite but still IR divergent. We cancel these IR divergences by adding soft photon/gluon or hard photon/gluon radiation, see Section 6.2.4 and 6.2.5. But first we calculate the coupling corrections $\delta g^v_{L,R}$, $\delta g^c_{L,R}$, and $\delta g^w_{L,R}$.

6.2.1 Vertex corrections

All vertex corrections which contribute to the coupling corrections $\delta g^v_{L,R}$ (see Eq. (6.8)) can be easily calculated within FA/FC. In our exemplary $\tilde{g} \to \tilde{u}_i \bar{u}_g$ decay we have 4 vertex diagrams in SQCD and 11 electroweak vertex diagrams, see Figure A.1 in Appendix A.

6.2.2 Coupling renormalisation

We calculate the coupling renormalisation constants $\delta g^c_{L,R}$ by performing the shift $g^{\overline{\text{DR}}}_{L,R} = g^{\overline{\text{DR}}}_{L,R} + \delta g^c_{L,R}$ in Eq. (6.6) for every parameter which appears in the coupling matrices. That way we reach a set of pre-defined renormalisation constants (RCs) which do not depend on further RCs any more. Then we expand the whole expression and keep the terms linear in the RCs.

Using our gluino decay again as an example, shifting the coupling constants (defined in Eq. (6.2)) along with all occurring parameters, expanding the results and keeping the terms up to $\mathcal{O}(\delta)$ yields

$$
\begin{aligned}
g^{\overline{\text{DR}}}_L &= g^{\overline{\text{DR}}}_L + \delta g^c_L \\
&= -\sqrt{2}\,(g^{\overline{\text{DR}}}_s + \delta g_s)T(R^{\tilde{u}\,\overline{\text{DR}}}_{i\,g} + \delta R^{\tilde{u}}_{i\,g}) \\
&= \underbrace{-\sqrt{2}\,g^{\overline{\text{DR}}}_s T R^{\tilde{u}\,\overline{\text{DR}}}_{i\,g}}_{g^{\overline{\text{DR}}}_L} \underbrace{-\sqrt{2}\,T(\delta g_s R^{\tilde{u}\,\overline{\text{DR}}}_{i\,g} + g^{\overline{\text{DR}}}_s \delta R^{\tilde{u}}_{i\,g})}_{\delta g^c_L} + \mathcal{O}(\delta^2)
\end{aligned}
\tag{6.16}
$$

and analogously

$$
g^{\overline{\text{DR}}}_R = \underbrace{\sqrt{2}\,g^{\overline{\text{DR}}}_s T R^{\tilde{u}\,\overline{\text{DR}}}_{i\,g+3}}_{g^{\overline{\text{DR}}}_R} + \underbrace{\sqrt{2}\,T(\delta g_s R^{\tilde{u}\,\overline{\text{DR}}}_{i\,g+3} + g^{\overline{\text{DR}}}_s \delta R^{\tilde{u}}_{i\,g+3})}_{\delta g^c_R} + \mathcal{O}(\delta^2) \, .
\tag{6.17}
$$

We defined the RC $\delta R^{\tilde{u}}$ in Eq. (5.40). Please note that $\delta g^c_{L,R}$ is exactly zero in the $\overline{\text{DR}}$ scheme but we nevertheless calculate this RC in order to check for RGE invariance / UV finiteness, see the remark in Section 6.2.

We perform this calculation of $\delta g^c_{L,R}$ automatically for every decay via a self-written function in Mathematica within the FA/FC environment. We further define all 'basic' RCs (like the above δg_s and $\delta R^{\tilde{u}}$) which we use as building blocks in a separate Mathematica file, using the file content shown in Appendix B.1 of [35] as a starting point.

6.2.3   Wave function renormalisation

We calculate the coupling corrections $\delta g_{L,R}^{w}$ (defined in Eq. (6.7) for our gluino decay) induced by all wave function corrections separately for diagonal and off-diagonal wave function renormalisation (WFR) constants δZ.

In the diagonal case we have

$$
\delta g_L^{w,\,\text{diag}} \;=\; \frac{1}{2}(\delta Z^{\tilde{g}R*} + \delta Z^{\tilde{u}*}_{ii} + \delta Z^{uL}_{gg})g_L^{\overline{\text{DR}}}\,, \tag{6.18}
$$

$$
\delta g_R^{w,\,\text{diag}} \;=\; \frac{1}{2}(\delta Z^{\tilde{g}L*} + \delta Z^{\tilde{u}*}_{ii} + \delta Z^{uR}_{gg})g_R^{\overline{\text{DR}}}\,. \tag{6.19}
$$

Since the tree-level couplings $g_{L,R}^{\overline{\text{DR}}}$ are the one from our $\tilde{g} \to \tilde{u}_i\,\bar{u}_g$ decay we can directly calculate the amplitude $\mathcal{M}_w^{\text{diag}}$ by substituting the couplings in the tree-level matrix element $\mathcal{M}_0$

$$
\mathcal{M}_w^{\text{diag}} = \mathcal{M}_0(g_{L,R}^{\overline{\text{DR}}} \to \delta g_{L,R}^{w,\,\text{diag}})\,. \tag{6.20}
$$

We implemented a Mathematica routine which automatically generates and inserts these substitutions into the respective tree-level matrix elements of each decay. All relevant WFR constants are defined within a separate counter term Mathematica file (see end of last section) using available FC routines for their calculation. A listing of all contributing diagrams can be found in Figure A.2 in Appendix A.

In the off-diagonal case ($(i \neq j)$ and $(l \neq g)$) we instead have (cf. the simplified version in Eq. (6.7) including the diagonal-only $\delta Z^{\tilde{g}\,L,R*}$)

$$
\delta g_L^{w,\,\text{off-diag}} \;=\; \frac{1}{2}(\delta Z^{\tilde{u}*}_{ij}\,g_L^{j\,\overline{\text{DR}}} + \delta Z^{uL}_{lg}\,g_L^{l\,\overline{\text{DR}}})\,, \tag{6.21}
$$

$$
\delta g_R^{w,\,\text{off-diag}} \;=\; \frac{1}{2}(\delta Z^{\tilde{u}*}_{ij}\,g_R^{j\,\overline{\text{DR}}} + \delta Z^{uR}_{lg}\,g_R^{l\,\overline{\text{DR}}})\,. \tag{6.22}
$$

It is important to note that the tree-level couplings $g_{L,R}^{j\,\overline{\text{DR}}}$ and $g_{L,R}^{l\,\overline{\text{DR}}}$ are *not* the same couplings as in our $\tilde{g} \to \tilde{u}_i\,\bar{u}_g$ decay but the coupling constants of the tree-level decays $\tilde{g} \to \tilde{u}_j\,\bar{u}_g$ and $\tilde{g} \to \tilde{u}_i\,\bar{u}_l$, respectively. In other words, because of the particle transitions induced by $\delta Z^{\tilde{u}*}_{ij}$ (changing $\tilde{u}_i$ with $\tilde{u}_j$) and $\delta Z^{uL,R}_{lg}$ (changing $\bar{u}_g$ with $\bar{u}_l$) we have to deal with different tree-level decay amplitudes and thus cannot use our simple trick in Eq. (6.20) for the off-diagonal case.

We instead use the following approach: we make use of the fact that the off-diagonal WFR constant δZ_{ij} of a particle is related to the real part of its selfenergy Π_{ij}. This can be clearly seen for a scalar particle in Eq. (5.21) but holds true for fermions (see Eq. (5.33)) as well as vector and Higgs bosons as well. We thus simply calculate all 'transition' diagrams where at least one of the external particles undergoes a transition due to its selfenergy. It is straightforward to calculate these diagrams with one-loop selfenergies in FA/FC, and we show all contributing diagrams of our gluino decay in Figure A.3 and A.4. By taking only the real part of the PaVe integrals of these 'transition' graphs we automatically obtain all contributions coming from off-diagonal wave function corrections.

6.2.4 Soft bremsstrahlung

Our squark and gluino two-body decays still suffer from IR divergences which arise as soon as a massless photon/gluon appears in a closed loop. However, these decays are not of any direct physical relevance since one cannot distinguish them experimentally from those involving an additional soft external photon/gluon due to the finite energy resolution of any detector. Adding these so called soft photon/gluon bremsstrahlung from the initial and final states not only renders the decay to be an observable process but also cancels all IR divergences of the original two-body decay [32].

We define the additional photon/gluon to be soft when its energy is below a certain cutoff parameter $|\mathbf{k}| \leq \Delta E$ (for a hard photon/gluon with $|\mathbf{k}| > \Delta E$ see the next section). This cutoff parameter ΔE should be small compared to all energy scales in the process. Furthermore, for the validity of the soft photon/gluon approximation the detector resolution $\Delta E/E$ needs to be sufficiently small. Then it can be shown that the bremsstrahlung diagrams are proportional to the tree-level diagrams [32]. The soft photon/gluon cross section (or equally decay width) reads

$$\left(\frac{d\sigma}{d\Omega}\right)_s = -\left(\frac{d\sigma}{d\Omega}\right)_0 \frac{4\pi\alpha}{(2\pi)^3} \int_{|\mathbf{k}| \leq \Delta E} \frac{d^3k}{2\omega_k} \sum_{ij} \frac{\pm p_i p_j Q_i Q_j}{p_i k p_j k} C_{ij} C_F \qquad (6.23)$$

with $\omega_k = \sqrt{\mathbf{k}^2 + \lambda^2}$, the small regulator mass λ, and $\alpha = \alpha_{em}, \alpha_s$ for the photon/gluon bremsstrahlung. The momentum and (colour) charge of the i-th external particle is p_i and Q_i, respectively, and the $\pm$ sign stems from charges flowing in and out of the diagram. C_{ij} denotes a symmetric 3×3 colour factor matrix which encodes the traces of the respective generators of the $SU(3)_C$ group. For the soft gluon bremsstrahlung of our exemplary $\tilde{g} \to \tilde{u}_i \bar{u}_g$ decay we obtain

$$C = \begin{pmatrix} 12 & 6 & -6 \\ 6 & 16/3 & -2/3 \\ -6 & -2/3 & 16/3 \end{pmatrix} \qquad (6.24)$$

with the overall colour factor $C_F = 3/16 \times 4/3 = 1/4$. (Please note that for the soft photon bremsstrahlung both C and C_F are set to one.) The basic integrals over the photon/gluon phase space

$$I_{ij} = \int_{|\mathbf{k}| \leq \Delta E} \frac{d^3k}{2\omega_k} \frac{2p_i p_j}{p_i k p_j k} \qquad (6.25)$$

can be found in [37]. Finally, adding the soft photon/gluon decay width to the full one-loop two-body decay width results in an IR convergent process, independent of the regulator mass λ so that the limit $\lambda \to 0$ can be safely taken.

6.2.5 Hard bremsstrahlung

Even though soft photon/gluon bremsstrahlung is sufficient to obtain an IR convergent result, the requirements for the soft photon/gluon approximation are often not fulfilled

with realistic detectors due to their bigger resolution $\Delta E/E$. Thus one also has to consider hard photon/gluon bremsstrahlung with $|\mathbf{k}| > \Delta E$.

For each distinct decay pattern (scalar-scalar-scalar, scalar-fermion-fermion, scalar-scalar-vector) of our $1 \rightarrow 2$ squark decays (see Table 6.1) the analytic squared matrix element of the corresponding complete photon/gluon $1 \rightarrow 3$ bremsstrahlung process can be found in [35]. For our gluino decays with its fermion-scalar-fermion structure we briefly derive the according complete (i.e. including both soft and hard) bremsstrahlung process here.

The diagram depicting the bremsstrahlung process of a single photon is shown in Figure 6.2 (for the gluon bremsstrahlung see below). For our exemplary $\tilde{g} \rightarrow \tilde{u}_i \, \bar{u}_g$ decay we have defined the tree-level couplings $g_t^{L,R}$ already in Eq. (6.2). The couplings of the $\gamma \tilde{f} \tilde{f}$- and $\gamma f f$-vertices are defined as $g_i = -eQ_i$ with $e = \sqrt{4\pi\alpha_{em}}$ and the charge Q_i of the particle on leg number $i = 0, 1, 2$. The matrix elements of each single photon

$$\boxed{t} : i(g_t^L P_L + g_t^R P_R)$$
$$\boxed{0} : ig_0\gamma^\mu$$
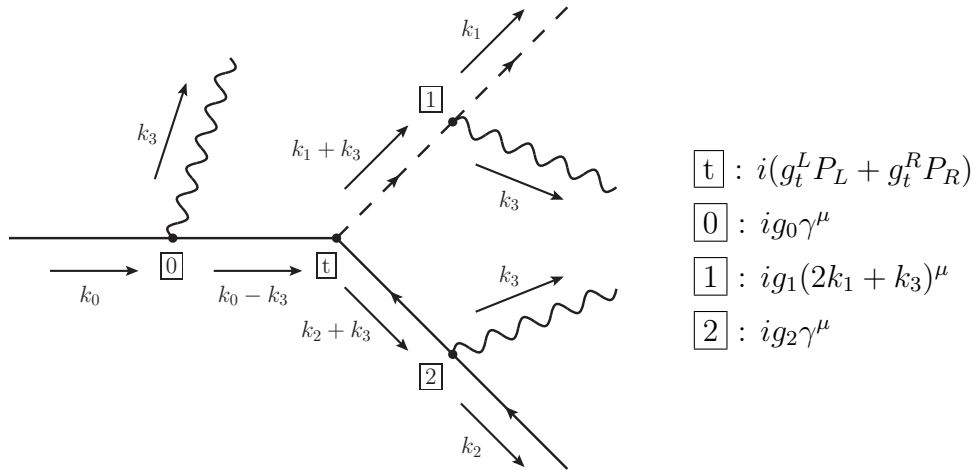$$\boxed{1} : ig_1(2k_1 + k_3)^\mu$$
$$\boxed{2} : ig_2\gamma^\mu$$

Figure 6.2: The combination of three Feynman diagrams showing the $1 \rightarrow 3$ bremsstrahlung process of a single photon from a fermion-scalar-fermion structure.

bremsstrahlung process are

$$\mathcal{M}_0 = \bar{v}(k_0)ig_0\gamma^\mu\epsilon_\mu^*(k_3)\frac{i}{\slashed{k}_0 - \slashed{k}_3 - m_0}i(g_t^L P_L + g_t^R P_R)v(k_2) , \qquad (6.26)$$

$$\mathcal{M}_1 = ig_1(2k_1 + k_3)^\mu\epsilon_\mu^*(k_3)\frac{i}{(k_1 + k_3)^2 - m_1^2}i\bar{v}(k_0)(g_t^L P_L + g_t^R P_R)v(k_2) , \quad (6.27)$$

$$\mathcal{M}_2 = i\bar{v}(k_0)(g_t^L P_L + g_t^R P_R)\frac{i}{\slashed{k}_2 + \slashed{k}_3 - m_2}ig_2\gamma^\mu\epsilon_\mu^*(k_3)v(k_2) . \qquad (6.28)$$

Squaring the sum of these matrix elements, averaging over incoming spins and summing

over outgoing spins results in

$$
\begin{aligned}
\overline{|\mathcal{M}|^2} \;=\; & g_0^2\Big[\left(-2\alpha m_0^2 - 2\beta m_2 m_0\right) I_0 - \alpha I_0^2 \\
& + \left(-2\alpha\left(m_0^2 - m_1^2 + m_2^2\right)m_0^2 - 4\beta m_2 m_0^3\right) I_{00}\Big] \\
& + g_0 g_1\Big[-\alpha I + \left(2\alpha\left(m_1^2 - m_2^2\right) - 2\beta m_0 m_2\right) I_0 \\
& + \left(\alpha\left(-m_0^2 - m_1^2 - m_2^2\right) - 2\beta m_0 m_2\right) I_1 \\
& + \left(2\alpha\left(\left(m_1^2 - m_2^2\right)^2 - m_0^4\right) - 4\beta m_0 m_2\left(m_0^2 + m_1^2 - m_2^2\right)\right) I_{10}\Big] \\
& + g_1^2\Big[\alpha I + \left(\alpha\left(-m_0^2 + 3m_1^2 - m_2^2\right) - 2\beta m_0 m_2\right) I_1 \\
& + \left(-2\alpha\left(m_0^2 - m_1^2 + m_2^2\right)m_1^2 - 4\beta m_0 m_2 m_1^2\right) I_{11}\Big] \\
& + g_0 g_2\Big[-2\alpha I + \left(2\alpha\left(m_1^2 - m_2^2\right) - 2\beta m_0 m_2\right) I_0 \\
& + \left(-2\alpha\left(m_0^2 - m_1^2\right) - 2\beta m_0 m_2\right) I_2 \\
& + \left(-2\alpha\left(m_0^2 - m_1^2 + m_2^2\right)^2 - 4\beta m_0 m_2\left(m_0^2 - m_1^2 + m_2^2\right)\right) I_{20}\Big] \\
& + g_1 g_2\Big[\alpha I + \left(\alpha\left(m_0^2 + m_1^2 + m_2^2\right) + 2\beta m_0 m_2\right) I_1 \\
& + \left(2\alpha\left(m_0^2 - m_1^2\right) + 2\beta m_0 m_2\right) I_2 \\
& + \left(\alpha\left(2m_2^4 - 2\left(m_0^2 - m_1^2\right)^2\right) + 4\beta m_0 m_2\left(-m_0^2 + m_1^2 + m_2^2\right)\right) I_{21}\Big] \\
& + g_2^2\Big[\alpha I + \left(-2\alpha m_2^2 - 2\beta m_0 m_2\right) I_2 + \alpha I_2^1 \\
& + \left(-2\alpha\left(m_0^2 - m_1^2 + m_2^2\right)m_2^2 - 4\beta m_0 m_2^3\right) I_{22}\Big]
\end{aligned}
\tag{6.29}
$$

where we defined $\alpha = |g_t^L|^2 + |g_t^R|^2$ and $\beta = g_t^L g_t^{R*} + g_t^{L*} g_t^R$ for simplicity. I denotes the bremsstrahlung phase space integrals which can be found in [32].

The squared matrix element of the complete gluon bremsstrahlung can be easily derived from the photon bremsstrahlung case in Eq. (6.29) by substituting the couplings

$$
g_i\, g_j \rightarrow g_{si}\, g_{sj}\, C_{ij}
\tag{6.30}
$$

where $g_{si} = -g_s Q_{si}$ with $g_s = \sqrt{4\pi\alpha_s}$ and the colour charge factor $Q_{si} = +1(-1)$ for particles carrying colour (anti-colour). C_{ij} is the colour factor matrix containing the results of the traces of $SU(3)_C$ generators which we already defined in Eq. (6.24) for our $\tilde{g} \rightarrow \tilde{u}_i\, \bar{u}_g$ decay.

Finally, adding the decay width of the complete soft and hard photon/gluon $1 \rightarrow 3$ bremsstrahlung process to the full one-loop two-body decay width results in an IR convergent process, independent of the regulator mass λ and also independent of a cutoff parameter ΔE as opposed to the soft bremsstrahlung case.

Chapter 7

Results and conclusions

In this chapter we present a case study to demonstrate the QFV functionality and general usefulness of our program package FVSFOLD (see Appendix B). We compare our squark and gluino two-body decay widths at full one-loop level with our SUSY-QCD (SQCD) and tree-level calculations and with the results from SPheno 3.2.3 [38, 39]. We present our comparison in tables depicting the decay widths and branching ratios of all squark and gluino decays as well as in various plots as a function of the most important QFV parameters. For the generation of these plots we use the parameter scan functionality of the Mathematica package SSP 1.2.0 (SARAH Scan and Plot) [40].

7.1   Two scenarios for squark and gluino decays

Our case study consists of two scenarios, one for the QFV squark decays and one for the QFV decays of gluinos. In both scenarios we assume general QFV mixing in the second and third up-type squark generations. In all of our results hard bremsstrahlung is included to achieve IR finiteness.

We study the QFV squark decays using 'scenario A' defined with the input parameters in Table 7.1. The resulting mass spectrum can be found in Table 7.2.[1] The flavour decomposition of the two lightest up-type and down-type squarks is given in Table 7.3.

For the study of the QFV gluino decays we slightly modify scenario A by setting $M_3 = 1300$ GeV, resulting in heavier gluino masses ($m_{\mathrm{OS}}^{\mathrm{SPheno}} = 1437.7$ GeV, $m_{\mathrm{OS}}^{\mathrm{FVSFOLD}} = 1419.4$ GeV, $m_{\overline{\mathrm{DR}}}^{\mathrm{FVSFOLD}} = 1300.0$ GeV) and otherwise rather negligible changes in the mass spectrum as well as in the flavour decomposition. We denote this modified reference point 'scenario B'.

We take into account the experimental constraints found in Table 7.4. The constraints stem from B-physics experiments, from the Higgs boson search and from direct searches for SUSY particles at the LHC. We chose the B-physics observables which are most relevant for our QFV mixing setup.

In Figure 7.1 we present two plots showing the lightest Higgs boson mass m_{h^0} from SPheno as a function of T_{U33} and μ using both scenarios as reference points. The light

---

[1]Please note that our calculation of m_{h^0} is at one-loop level only whereas SPheno also includes the most important two-loop contributions.

blue (green) region denotes the excluded values of m_{h^0} (BR($\overline{B} \to X_s\gamma$)), whereas the other experimental constraints are all fulfilled.

Furthermore, we define measures like

$$\Delta_{\text{Full vs SQCD}} \equiv \frac{\text{BR}(\tilde{u}_1 \to t\,\tilde{\chi}_1^0)_{\text{Full}} - \text{BR}(\tilde{u}_1 \to t\,\tilde{\chi}_1^0)_{\text{SQCD}}}{\text{BR}(\tilde{u}_1 \to t\,\tilde{\chi}_1^0)_{\text{Full}}} \,, \tag{7.1}$$

which determines the relative contribution of the EW corrections to the full one-loop result. We define the remaining measures analogously to quantify the relative differences of the branching ratios (BRs) and decay widths when comparing the full one-loop calculation with the tree-level calculation from FVSFOLD as well as with the calculation from SPheno.

Regarding the comparison of our full one-loop results with SPheno we note that, although its decay width formulas are calculated at tree-level only, SPheno improves its results by incorporating full one-loop corrections to the masses and the rotation matrices along the lines of [41]. In short, this is achieved by first adding the respective (diagonal and off-diagonal) one-loop selfenergy contributions to each already diagonalised mass matrix at tree-level in the $\overline{\text{DR}}$ scheme. This new mass matrix is then transformed using the tree-level $\overline{\text{DR}}$ rotation matrix, resulting in an effective on-shell mass matrix. At last, this effective mass matrix is re-diagonalised with an effective on-shell rotation matrix (which now intrinsically contains one-loop selfenergy contributions).

M_1	M_2	M_3	μ	$\tan\beta$	m_{A^0}
250 GeV	500 GeV	1000 GeV	2200 GeV	20	1500 GeV

	$\alpha\beta = 11$	$\alpha\beta = 22$	$\alpha\beta = 33$	$\alpha\beta = 23$	$\alpha\beta = 32$
$M_{Q_{\alpha\beta}}^2$ [GeV²]	$(2400)^2$	$(2360)^2$	$(1450)^2$	$(287)^2$	$(287)^2$
$M_{U_{\alpha\beta}}^2$ [GeV²]	$(2380)^2$	$(939.24)^2$	$(903.12)^2$	$(504.54)^2$	$(504.54)^2$
$M_{D_{\alpha\beta}}^2$ [GeV²]	$(2380)^2$	$(2340)^2$	$(2300)^2$	0	0
$M_{L_{\alpha\beta}}^2$ [GeV²]	$(500)^2$	$(500)^2$	$(600)^2$	0	0
$M_{E_{\alpha\beta}}^2$ [GeV²]	$(500)^2$	$(500)^2$	$(600)^2$	0	0
$T_{U_{\alpha\beta}}$ [GeV]	0	0	-2160	0	0

δ_{23}^{uLL}	δ_{23}^{uRR}	δ_{23}^{uRL}	δ_{23}^{uLR}	δ_{33}^{uRL}
0.024	0.300	0	0	-0.284

Table 7.1: Weak scale MSSM $\overline{\text{DR}}$ input parameters at $Q = 1$ TeV (except for the pole mass m_{A^0}) in the SPA convention [36] for scenario A. All other MSSM input parameters not shown here are zero. For completion also the derived QFV parameters δ_{23}^{uLL}, δ_{23}^{uRR}, δ_{23}^{uRL} and δ_{23}^{uLR} as well as the QFC parameter δ_{33}^{uRL} are shown.

	$m_{\mathrm{OS}}^{\mathrm{SPheno}}$ [GeV]	$m_{\mathrm{OS}}^{\mathrm{FVSFOLD}}$ [GeV]	$m_{\overline{\mathrm{DR}}}^{\mathrm{FVSFOLD}}$ [GeV]
$\tilde{u}_1$	760.3	758.4	739.1
$\tilde{u}_2$	1055.1	1051.9	1028.8
$\tilde{u}_3$	1495.3	1495.0	1493.8
$\tilde{u}_4$	2387.3	2382.5	2359.9
$\tilde{u}_5$	2401.2	2397.6	2379.7
$\tilde{u}_6$	2427.2	2422.3	2399.4
$\tilde{d}_1$	1448.7	1449.0	1449.4
$\tilde{d}_2$	2322.2	2318.8	2300.8
$\tilde{d}_3$	2363.6	2359.9	2340.1
$\tilde{d}_4$	2388.5	2383.7	2361.1
$\tilde{d}_5$	2403.7	2400.0	2380.1
$\tilde{d}_6$	2428.3	2423.4	2400.7
$\tilde{g}$	1144.3	1130.1	1000.0
$\tilde{\chi}_1^0$	248.4	248.4	249.8
$\tilde{\chi}_2^0$	522.1	521.4	499.1
$\tilde{\chi}_3^0$	2185.2	2185.8	2201.4
$\tilde{\chi}_4^0$	2186.8	2187.4	2202.5
$\tilde{\chi}_1^+$	522.3	521.6	499.1
$\tilde{\chi}_2^+$	2187.3	2187.9	2203.0
h^0	125.5	120.8	89.2

Table 7.2: Mass spectrum of the particles in scenario A derived using SPheno (physical OS masses) and FVSFOLD (OS and $\overline{\mathrm{DR}}$ masses).

	$\tilde{u}_L$	$\tilde{c}_L$	$\tilde{t}_L$	$\tilde{u}_R$	$\tilde{c}_R$	$\tilde{t}_R$
$\tilde{u}_1$	0	0	0.042	0	0.310	0.648
$\tilde{u}_2$	0	0	0.040	0	0.687	0.273
	$\tilde{d}_L$	$\tilde{s}_L$	$\tilde{b}_L$	$\tilde{d}_R$	$\tilde{s}_R$	$\tilde{b}_R$
$\tilde{d}_1$	0	0.001	0.999	0	0	0.001
$\tilde{d}_2$	0	0	0.001	0	0	0.999

Table 7.3: Squared coefficients of the flavour decomposition of $\tilde{u}_{1,2}$ and $\tilde{d}_{1,2}$ in scenario A using the squark rotation matrix from SPheno.

Observable	Constraint
$\left|\Delta M_{B_s}\right|\,[\mathrm{ps}^{-1}]$	17.73 ± 3.30
$\mathrm{BR}(\overline{B} \to X_s \gamma)$	$(3.37 \pm 0.64) \times 10^{-4}$
$\mathrm{BR}(b \to s\,\mu^+\mu^-)$	$(1.60 \pm 1.00) \times 10^{-6}$
$\mathrm{BR}(B_s \to \mu^+\mu^-)$	$(3.00 \pm 1.00) \times 10^{-9}$
$\mathrm{BR}(B^+ \to \tau^+\nu)$	$(1.15 \pm 0.23) \times 10^{-4}$
$\Delta\rho\,(\mathrm{SUSY})$	< 0.0012
$m_{h^0}\,[\mathrm{GeV}]$	126 ± 3
$m_{\tilde{g}}\,[\mathrm{GeV}]$	≥ 1000

Table 7.4: Experimental constraints from B-physics experiments, from the Higgs boson search and from direct searches for SUSY particles at the LHC (for further details and references see the appendix in [3]).
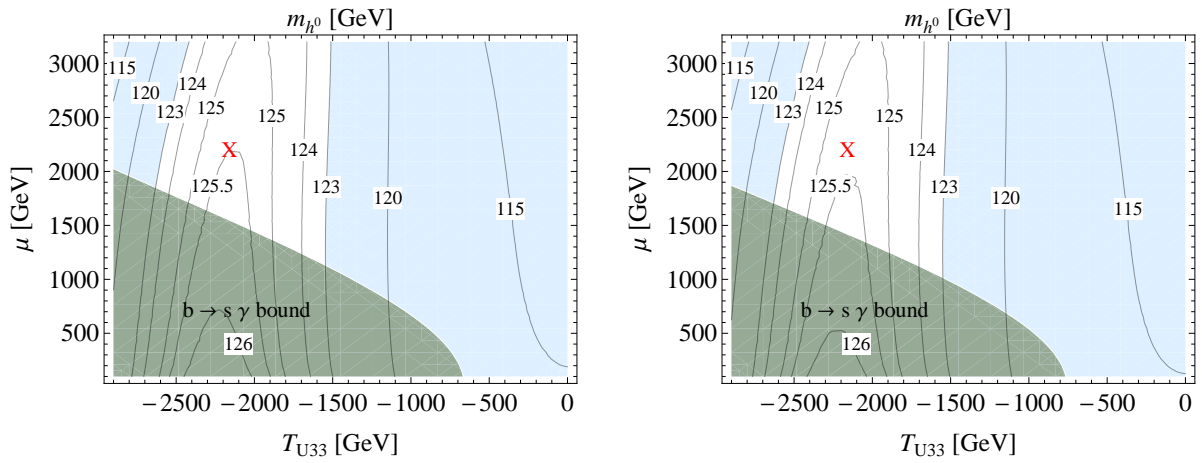
Figure 7.1: The lightest Higgs boson mass m_{h^0} taken from SPheno as a function of T_{U33} and μ using scenario A (left) and scenario B (right) as a reference point (marked with 'X' in each plot). The light blue (green) region denotes the excluded values of m_{h^0} ($\mathrm{BR}(\overline{B} \to X_s \gamma)$).

7.2   Gluino decays

In Table 7.5 we present the total decay width $\Gamma(\tilde{g})$ as well as all branching ratios (BRs) of our QFV gluino decays into squark-quark pairs using reference point B, comparing the results from SPheno with FVSFOLD. Furthermore, we show the relative differences $\Delta_{\text{Full vs SPheno}}$, $\Delta_{\text{Full vs Born}}$, and $\Delta_{\text{Full vs SQCD}}$ of $\Gamma(\tilde{g})$ and of the various BRs as defined in Eq. (7.1). The relative differences can get as high as 13.1% for reasonable large BRs, and for the highest BR (i.e. $\text{BR}(\tilde{g} \rightarrow \bar{t}\,\tilde{u}_1) + c.c.$) we obtain differences of -4.5% ($+5.0\%$) when comparing the full one-loop calculation from FVSFOLD with SPheno (SQCD from FVSFOLD). In this decay $\tilde{g} \rightarrow \bar{t}\,\tilde{u}_1$ the electroweak (EW) corrections counteract the SQCD contributions in such a way that the simple tree-level result matches the full one-loop result best. The decay $\tilde{g} \rightarrow \bar{c}\,\tilde{u}_1$ also shows this inverse feature with even bigger EW than SQCD corrections. In the decays into $\tilde{u}_2$ the EW corrections have the same sign as the SQCD contributions, but again with a higher magnitude. Thus one can clearly see that the EW corrections to the gluino two-body decays cannot be neglected at all!

	SPheno	FVSFOLD			$\Delta_{\text{Full vs ...}}\ [\times 10^{-2}]$		
		Born	SQCD	Full	SPheno	Born	SQCD
$\Gamma(\tilde{g})$ [GeV]	20.357	19.591	20.620	20.463	0.52	4.26	-0.77
$\text{BR}(\tilde{g} \rightarrow \bar{c}\,\tilde{u}_1) + c.c.$	0.251	0.288	0.293	0.263	4.56	-9.51	-11.41
$\text{BR}(\tilde{g} \rightarrow \bar{t}\,\tilde{u}_1) + c.c.$	0.463	0.439	0.421	0.443	-4.51	0.90	4.97
$\text{BR}(\tilde{g} \rightarrow \bar{c}\,\tilde{u}_2) + c.c.$	0.222	0.205	0.219	0.236	5.93	13.14	7.20
$\text{BR}(\tilde{g} \rightarrow \bar{t}\,\tilde{u}_2) + c.c.$	0.061	0.068	0.067	0.058	-5.17	-17.24	-15.52

Table 7.5: Total decay width and all branching ratios (including charge conjugated decays) of $\tilde{g}$ in scenario B, comparing the results from SPheno with FVSFOLD (tree-level, SUSY-QCD, full one-loop corrections). In addition the relative differences of this comparison are shown for convenience.

In Figures 7.2-7.5 we show 2D contour plots of the branching ratios $\text{BR}(\tilde{g} \rightarrow \bar{t}\,\tilde{u}_1) + c.c.$ and $\text{BR}(\tilde{g} \rightarrow \bar{c}\,\tilde{u}_1) + c.c.$ from SPheno as a function of doublets of the QFV parameters δ_{23}^{uRR}, δ_{23}^{uRL}, δ_{23}^{uLL} and the quark flavour conserving (QFC) parameter δ_{33}^{uRL}. In each figure scenario B is used as a reference point, and the parameter regions yielding excluded values for m_{h^0}, $\text{BR}(\overline{B} \rightarrow X_s\gamma)$ and $|\Delta M_{B_s}|$ are highlighted in different colours. We provide these plots as a broad overview of the QFV and QFC parameter dependences, so that we can pick the most interesting parameters (mainly δ_{23}^{uRR} but also δ_{23}^{uRL} in this scenario) for a detailed comparison of SPheno with FVSFOLD (see Figures 7.6-7.11 below). The dependence on δ_{23}^{uRR} (affecting the $\tilde{t}_R$ - $\tilde{c}_R$ mixing) is most prominently seen and understood in the $\tilde{g} \rightarrow \bar{c}\,\tilde{u}_1$ decay, where the BR rapidly rises from almost zero (at $\delta_{23}^{uRR} \sim 0$, i.e. $\tilde{u}_1$ is basically $\tilde{t}_R$-like) to more than 35% with higher (absolute) values of δ_{23}^{uRR} indicating a sizeable admixture of $\tilde{c}_R$ to $\tilde{u}_1$ (see also Table 7.3). The reason for this

dependence is rooted in the $\tilde{g}\, c\, \tilde{u}_1$ coupling (see Eq. (6.2)), where the dominant term proportional to $R^{\tilde{u}}_{15}$ is due to the $\tilde{t}_R$ - $\tilde{c}_R$ mixing. The dependence on δ^{uRL}_{23} (encoding the $\tilde{t}_L$ - $\tilde{c}_R$ mixing) is much less pronounced in these plots since we present decays into $\tilde{u}_1$ which are dominantly $\tilde{t}_R$-like. We also studied the dependence on δ^{uLR}_{23} ($\tilde{t}_R$ - $\tilde{c}_L$ mixing) which is however irrelevant in our scenario since the $\tilde{c}_L$ part in $\tilde{u}_1$ remains basically zero.
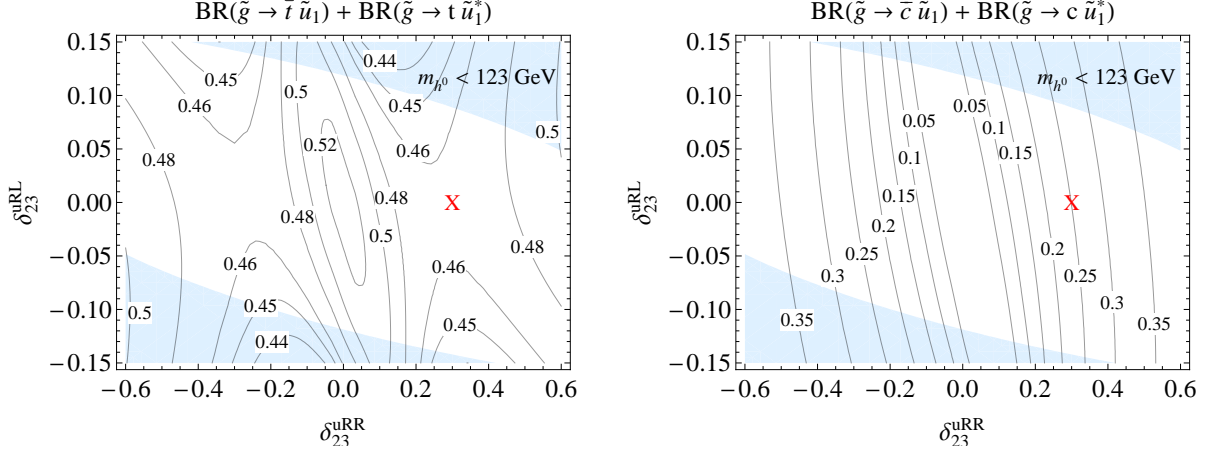
Figure 7.2: The branching ratios $\mathrm{BR}(\tilde{g} \to \bar{t}\,\tilde{u}_1) + c.c.$ (left) and $\mathrm{BR}(\tilde{g} \to \bar{c}\,\tilde{u}_1) + c.c.$ (right) from SPheno as a function of δ^{uRR}_{23} and δ^{uRL}_{23} using scenario B as a reference point (denoted with 'X' in each plot). The light blue region shows the excluded values of m_{h^0} with 95% CL.

In Figure 7.6 we present the total decay width $\Gamma(\tilde{g})$ as a function of δ^{uRR}_{23} comparing the result from SPheno with the tree-level, SQCD and full one-loop calculation from FVSFOLD. For better comparison also the relative differences of the full one-loop result with the other partial results are shown. $\Gamma(\tilde{g})$ increases about 23% with higher (absolute) values of δ^{uRR}_{23} due to the $\tilde{g} \to \bar{c}\,\tilde{u}_1$ decay becoming more enhanced (see explanation in previous paragraph). We observe a good agreement with SPheno, partly because the EW corrections to the full calculation remain with just $\sim 1\%$ rather small.

In Figure 7.7 we show the branching ratio $\mathrm{BR}(\tilde{g} \to \bar{t}\,\tilde{u}_1) + c.c.$ as a function of δ^{uRR}_{23} comparing the result from SPheno with the tree-level, SQCD and full one-loop calculation from FVSFOLD. We also present the relative differences of the full one-loop result with the other partial results for convenience. The EW corrections counteract the SQCD contributions and amount up to 6% to the full one-loop result. Thus the EW corrections cannot be neglected in our scenario.

Figure 7.8 shows the branching ratio $\mathrm{BR}(\tilde{g} \to \bar{c}\,\tilde{u}_1) + c.c.$ as a function of δ^{uRR}_{23} comparing again the result from SPheno with the tree-level, SQCD and full one-loop calculation from FVSFOLD and again showing the relative differences for better comparison. Please note that we focus on a smaller interval of δ^{uRR}_{23} since both plots are symmetric and small $|\delta^{uRR}_{23}|$ correspond to vanishing BR which lead to numerically unstable relative differences. Once more the EW corrections cannot be neglected, since their relative contribution can be as high as $\sim 20\%$ for weaker $\tilde{t}_R$ - $\tilde{c}_R$ mixing and still remain at $\sim 5\%$ for stronger mixing.
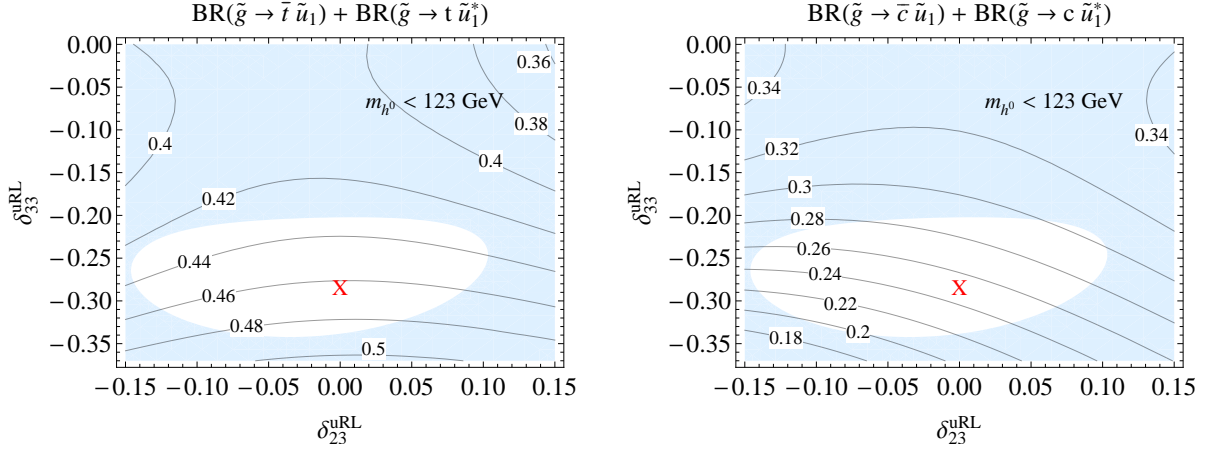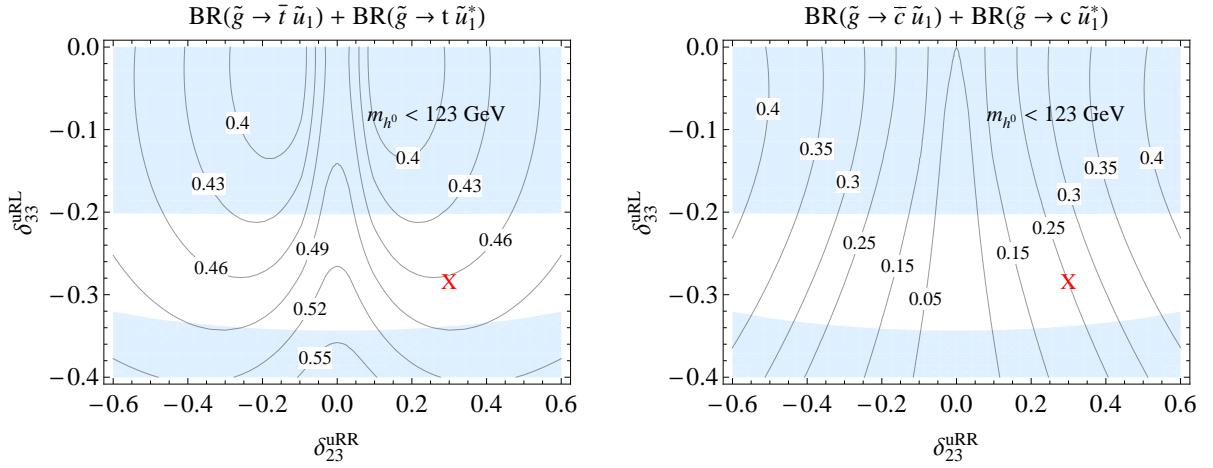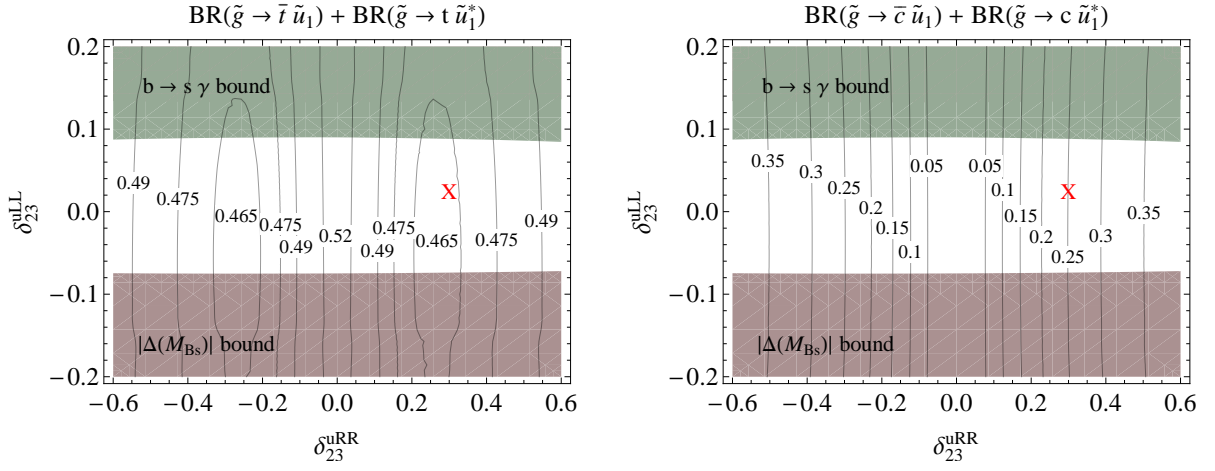
Figure 7.3: The branching ratios $BR(\tilde{g} \to \bar{t}\,\tilde{u}_1) + c.c.$ (left) and $BR(\tilde{g} \to \bar{c}\,\tilde{u}_1) + c.c.$ (right) from SPheno as a function of δ_{23}^{uRL} and δ_{33}^{uRL} using scenario B as a reference point (denoted with 'X' in each plot). The light blue region shows the excluded values of m_{h^0} with 95% CL.

Figure 7.4: The branching ratios $BR(\tilde{g} \to \bar{t}\,\tilde{u}_1) + c.c.$ (left) and $BR(\tilde{g} \to \bar{c}\,\tilde{u}_1) + c.c.$ (right) from SPheno as a function of δ_{23}^{uRR} and δ_{33}^{uRL} using scenario B as a reference point (denoted with 'X' in each plot). The light blue region shows the excluded values of m_{h^0} with 95% CL.

Figure 7.5: The branching ratios $\mathrm{BR}(\tilde{g} \to \bar{t}\,\tilde{u}_1) + c.c.$ (left) and $\mathrm{BR}(\tilde{g} \to \bar{c}\,\tilde{u}_1) + c.c.$ (right) from SPheno as a function of δ_{23}^{uRR} and δ_{23}^{uLL} using scenario B as a reference point (denoted with 'X' in each plot). The green (red) region shows the excluded values of $\mathrm{BR}(\overline{B} \to X_s \gamma)$ ($|\Delta M_{B_s}|$).
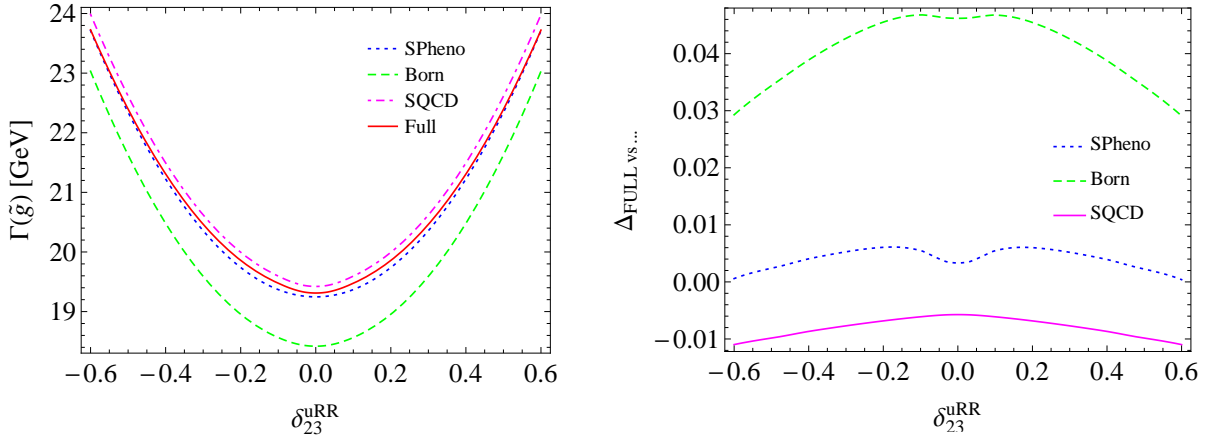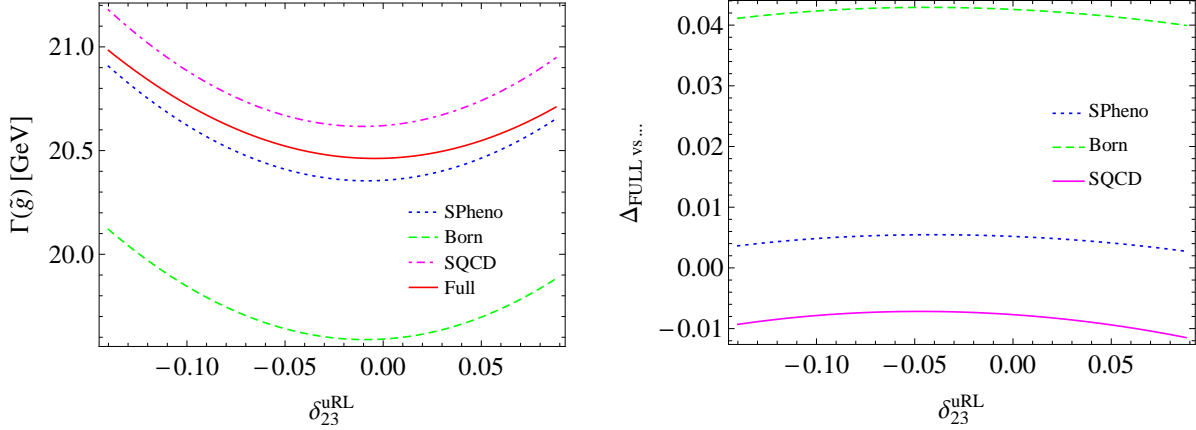

Figure 7.6: Left: Total decay width of $\tilde{g}$ as a function of δ_{23}^{uRR} using scenario B as a starting point, comparing the results from SPheno with FVSFOLD (tree-level, SQCD, full one-loop corrections). Right: Relative differences of this $\Gamma(\tilde{g})$, comparing the full one-loop calculation from FVSFOLD with the tree-level ($\Delta_{\mathrm{Full\ vs\ Born}}$) and SQCD ($\Delta_{\mathrm{Full\ vs\ SQCD}}$) calculation (both from FVSFOLD) as well as with the calculation from SPheno ($\Delta_{\mathrm{Full\ vs\ SPheno}}$).
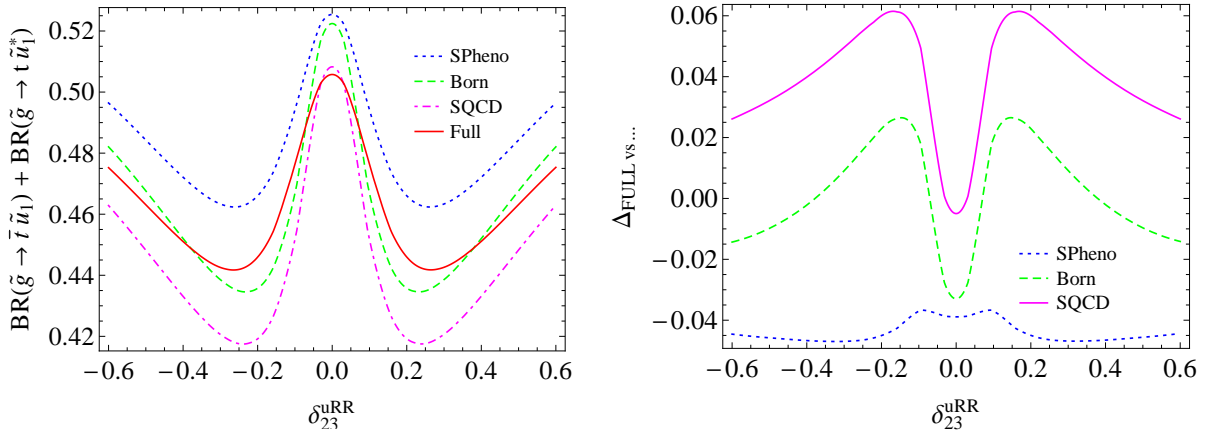
Figure 7.7: Left: The branching ratio $\text{BR}(\tilde{g} \to \bar{t}\,\tilde{u}_1) + c.c.$ as a function of δ_{23}^{uRR} using scenario B as a starting point, comparing the results from SPheno with FVSFOLD (tree-level, SQCD, full one-loop corrections). Right: Relative differences of this BR, comparing the full one-loop calculation from FVSFOLD with the tree-level ($\Delta_{\text{Full vs Born}}$) and SQCD ($\Delta_{\text{Full vs SQCD}}$) calculation (both from FVSFOLD) as well as with the calculation from SPheno ($\Delta_{\text{Full vs SPheno}}$).
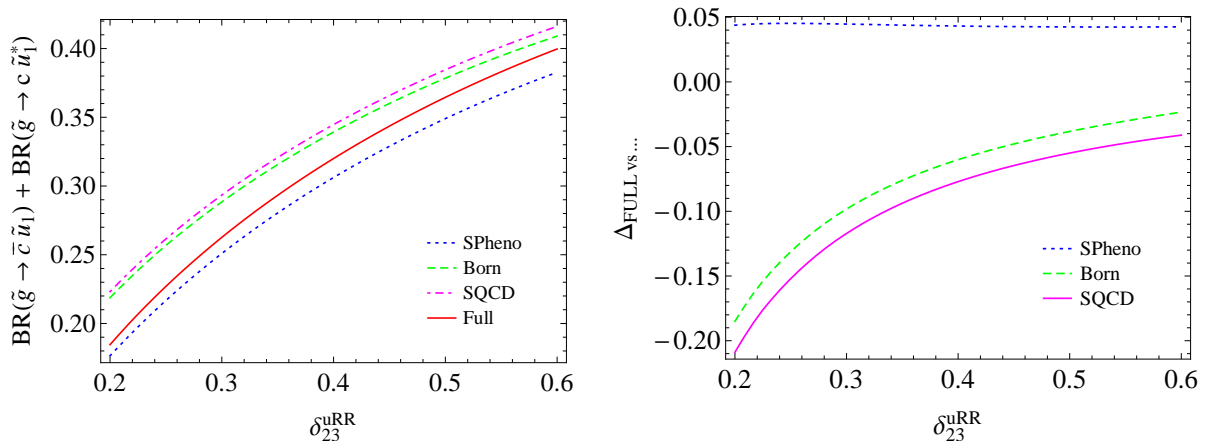
Figure 7.8: Left: The branching ratio $\text{BR}(\tilde{g} \to \bar{c}\,\tilde{u}_1) + c.c.$ as a function of δ_{23}^{uRR} using scenario B as a starting point, comparing the results from SPheno with FVSFOLD (tree-level, SQCD, full one-loop corrections). Right: Relative differences of this BR, comparing the full one-loop calculation from FVSFOLD with the tree-level ($\Delta_{\text{Full vs Born}}$) and SQCD ($\Delta_{\text{Full vs SQCD}}$) calculation (both from FVSFOLD) as well as with the calculation from SPheno ($\Delta_{\text{Full vs SPheno}}$).

In Figure 7.9 we present the total decay width $\Gamma(\tilde{g})$ as a function of δ_{23}^{uRL} comparing the result from SPheno with the various results from FVSFOLD. Relative differences of these results are again shown for better comparison. As already anticipated the dependence on δ_{23}^{uRL} is much weaker, and we observe just $\sim 1\%$ relative contribution of EW corrections to the full one-loop result.

Figure 7.9: Left: Total decay width of $\tilde{g}$ as a function of δ_{23}^{uRL} using scenario B as a starting point, comparing the result from SPheno with FVSFOLD (tree-level, SQCD, full one-loop corrections). Right: Relative differences of this $\Gamma(\tilde{g})$, comparing the full one-loop calculation from FVSFOLD with the tree-level ($\Delta_{\text{Full vs Born}}$) and SQCD ($\Delta_{\text{Full vs SQCD}}$) calculation (both from FVSFOLD) as well as with the calculation from SPheno ($\Delta_{\text{Full vs SPheno}}$).

Figure 7.10 displays $\text{BR}(\tilde{g} \to \bar{t}\,\tilde{u}_1) + c.c.$ as a function of δ_{23}^{uRL} comparing SPheno with FVSFOLD, and shows relative differences of the BRs for better comparison. The EW corrections basically cancel the SQCD contributions and amount up to 6% to the full one-loop result. Therefore, the EW corrections cannot be neglected at all.

At last, in Figure 7.11 we present $\text{BR}(\tilde{g} \to \bar{c}\,\tilde{u}_1) + c.c.$ as a function of δ_{23}^{uRL} comparing SPheno with FVSFOLD, and show relative differences of the BRs for better comparison. The relative contribution of the EW corrections to the full result can rise up to 15% and hence cannot be neglected.
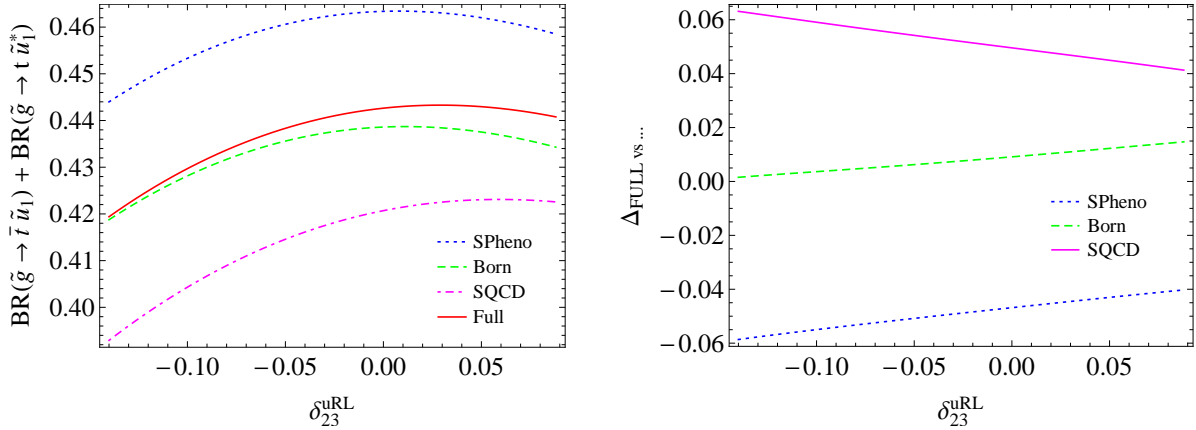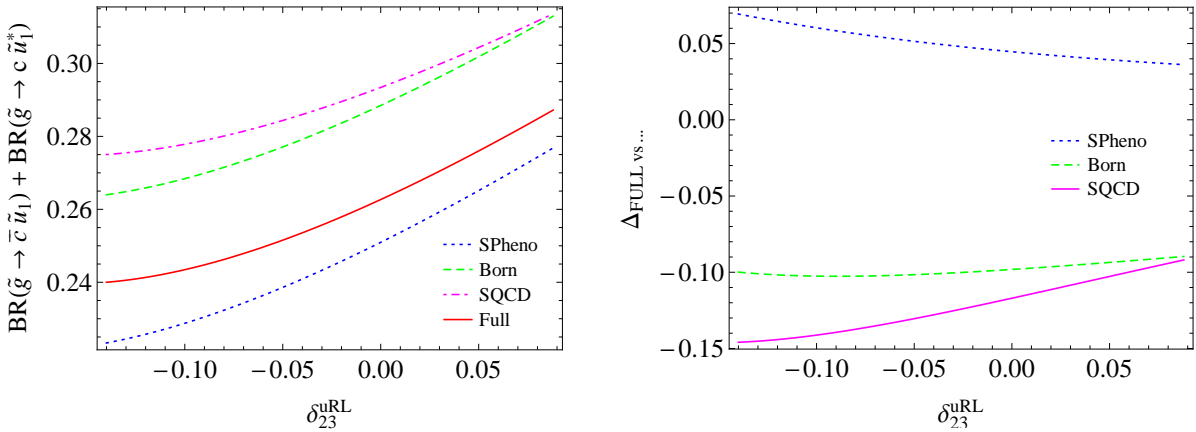
Figure 7.10: Left: The branching ratio $\mathrm{BR}(\tilde{g} \to \bar{t}\,\tilde{u}_1) + c.c.$ as a function of δ_{23}^{uRL} using scenario B as a starting point, comparing the results from SPheno with FVSFOLD (tree-level, SQCD, full one-loop corrections). Right: Relative differences of this BR, comparing the full one-loop calculation from FVSFOLD with the tree-level ($\Delta_{\mathrm{Full\ vs\ Born}}$) and SQCD ($\Delta_{\mathrm{Full\ vs\ SQCD}}$) calculation (both from FVSFOLD) as well as with the calculation from SPheno ($\Delta_{\mathrm{Full\ vs\ SPheno}}$).

Figure 7.11: Left: The branching ratio $\mathrm{BR}(\tilde{g} \to \bar{c}\,\tilde{u}_1) + c.c.$ as a function of δ_{23}^{uRL} using scenario B as a starting point, comparing the results from SPheno with FVSFOLD (tree-level, SQCD, full one-loop corrections). Right: Relative differences of this BR, comparing the full one-loop calculation from FVSFOLD with the tree-level ($\Delta_{\mathrm{Full\ vs\ Born}}$) and SQCD ($\Delta_{\mathrm{Full\ vs\ SQCD}}$) calculation (both from FVSFOLD) as well as with the calculation from SPheno ($\Delta_{\mathrm{Full\ vs\ SPheno}}$).

7.3 Squark decays

In Table 7.6 we present the total decay widths and all branching ratios (BRs) of QFV $\tilde{u}_1$ and $\tilde{d}_1$ two-body decays as well as all partial decay widths of $\tilde{u}_2$ in scenario A, comparing the results from SPheno with FVSFOLD. Furthermore, we show the relative differences $\Delta_{\text{Full vs SPheno}}$, $\Delta_{\text{Full vs Born}}$, and $\Delta_{\text{Full vs SQCD}}$ of this comparison as defined in Eq. (7.1). Please note that currently decays into Higgses are calculated at tree-level only, hence for $\tilde{u}_2$ decays only partial decay widths are a meaningful comparison. The relative contribution of EW corrections to the full one-loop result (i.e. $\Delta_{\text{Full vs SQCD}}$) can get as high as -24.4%, but even in less extreme cases the EW corrections cannot be neglected at all!

In Figures 7.12-7.15 we show 2D contour plots of the branching ratios $\text{BR}(\tilde{u}_1 \to t\,\tilde{\chi}_1^0)$, $\text{BR}(\tilde{u}_1 \to c\,\tilde{\chi}_1^0)$, $\text{BR}(\tilde{u}_1 \to b\,\tilde{\chi}_1^+)$, $\text{BR}(\tilde{d}_1 \to \tilde{u}_1\,W^-)$ and the partial decay width $\Gamma(\tilde{u}_2 \to \tilde{u}_1\,Z^0)$ from SPheno as a function of doublets of the QFV parameters δ_{23}^{uRR}, δ_{23}^{uRL}, δ_{23}^{uLL} and the quark flavour conserving (QFC) parameter δ_{33}^{uRL}. In each figure scenario B is used as a reference point, and the parameter regions yielding excluded values for m_{h^0}, $\text{BR}(\overline{B} \to X_s\gamma)$ and $|\Delta M_{B_s}|$ are highlighted in different colours. We provide these plots again as a broad overview of the QFV and QFC parameter dependences, so that we can select the most promising parameters (mostly δ_{23}^{uRR} but also δ_{23}^{uRL} in this scenario) for a detailed comparison of SPheno with FVSFOLD (see Figures 7.16-7.26 below).

In Figures 7.16-7.19 we present the total decay width of $\tilde{u}_1$ as well as the branching ratios $\text{BR}(\tilde{u}_1 \to t\,\tilde{\chi}_1^0)$, $\text{BR}(\tilde{u}_1 \to c\,\tilde{\chi}_1^0)$ and $\text{BR}(\tilde{u}_1 \to b\,\tilde{\chi}_1^+)$ as a function of δ_{23}^{uRR} ($\tilde{t}_R$ - $\tilde{c}_R$ mixing), comparing the result from SPheno with the tree-level, SQCD and full one-loop calculation from FVSFOLD. For better comparison also the relative differences of the full one-loop result with the other partial results are shown. We note that $\Gamma(\tilde{u}_1)$ increases significantly up to $\sim 54\%$ within the QFV parameter range of δ_{23}^{uRR}. The EW corrections to the full calculation can be rather parameter-independent and small ($\sim 3\%$ in $\Gamma(\tilde{u}_1)$) but also strongly dependent on δ_{23}^{uRR} with values of more than 20% as in $\text{BR}(\tilde{u}_1 \to c\,\tilde{\chi}_1^0)$ for weaker mixing. We can thus clearly see that we cannot neglect the EW contributions in our scenario, since their contributions can be quite large! The relative differences of the full result compared to SPheno varies and can be as high as 9% as in $\Gamma(\tilde{u}_1)$ for negligible $\tilde{t}_R$ - $\tilde{c}_R$ mixing.

In Figure 7.20 we show the partial decay width $\Gamma(\tilde{u}_2 \to \tilde{u}_1\,Z^0)$ as a function of δ_{23}^{uRR} comparing the result from SPheno with the results from FVSFOLD, and presenting the relative differences for better comparison. The EW corrections to the full calculation are quite small with $2-5\%$ and show a weak dependence on the parameter. As a result, the rather poor performance of SPheno in this decay channel comes as a surprise.

In Figures 7.21-7.24 we present the total decay width of $\tilde{u}_1$ as well as the branching ratios $\text{BR}(\tilde{u}_1 \to t\,\tilde{\chi}_1^0)$, $\text{BR}(\tilde{u}_1 \to c\,\tilde{\chi}_1^0)$ and $\text{BR}(\tilde{u}_1 \to b\,\tilde{\chi}_1^+)$ as a function of δ_{23}^{uRL} ($\tilde{t}_L$ - $\tilde{c}_R$ mixing), comparing the result from SPheno with the tree-level, SQCD and full one-loop calculation from FVSFOLD. For better comparison also the relative differences of the full one-loop result with the other partial results are shown. The EW corrections to the full calculation can become large, ranging $9-15\%$ for the $\text{BR}(\tilde{u}_1 \to c\,\tilde{\chi}_1^0)$ or even $16-27\%$ for the $\text{BR}(\tilde{u}_1 \to b\,\tilde{\chi}_1^+)$ (which is however a decay channel with small BR). In comparison, the EW corrections in the remaining BR and the total decay width are

	SPheno	FVSFOLD			$\Delta_{\text{Full vs ...}}$ $[\times 10^{-2}]$		
		Born	SQCD	Full	SPheno	Born	SQCD
$\Gamma(\tilde{u}_1)$ [GeV]	1.363	1.355	1.347	1.313	-3.78	-3.20	-2.55
$\text{BR}(\tilde{u}_1 \to c\,\tilde{\chi}_1^0)$	0.319	0.365	0.376	0.335	4.56	-9.06	-12.24
$\text{BR}(\tilde{u}_1 \to t\,\tilde{\chi}_1^0)$	0.600	0.564	0.554	0.580	-3.50	2.67	4.48
$\text{BR}(\tilde{u}_1 \to t\,\tilde{\chi}_2^0)$	0.019	0.016	0.017	0.020	4.68	16.60	14.88
$\text{BR}(\tilde{u}_1 \to b\,\tilde{\chi}_1^+)$	0.062	0.054	0.054	0.066	6.31	17.49	18.25
$\Gamma(\tilde{u}_2 \to c\,\tilde{\chi}_1^0)$ [GeV]	1.501	1.401	1.386	1.473	-1.85	4.90	5.94
$\Gamma(\tilde{u}_2 \to t\,\tilde{\chi}_1^0)$ [GeV]	0.575	0.658	0.605	0.486	-18.29	-35.45	-24.39
$\Gamma(\tilde{u}_2 \to t\,\tilde{\chi}_2^0)$ [GeV]	0.099	0.102	0.097	0.093	-5.95	-9.27	-3.67
$\Gamma(\tilde{u}_2 \to b\,\tilde{\chi}_1^+)$ [GeV]	0.219	0.226	0.214	0.214	-2.34	-5.62	0.14
$\Gamma(\tilde{u}_2 \to \tilde{u}_1\,Z^0)$ [GeV]	0.061	0.056	0.061	0.064	5.38	13.61	4.42
$\Gamma(\tilde{u}_2 \to \tilde{u}_1\,h^0)$ [GeV]	0.971	0.971					
$\Gamma(\tilde{d}_1)$ [GeV]	62.489	60.924	62.018	59.057	-5.81	-3.16	-5.02
$\text{BR}(\tilde{d}_1 \to b\,\tilde{\chi}_1^0)$	0.003	0.003	0.003	0.003	-11.05	-13.58	-2.08
$\text{BR}(\tilde{d}_1 \to b\,\tilde{\chi}_2^0)$	0.071	0.073	0.065	0.071	-0.66	-3.38	7.36
$\text{BR}(\tilde{d}_1 \to t\,\tilde{\chi}_1^-)$	0.136	0.140	0.124	0.132	-3.33	-6.10	5.55
$\text{BR}(\tilde{d}_1 \to b\,\tilde{g})$	0.194	0.216	0.233	0.242	19.79	10.73	4.00
$\text{BR}(\tilde{d}_1 \to \tilde{u}_1\,W^-)$	0.475	0.437	0.443	0.434	-9.42	-0.49	-1.95
$\text{BR}(\tilde{d}_1 \to \tilde{u}_2\,W^-)$	0.120	0.131	0.131	0.118	-1.60	-11.10	-11.61

Table 7.6: Total decay widths and all branching ratios of $\tilde{u}_1$ and $\tilde{d}_1$ as well as all partial decay widths of $\tilde{u}_2$ in scenario A, comparing the results from SPheno with FVSFOLD (tree-level, SUSY-QCD, full one-loop corrections). In addition the relative differences of this comparison are shown for convenience. Note that currently decays into Higgses are calculated at tree-level only.
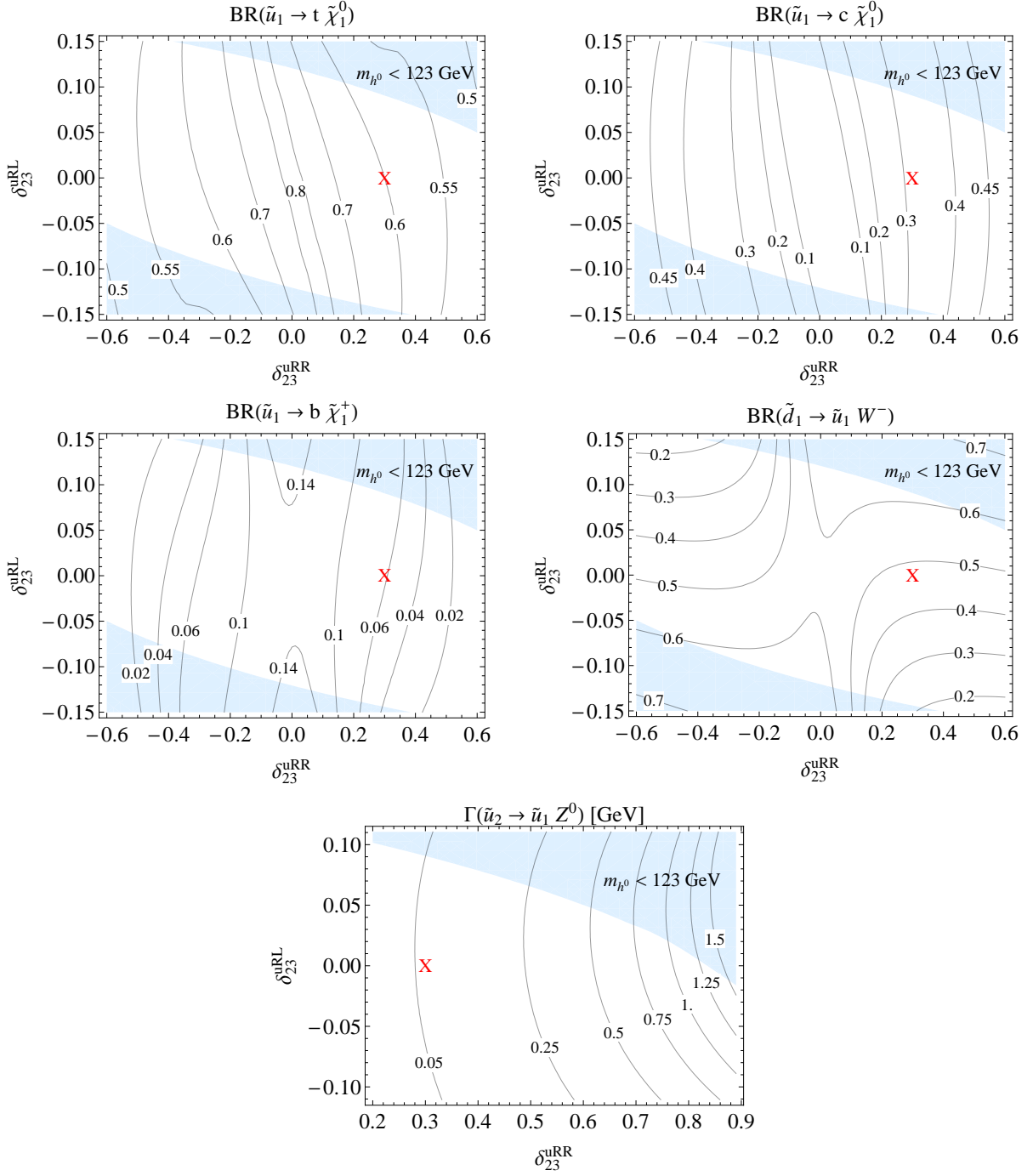
Figure 7.12: The branching ratios $\mathrm{BR}(\tilde{u}_1 \to t\, \tilde{\chi}_1^0)$ (top left), $\mathrm{BR}(\tilde{u}_1 \to c\, \tilde{\chi}_1^0)$ (top right), $\mathrm{BR}(\tilde{u}_1 \to b\, \tilde{\chi}_1^+)$ (center left), $\mathrm{BR}(\tilde{d}_1 \to \tilde{u}_1\, W^-)$ (center right) and the partial decay width $\Gamma(\tilde{u}_2 \to \tilde{u}_1\, Z^0)$ (bottom) from SPheno as a function of δ_{23}^{uRR} and δ_{23}^{uRL} using scenario A as a reference point (denoted with 'X' in each plot). The light blue region shows the excluded values of m_{h^0} with 95% CL. In the $\Gamma(\tilde{u}_2 \to \tilde{u}_1\, Z^0)$ plot we use a wider interval for δ_{23}^{uRR} and focus on the positive axis since the plot is quasi-symmetric.
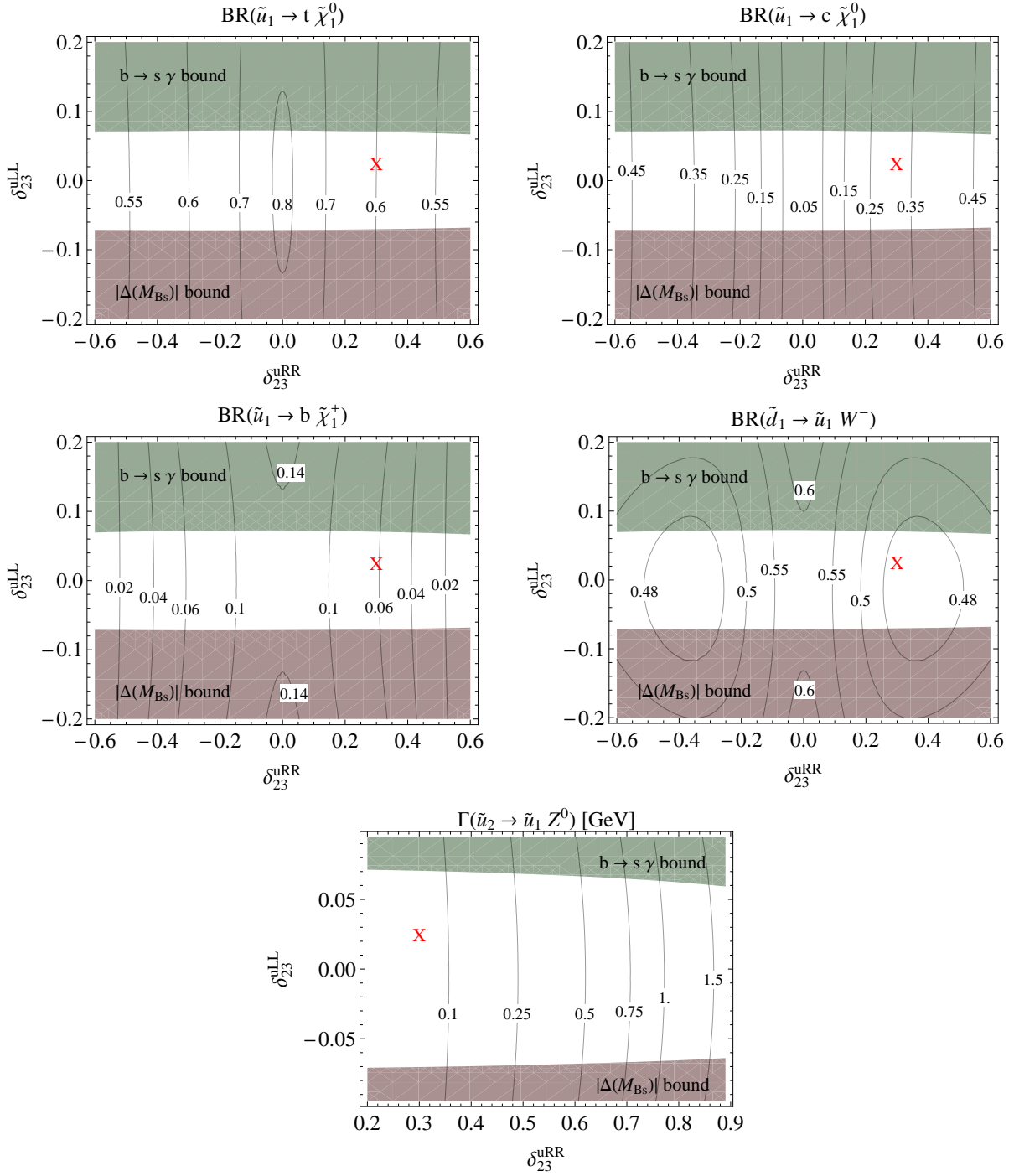
Figure 7.13: The branching ratios $\mathrm{BR}(\tilde{u}_1 \to t\,\tilde{\chi}_1^0)$ (top left), $\mathrm{BR}(\tilde{u}_1 \to c\,\tilde{\chi}_1^0)$ (top right), $\mathrm{BR}(\tilde{u}_1 \to b\,\tilde{\chi}_1^+)$ (center left), $\mathrm{BR}(\tilde{d}_1 \to \tilde{u}_1\,W^-)$ (center right) and the partial decay width $\Gamma(\tilde{u}_2 \to \tilde{u}_1\,Z^0)$ (bottom) from SPheno as a function of δ_{23}^{uRL} and δ_{33}^{uRL} using scenario A as a reference point (denoted with 'X' in each plot). The light blue region shows the excluded values of m_{h^0} with 95% CL.
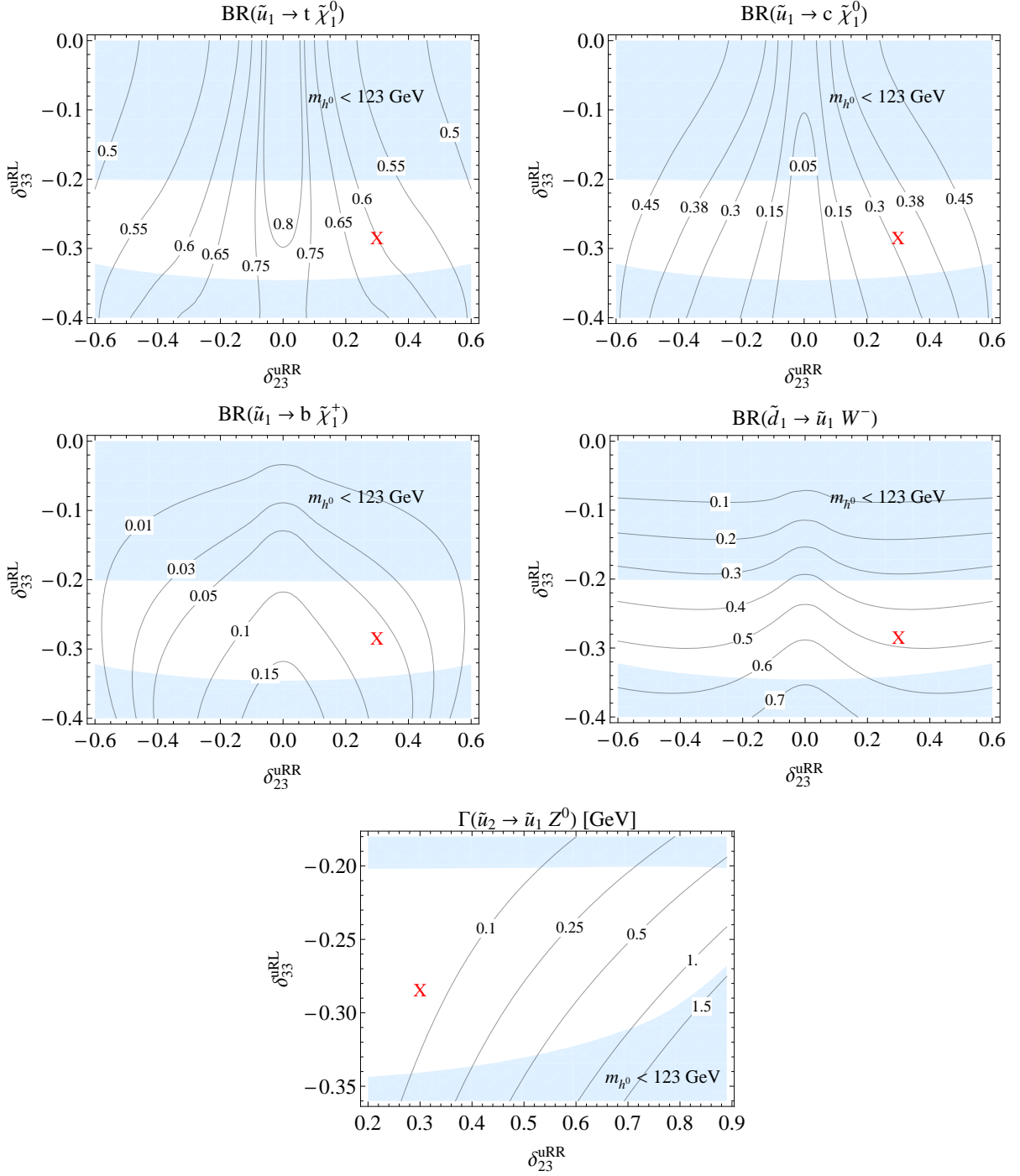
Figure 7.14: The branching ratios $\mathrm{BR}(\tilde{u}_1 \to t\,\tilde{\chi}_1^0)$ (top left), $\mathrm{BR}(\tilde{u}_1 \to c\,\tilde{\chi}_1^0)$ (top right), $\mathrm{BR}(\tilde{u}_1 \to b\,\tilde{\chi}_1^+)$ (center left), $\mathrm{BR}(\tilde{d}_1 \to \tilde{u}_1\,W^-)$ (center right) and the partial decay width $\Gamma(\tilde{u}_2 \to \tilde{u}_1\,Z^0)$ (bottom) from SPheno as a function of δ_{23}^{uRR} and δ_{33}^{uRL} using scenario A as a reference point (denoted with 'X' in each plot). The light blue region shows the excluded values of m_{h^0} with 95% CL. In the $\Gamma(\tilde{u}_2 \to \tilde{u}_1\,Z^0)$ plot we use a wider interval for δ_{23}^{uRR} and focus on the positive axis since the plot is quasi-symmetric.

Figure 7.15: The branching ratios $\mathrm{BR}(\tilde{u}_1 \to t\,\tilde{\chi}_1^0)$ (top left), $\mathrm{BR}(\tilde{u}_1 \to c\,\tilde{\chi}_1^0)$ (top right), $\mathrm{BR}(\tilde{u}_1 \to b\,\tilde{\chi}_1^+)$ (center left), $\mathrm{BR}(\tilde{d}_1 \to \tilde{u}_1\,W^-)$ (center right) and the partial decay width $\Gamma(\tilde{u}_2 \to \tilde{u}_1\,Z^0)$ (bottom) from SPheno as a function of δ_{23}^{uRR} and δ_{23}^{uLL} using scenario A as a reference point (denoted with 'X' in each plot). The green (red) region shows the excluded values of $\mathrm{BR}(\overline{B} \to X_s\gamma)$ ($|\Delta M_{B_s}|$). In the $\Gamma(\tilde{u}_2 \to \tilde{u}_1\,Z^0)$ plot we use a wider interval for δ_{23}^{uRR} and focus on the positive axis since the plot is quasi-symmetric.
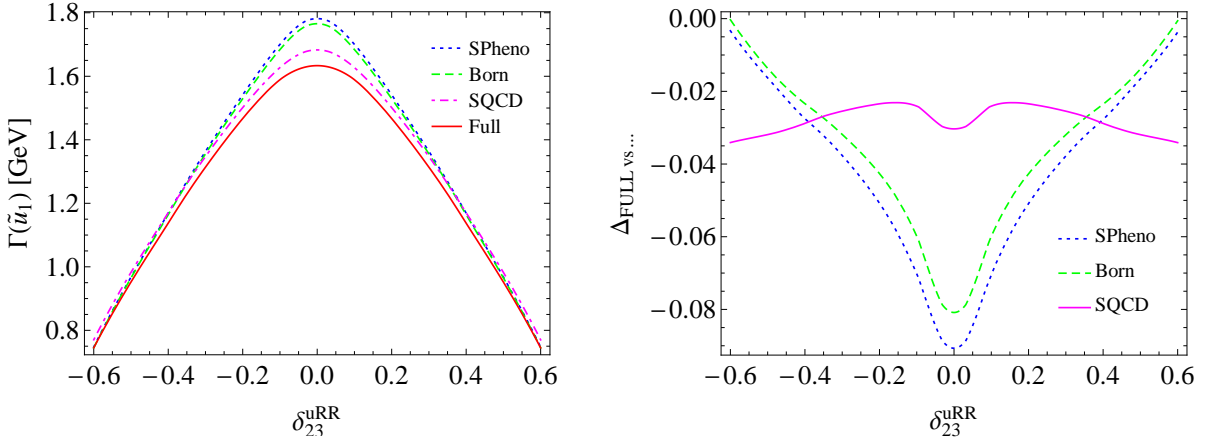
Figure 7.16: Left: Total decay width of $\tilde{u}_1$ as a function of δ_{23}^{uRR} using scenario A as a starting point, comparing the results from SPheno with FVSFOLD (tree-level, SQCD, full one-loop corrections). Right: Relative differences of this $\Gamma(\tilde{u}_1)$, comparing the full one-loop calculation from FVSFOLD with the tree-level ($\Delta_{\text{Full vs Born}}$) and SQCD ($\Delta_{\text{Full vs SQCD}}$) calculation (both from FVSFOLD) as well as with the calculation from SPheno ($\Delta_{\text{Full vs SPheno}}$).
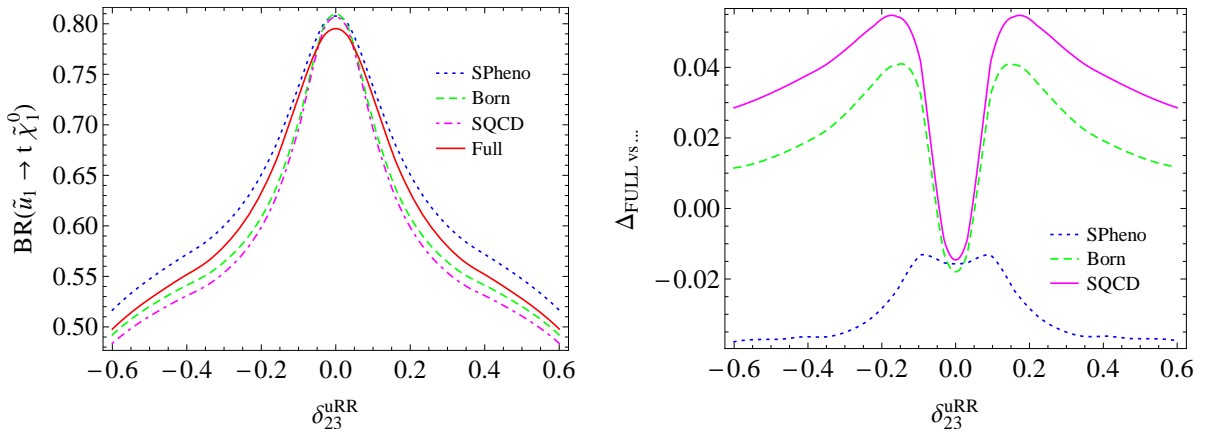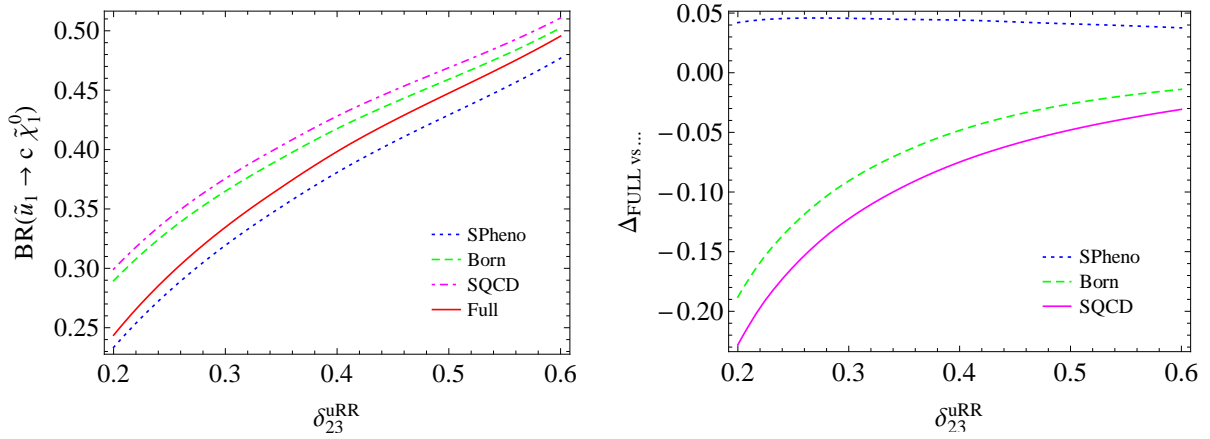

Figure 7.17: Left: The branching ratio $\text{BR}(\tilde{u}_1 \rightarrow t\,\tilde{\chi}_1^0)$ as a function of δ_{23}^{uRR} using scenario A as a starting point, comparing the results from SPheno with FVSFOLD (tree-level, SQCD, full one-loop corrections). Right: Relative differences of this BR, comparing the full one-loop calculation from FVSFOLD with the tree-level ($\Delta_{\text{Full vs Born}}$) and SQCD ($\Delta_{\text{Full vs SQCD}}$) calculation (both from FVSFOLD) as well as with the calculation from SPheno ($\Delta_{\text{Full vs SPheno}}$).
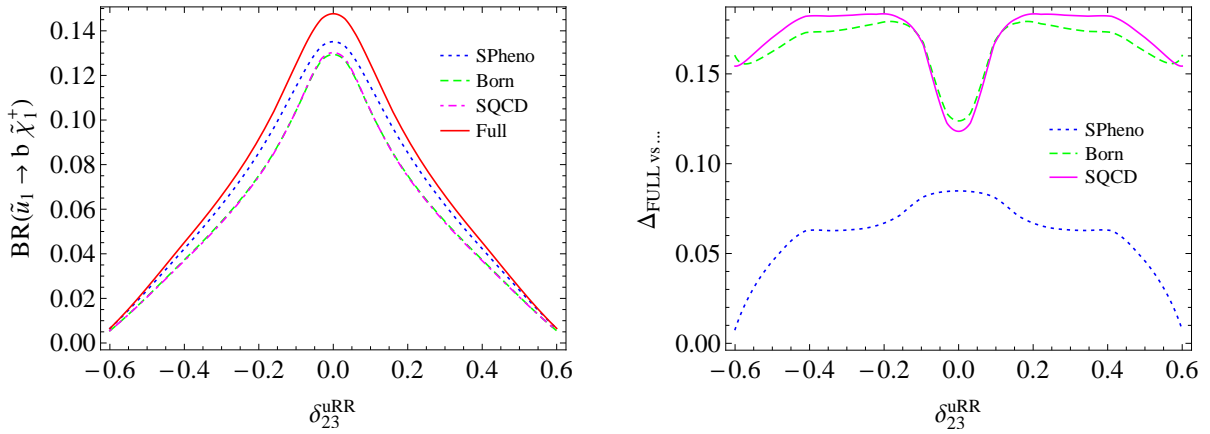
Figure 7.18: Left: The branching ratio $\mathrm{BR}(\tilde{u}_1 \to c\,\tilde{\chi}_1^0)$ as a function of δ_{23}^{uRR} using scenario A as a starting point, comparing the results from SPheno with FVSFOLD (tree-level, SQCD, full one-loop corrections). Right: Relative differences of this BR, comparing the full one-loop calculation from FVSFOLD with the tree-level ($\Delta_{\text{Full vs Born}}$) and SQCD ($\Delta_{\text{Full vs SQCD}}$) calculation (both from FVSFOLD) as well as with the calculation from SPheno ($\Delta_{\text{Full vs SPheno}}$). Please note that we focus on a smaller interval of δ_{23}^{uRR} since both plots are symmetric and small $|\delta_{23}^{uRR}|$ correspond to vanishing BR which lead to numerically unstable relative differences Δ.

Figure 7.19: Left: The branching ratio $\mathrm{BR}(\tilde{u}_1 \to b\,\tilde{\chi}_1^+)$ as a function of δ_{23}^{uRR} using scenario A as a starting point, comparing the results from SPheno with FVSFOLD (tree-level, SQCD, full one-loop corrections). Right: Relative differences of this BR, comparing the full one-loop calculation from FVSFOLD with the tree-level ($\Delta_{\text{Full vs Born}}$) and SQCD ($\Delta_{\text{Full vs SQCD}}$) calculation (both from FVSFOLD) as well as with the calculation from SPheno ($\Delta_{\text{Full vs SPheno}}$).
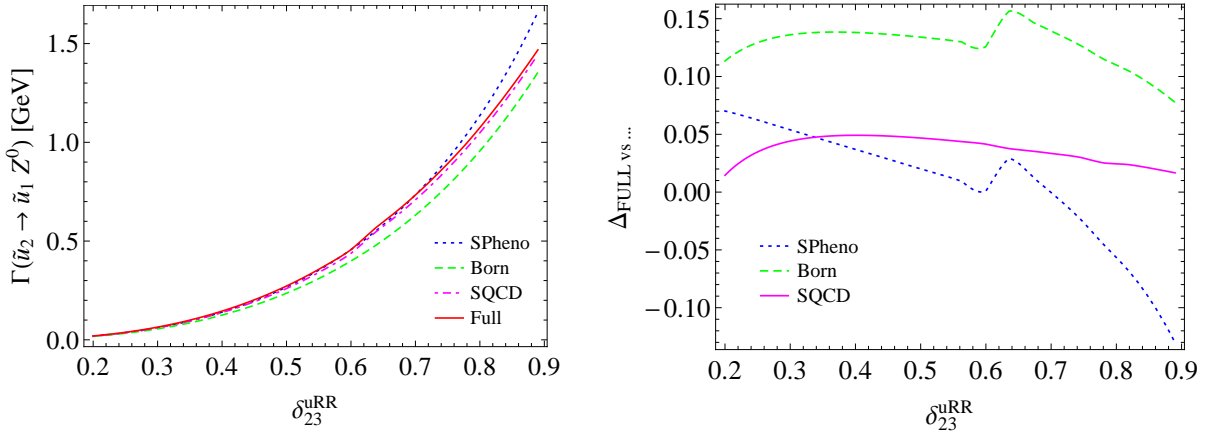
Figure 7.20: Left: The partial decay width $\Gamma(\tilde{u}_2 \to \tilde{u}_1 Z^0)$ as a function of δ_{23}^{uRR} using scenario A as a starting point, comparing the results from SPheno with FVSFOLD (tree-level, SQCD, full one-loop corrections). Right: Relative differences of this decay width, comparing the full one-loop calculation from FVSFOLD with the tree-level ($\Delta_{\text{Full vs Born}}$) and SQCD ($\Delta_{\text{Full vs SQCD}}$) calculation (both from FVSFOLD) as well as with the calculation from SPheno ($\Delta_{\text{Full vs SPheno}}$).

rather small and depend weakly on the QFV parameter. We can thus see that we again cannot neglect the EW contributions in our scenario. The comparison with SPheno shows an overall good agreement with $2-5\%$ relative difference compared to the full one-loop result.

Finally, in Figures 7.25-7.26 we show the total decay width of $\tilde{d}_1$ and the branching ratio $\text{BR}(\tilde{d}_1 \to \tilde{u}_1 W^-)$ as a function of δ_{23}^{uRL} comparing the result from SPheno with the results from FVSFOLD, again presenting the relative differences for better comparison. The EW corrections to the full result can be sizeable, ranging $2-8\%$ for the total decay width and even $5-15\%$ for the BR. Thus once again we conclude that EW corrections are quite relevant in our scenario. Comparing with SPheno reveals a relative difference of $\sim 10\%$ for the BR (with no relevant dependence on δ_{23}^{uRL}) and $3-9\%$ for the total decay width.
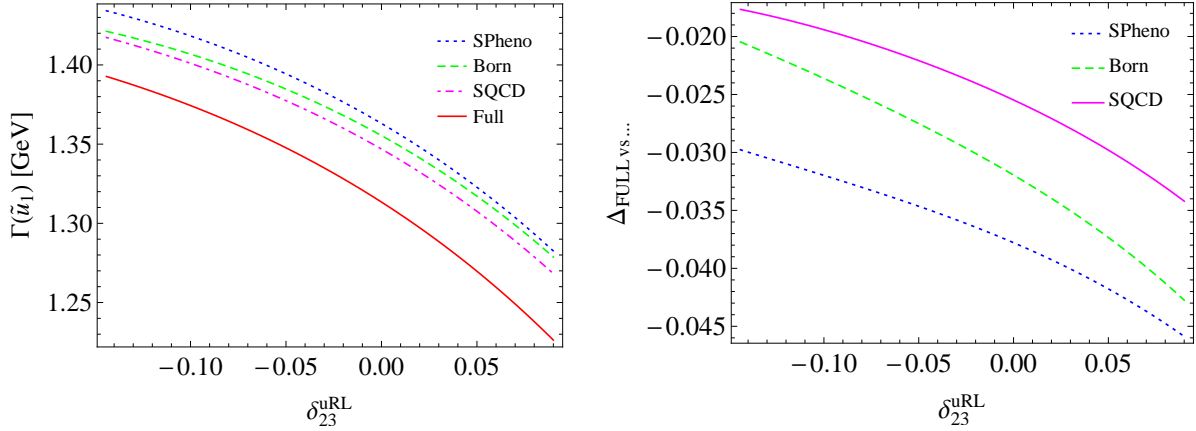
Figure 7.21: Left: Total decay width of $\tilde{u}_1$ as a function of δ_{23}^{uRL} using scenario A as a starting point, comparing the results from SPheno with FVSFOLD (tree-level, SQCD, full one-loop corrections). Right: Relative differences of this $\Gamma(\tilde{u}_1)$, comparing the full one-loop calculation from FVSFOLD with the tree-level ($\Delta_{\text{Full vs Born}}$) and SQCD ($\Delta_{\text{Full vs SQCD}}$) calculation (both from FVSFOLD) as well as with the calculation from SPheno ($\Delta_{\text{Full vs SPheno}}$).
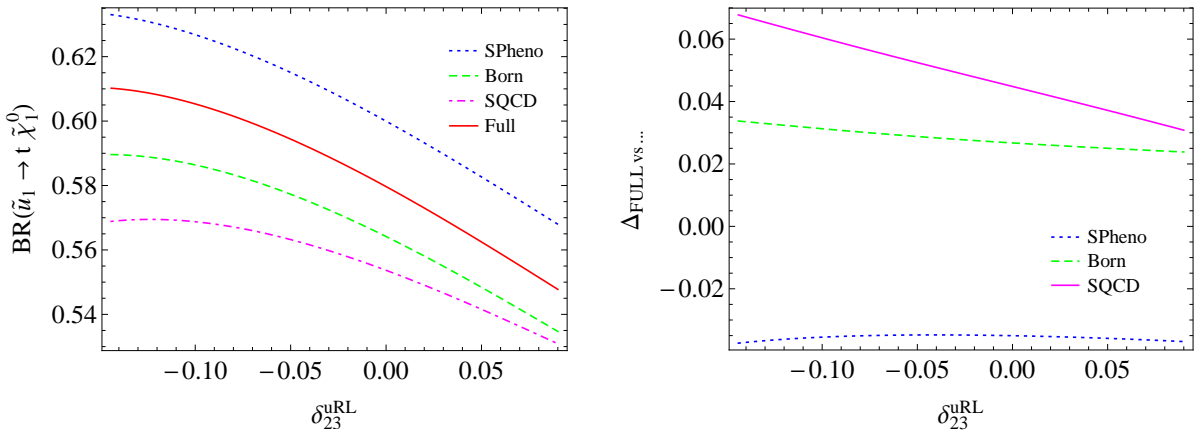

Figure 7.22: Left: The branching ratio $\text{BR}(\tilde{u}_1 \to t\,\tilde{\chi}_1^0)$ as a function of δ_{23}^{uRL} using scenario A as a starting point, comparing the results from SPheno with FVSFOLD (tree-level, SQCD, full one-loop corrections). Right: Relative differences of this BR, comparing the full one-loop calculation from FVSFOLD with the tree-level ($\Delta_{\text{Full vs Born}}$) and SQCD ($\Delta_{\text{Full vs SQCD}}$) calculation (both from FVSFOLD) as well as with the calculation from SPheno ($\Delta_{\text{Full vs SPheno}}$).
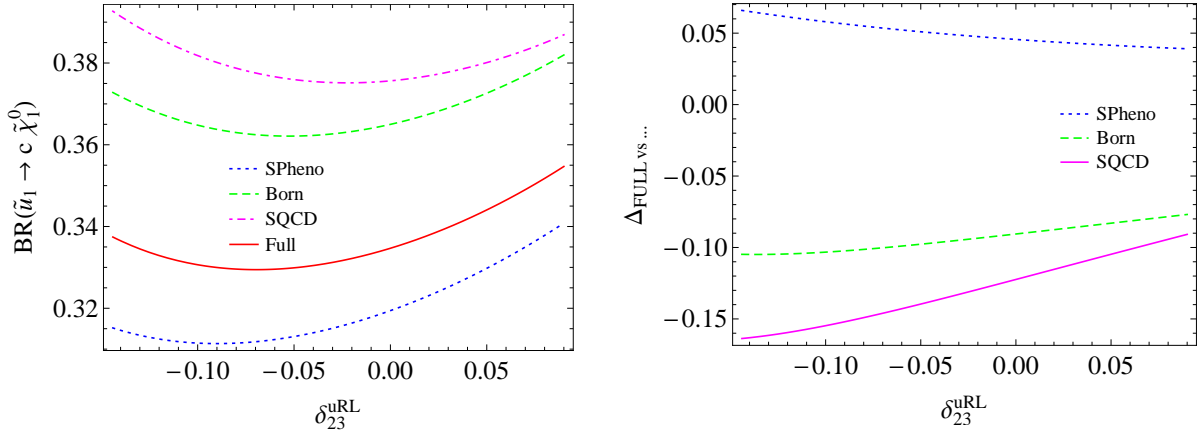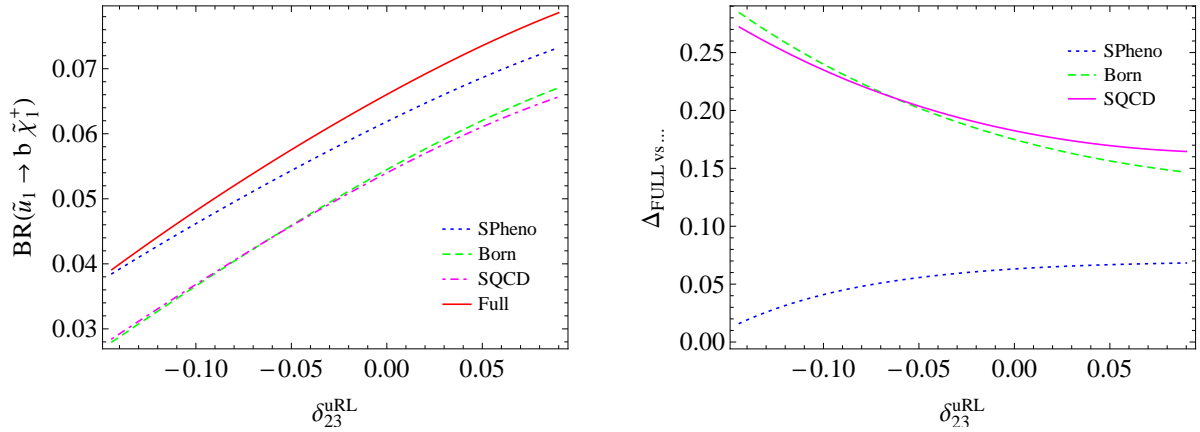
Figure 7.23: Left: The branching ratio $\mathrm{BR}(\tilde{u}_1 \rightarrow c\,\tilde{\chi}_1^0)$ as a function of δ_{23}^{uRL} using scenario A as a starting point, comparing the results from SPheno with FVSFOLD (tree-level, SQCD, full one-loop corrections). Right: Relative differences of this BR, comparing the full one-loop calculation from FVSFOLD with the tree-level ($\Delta_{\mathrm{Full\ vs\ Born}}$) and SQCD ($\Delta_{\mathrm{Full\ vs\ SQCD}}$) calculation (both from FVSFOLD) as well as with the calculation from SPheno ($\Delta_{\mathrm{Full\ vs\ SPheno}}$).

Figure 7.24: Left: The branching ratio $\mathrm{BR}(\tilde{u}_1 \rightarrow b\,\tilde{\chi}_1^+)$ as a function of δ_{23}^{uRL} using scenario A as a starting point, comparing the results from SPheno with FVSFOLD (tree-level, SQCD, full one-loop corrections). Right: Relative differences of this BR, comparing the full one-loop calculation from FVSFOLD with the tree-level ($\Delta_{\mathrm{Full\ vs\ Born}}$) and SQCD ($\Delta_{\mathrm{Full\ vs\ SQCD}}$) calculation (both from FVSFOLD) as well as with the calculation from SPheno ($\Delta_{\mathrm{Full\ vs\ SPheno}}$).

Figure 7.25: Left: Total decay width of $\tilde{d}_1$ as a function of δ_{23}^{uRL} using scenario A as a starting point, comparing the results from SPheno with FVSFOLD (tree-level, SQCD, full one-loop corrections). Right: Relative differences of this $\Gamma(\tilde{d}_1)$, comparing the full one-loop calculation from FVSFOLD with the tree-level ($\Delta_{\text{Full vs Born}}$) and SQCD ($\Delta_{\text{Full vs SQCD}}$) calculation (both from FVSFOLD) as well as with the calculation from SPheno ($\Delta_{\text{Full vs SPheno}}$).
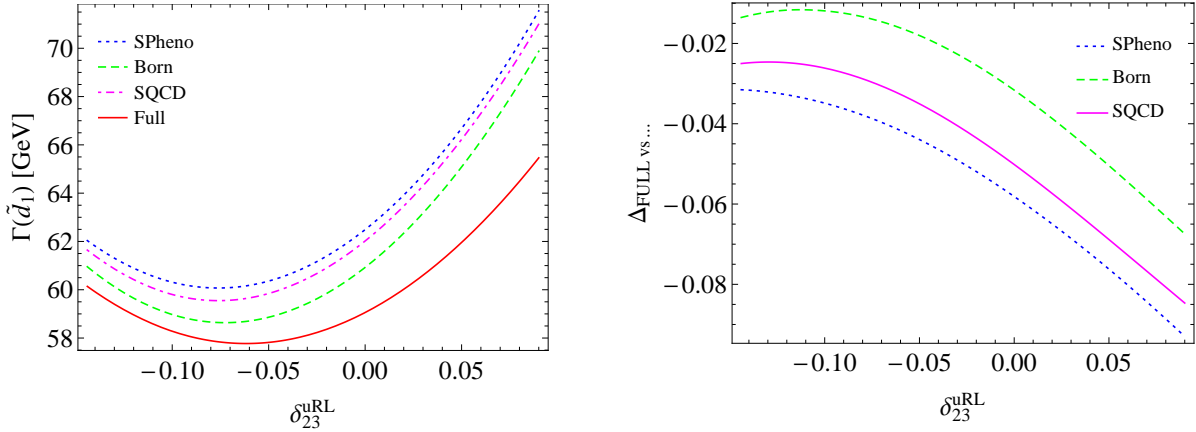

Figure 7.26: Left: The branching ratio $\text{BR}(\tilde{d}_1 \rightarrow \tilde{u}_1 W^-)$ as a function of δ_{23}^{uRL} using scenario A as a starting point, comparing the results from SPheno with FVSFOLD (tree-level, SQCD, full one-loop corrections). Right: Relative differences of this BR, comparing the full one-loop calculation from FVSFOLD with the tree-level ($\Delta_{\text{Full vs Born}}$) and SQCD ($\Delta_{\text{Full vs SQCD}}$) calculation (both from FVSFOLD) as well as with the calculation from SPheno ($\Delta_{\text{Full vs SPheno}}$).
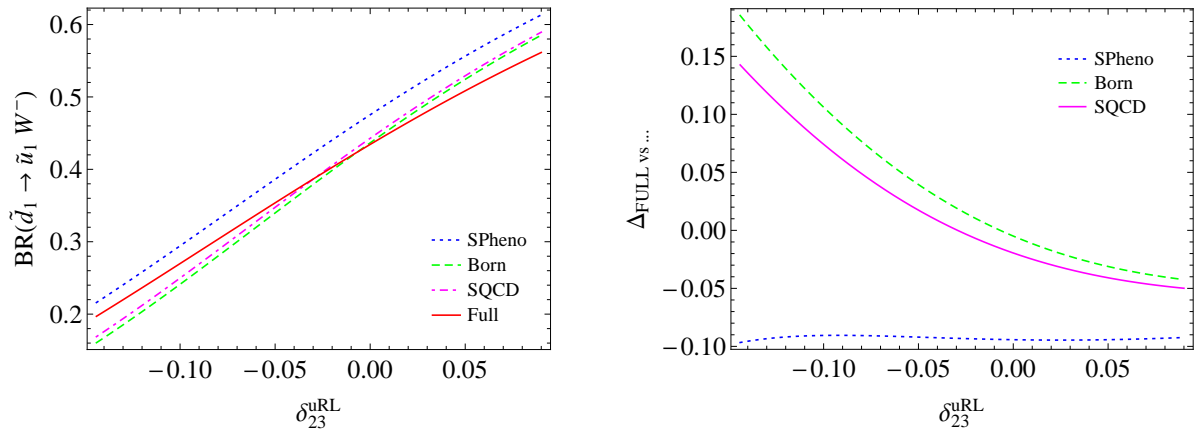
7.4 Conclusions

In this thesis we calculated for the first time all squark and gluino two-body decay widths in the MSSM with general quark flavour violation (QFV) at full one-loop level. We used the $\overline{\text{DR}}$ renormalisation scheme as specified in the SPA convention and included soft and hard photon/gluon bremsstrahlung to our processes. Based on our calculations we developed the first publicly available program package called `FVSFOLD` (Flavour Violating Squark Full One Loop Decays), which computes fully automatically all above-mentioned QFV decays at full one-loop level and makes use of the SLHA2 input/output format. We made extensive cross-checks with SPheno and SFOLD and rigorously checked for UV and IR finiteness.

We presented a case study consisting of two scenarios to demonstrate the QFV functionality and general usefulness of our code. In both scenarios we assumed general QFV mixing between the second and third up-type squark generations and took the most important experimental constraints into account. We compared our full one-loop results with our SUSY-QCD and tree-level calculations and with the results from SPheno. For convenience we also showed the relative differences of these partial results with our full one-loop result. We presented our comparison in tables depicting the decay widths and branching ratios of all squark and gluino decays as well as in various plots as a function of the most important QFV parameters.

We obtained significant deviations of decay widths and branching ratios from the quark flavour conserving case up to $\sim 54\%$ ($\sim 23\%$) in squark (gluino) decays, depending on the QFV parameters. Moreover, we observed that the electroweak contributions can become even larger than the SUSY-QCD corrections (sometimes with opposite sign) and thus cannot be neglected. The comparison with SPheno showed partly good agreement with small relative differences compared to our full one-loop results (primarily in the gluino decays) and partly bigger deviations from the full calculations (mainly in the squark decays).

In view of these results we conclude that it is important to account for possible QFV effects in squark and gluino decays since they can have an influence on the squark and gluino searches at the LHC. Furthermore, it is necessary to include also electroweak corrections when calculating these QFV decays in order to attain an adequate accuracy.

Part II

Computational uncertainties in public $\mathrm{BR}(\overline{B} \to X_s \gamma)$ codes

Chapter 8

Introduction

The inclusive rare meson decay $\overline{B} \to X_s\gamma$ is a loop-induced flavour changing neutral current (FCNC) process which is widely regarded as a sensitive probe for the flavour structure of the Standard Model (SM) and beyond [42, 43]. A possible deviation from the SM prediction can give clues to new physics in the energy range even far beyond the electroweak scale currently accessible by high energy experiments like CMS and ATLAS. Thus studying this rare decay is an important indirect search via virtual corrections and is complementary to the direct searches for new particles and forces.

One of the plausible extensions of the SM is to introduce supersymmetry (SUSY) in the simplest form as Minimal Supersymmetric Standard Model (MSSM). While the SM contributions to the branching ratio $\mathrm{BR}(\overline{B} \to X_s\gamma)$ are only mediated by a $W^\pm$ boson in penguin loops, additional MSSM contributions involving a charged Higgs boson $H^\pm$, a chargino $\tilde{\chi}^\pm$, a neutralino $\tilde{\chi}^0$, or a gluino $\tilde{g}$ can lead to sizeable deviations from the SM prediction. However, when one compares the latest experimental value [44]

$$\mathrm{BR}(\overline{B} \to X_s\gamma)_{\mathrm{exp}}^{E_\gamma > 1.6\ \mathrm{GeV}} = (3.43 \pm 0.21 \pm 0.07) \times 10^{-4} \tag{8.1}$$

with the theoretical SM prediction [45] (including NNLO corrections in pertubative QCD)

$$\mathrm{BR}(\overline{B} \to X_s\gamma)_{\mathrm{SM}}^{E_\gamma > 1.6\ \mathrm{GeV}} = (3.15 \pm 0.23) \times 10^{-4} \tag{8.2}$$

one observes a good agreement within a comparable uncertainty, thus already severely constraining (the flavour structure of) many new physics scenarios. When taking an even more recent SM prediction [46]

$$\mathrm{BR}(\overline{B} \to X_s\gamma)_{\mathrm{SM}}^{E_\gamma > 1.6\ \mathrm{GeV}} = (3.28 \pm 0.23) \times 10^{-4}\ , \tag{8.3}$$

the result is in even better agreement with the experimental value.

Because of the sensitivity of this rare decay to new physics this observable is an important constraint for global fits on SUSY models and for general studies of the MSSM [43, 47, 48, 49, 50, 51, 52, 53, 54, 55, 56]. It is therefore very important to have a good assessment of the theoretical and computational uncertainties involved in the complex calculation of the SM and MSSM contributions to $\mathrm{BR}(\overline{B} \to X_s\gamma)$, including the differences in the implementations and/or approximations used in public computational $\mathrm{BR}(\overline{B} \to X_s\gamma)$ tools.

We study these uncertainties and their impact on SUSY parameter fits by employing two detailed numerical studies comparing the public codes `SuperIso`, `SusyBSG`, `SPheno`, and `microMEGAs`. We perform both studies within the phenomenological MSSM (pMSSM) with a reduced parameter set. In the first study, we employ a uniform random scan in the reduced pMSSM parameter space in order to quantify the relative differences of the $\mathrm{BR}(\overline{B} \to X_s\gamma)_{\mathrm{MSSM}}$ values as a function of the input parameters and relevant sparticle and Higgs masses. In the second study, we evaluate the implication of different $\mathrm{BR}(\overline{B} \to X_s\gamma)$ values on SUSY fits by performing a global Bayesian analysis using Markov Chain Monte Carlo (MCMC) techniques, resulting in posterior probability density functions (PDFs) of parameters and derived observables. By comparing the posterior PDFs obtained from different $\mathrm{BR}(\overline{B} \to X_s\gamma)$ calculations one can demonstrate the sensitivity of these global fits on this uncertainty.

The work is organised as follows: in Chapter 9 we summarise the current status of the SM and MSSM predictions for $\mathrm{BR}(\overline{B} \to X_s\gamma)$ as well as the various implementations found in the public codes. In Chapter 10 we explain in detail the setup of the two numerical studies. In Chapter 11 we present the results of our two studies and conclude our findings.

Chapter 9

Calculation of $\mathrm{BR}(\overline{B} \to X_s\gamma)$

In this chapter we review the current status of the SM and MSSM predictions for the branching ratio $\mathrm{BR}(\overline{B} \to X_s\gamma)$ as well as the various implementations found in the computer programs.

9.1 Status of $\mathrm{BR}(\overline{B} \to X_s\gamma)$ calculation

The calculation of the pertubative QCD corrections to $\mathrm{BR}(\overline{B} \to X_s\gamma)_{\mathrm{SM}}$ is complicated by the presence of different mass scales which induce large logarithms at each order in fixed-order pertubation theory, making this approach not applicable. Instead, one uses an effective field theory approach by way of the Operator Product Expansion (OPE) in order to set up an expansion in RG improved pertubation theory. The Wilson coefficients C_i of the effective Lagrangian are obtained at a high scale $\mu \sim M_W$ by matching between the full SM and the effective theory, and then evolved via RGEs down to a low scale $\mu \sim m_b$. The Wilson coefficients and the anomalous dimensions for the RG evolution required for the most recent NNLO calculation have been obtained in [57, 58] and [59, 60, 61], respectively. The calculation of $\mathrm{BR}(\overline{B} \to X_s\gamma)_{\mathrm{SM}}$ from this effective Lagrangian with a cut on the photon energy is completely known at NLO [62], whereas at NNLO the result is only partly exact with an estimate of the remaining NNLO corrections [63]. The final result for SM after taking into account all previously mentioned NNLO pertubative QCD calculations is $\mathrm{BR}(\overline{B} \to X_s\gamma)_{\mathrm{SM}}^{E_\gamma > 1.6 \text{ GeV}} = (3.15 \pm 0.23) \times 10^{-4}$ [45], including the leading non-pertubative and electroweak effects as well. The total uncertainty stems from non-pertubative (5%), parametric (3%), pertubative (3%), and charm quark mass interpolation uncertainties (3%), which are added in quadrature. By re-evaluating the non-pertubative parameters one obtains a slightly higher value $\mathrm{BR}(\overline{B} \to X_s\gamma)_{\mathrm{SM}}^{E_\gamma > 1.6 \text{ GeV}} = (3.28 \pm 0.23) \times 10^{-4}$ [46], in even better agreement with the experimental value.

In the MSSM new contributions to $\mathrm{BR}(\overline{B} \to X_s\gamma)_{\mathrm{MSSM}}$ mediated by a charged Higgs boson $H^\pm$, a chargino $\tilde{\chi}^\pm$, a neutralino $\tilde{\chi}^0$, or a gluino $\tilde{g}$ can be absorbed into the Wilson coefficients C_i of the above SM-only calculation. Currently a NLO calculation [64, 65, 66, 67, 68, 69] is available for the MSSM under the simplifying assumption of Minimal Flavour Violation (MFV), according to which the quark and squark mass matrices can

be simultaneously diagonalised and the only source of flavour violation is the CKM matrix. At present only a LO calculation is available for MSSM scenarios beyond MFV. Some of the corrections are $\tan\beta$-enhanced and need to be resummed if applicable.

9.2 Public BR($\overline{B} \to X_s\gamma$) codes

Several computer programs include calculations of BR($\overline{B} \to X_s\gamma$). We choose the following codes because they are publicly available, widely used and employ dedicated routines for the calculation: `SuperIso 3.4beta` [70, 71], `SusyBSG 1.5` [72], `SPheno 3.2.3` [38, 39], and `micrOMEGAs 3.1` [73]. We compare the implementations separately for SM and SUSY contributions within the MSSM.

9.2.1 SM contributions

- `SuperIso` includes the full implementation of the NNLO calculation [45]. This leads to BR($\overline{B} \to X_s\gamma$)$_{\text{SM}} = (3.08 \pm 0.24) \times 10^{-4}$ with the updated PDG inputs values.

- `SusyBSG` implements a NLO calculation [74] but improves it by adjusting the renormalisation scale μ_c (at which $m_c(\mu_c)^{\overline{\text{MS}}}$ enters the SM contributions to the Wilson coefficients) to reproduce the NNLO result [46] with BR($\overline{B} \to X_s\gamma$)$_{\text{SM}} = 3.28 \times 10^{-4}$.

- `SPheno` currently has no dedicated calculation implemented but directly takes the NNLO result of [45, 75] by setting BR($\overline{B} \to X_s\gamma$)$_{\text{SM}} = 2.98 \times 10^{-4}$ as a fixed value.

- `micrOMEGAs` [76, 77] includes a NLO calculation [78] but improves it by appropriately choosing the scale for the c quark mass to reproduce the NNLO result [45, 63, 46]. With updated default values for the experimentally determined quantities the SM result is BR($\overline{B} \to X_s\gamma$)$_{\text{SM}} = 3.27 \times 10^{-4}$.

9.2.2 SUSY contributions

- `SuperIso` incorporates the NNLO charged Higgs contributions [79], as well as partial NNLO calculation in the MSSM with MFV, using an effective field theory approach based on [80], [68] and [45].

- `SusyBSG` [72] implements a NLO calculation [74, 64] in the MSSM with MFV (as well as a LO calculation in MSSM scenarios with a generic non-MFV flavour structure), including the complete NLO SUSY-QCD corrections along with full gluino contributions [69]. Large $\tan\beta$-enhanced contributions are properly taken into account. Optionally the code comprises additional LO contributions from diagrams with gluinos as well as charginos that become relevant when the MFV condition is imposed at a scale much higher than the electroweak scale.

- `SPheno` implements the NLO calculation of [81, 82, 83] in the MSSM with MFV, as well as a LO calculation in MSSM scenarios with a generic non-MFV flavour structure.

- `micrOMEGAs` [76, 77] includes charged Higgs contributions at NLO based on [74] as well as LO contributions from charginos following [66] which are improved by taking into account Δm_b corrections and large $\tan \beta$ effects. Currently no contributions with MFV squarks are implemented and the only flavour violation stems from the CKM matrix in the quark sector (thus only the SUSY Les Houches Accord (SLHA1) [84] input format is supported).

Chapter 10

Analysis

In order to compare the public $\mathrm{BR}(\overline{B} \to X_s\gamma)$ codes as well as to assess the implication for SUSY fits, we employ two numerical studies which are explained in detail below.

We perform both studies within the phenomenological MSSM (pMSSM) with a reduced parameter set. The pMSSM is a 19-dimensional parametrisation of the MSSM with real parameters that captures most of its phenomenological features, going beyond more constrained SUSY models. However, when focusing on the relevant parameters for the $\mathrm{BR}(\overline{B} \to X_s\gamma)$ calculation one can reduce the parameter set down to six dimensions: $\tan\beta$ (ratio of the Higgs VEVs), m_{A^0} (pseudo-scalar Higgs pole mass), μ (higgsino mass parameter), $M_1(= \frac{1}{2}M_2 = \frac{1}{6}M_3)$ (gaugino mass parameters with approximate gaugino mass unification relation), A_t (top trilinear coupling), and $M_{\widetilde{Q}_3}(= M_{\widetilde{U}_3} = M_{\widetilde{D}_3})$ (3rd generation squark mass parameters with simplifying relation applied). In both studies we vary these six parameters over broad ranges and keep the remaining parameters fixed (see Table 11.1 in the next chapter).

Since `micrOMEGAs` currently cannot handle the SLHA2 input format (needed for MFV in the squark sector) we resort to the SLHA1 input standard for both studies. As a result flavour violation via the CKM matrix is only found in the quark sector and the squark mass matrix remains flavour diagonal.

10.1 Comparison of $\mathrm{BR}(\overline{B} \to X_s\gamma)_{\mathrm{MSSM}}$

In order to compare the different $\mathrm{BR}(\overline{B} \to X_s\gamma)_{\mathrm{MSSM}}$ values we perform a random scan in the reduced pMSSM parameter space.

First we generate 5.5×10^6 pMSSM parameter points chosen by a uniform random number generator within the intervals given in Table 11.1. Then we successively take one parameter point at a time, combine it with our default SM parameter set and feed this information via a SLHA I/O tool [85] to the RGE code `SPheno`. The output at the electroweak scale in SLHA1 format is then forwarded as an input to the programs `SuperIso`, `SusyBSG`, and `micrOMEGAs`. If at any step a program produces an error or the result violates an existing experimental constraint given in Table 10.1, the algorithm discards the currently chosen parameter point and picks the next one. If nothing fails, the values of $\mathrm{BR}(\overline{B} \to X_s\gamma)_{\mathrm{MSSM}}$ of all programs are saved along with the current

parameter point and the algorithm continues until all pMSSM parameter points have been processed. Finally we end up with 226733 data points ($\sim 4.1\%$ of the originally generated amount) for our analysis. This steep drop in numbers of "surviving" data points stems mainly from the stringent Higgs mass constraint.

Observable	Constraint
$m_{\tilde{l}}$, $m_{\tilde{\chi}_1^\pm}$	LEP bounds
LSP	$\tilde{\chi}_1^0$
$m_{\tilde{g}}$	≥ 1 TeV
m_{h^0}	$[121, 129]$ GeV

Table 10.1: Relevant experimental constraints coming from LEP (mass bounds for charged leptons and charginos), SUSY/cosmology (CDM candidate needs to be the lightest neutralino) and LHC [23, 86] (gluino mass bound and Higgs mass range).

Finally, to quantify the relative differences of the $\mathrm{BR}(\overline{B} \to X_s\gamma)_\mathrm{MSSM}$ values we define the measures

$$\Delta_\mathrm{MSSM} \equiv \frac{\mathrm{Max}(\mathrm{BR}(\overline{B} \to X_s\gamma)^i_\mathrm{MSSM}) - \mathrm{Min}(\mathrm{BR}(\overline{B} \to X_s\gamma)^i_\mathrm{MSSM})}{\mathrm{Mean}(\mathrm{BR}(\overline{B} \to X_s\gamma)^i_\mathrm{MSSM})} \tag{10.1}$$

when comparing all programs at once and

$$\Delta_\mathrm{MSSM} \equiv \frac{\mathrm{BR}(\overline{B} \to X_s\gamma)^A_\mathrm{MSSM} - \mathrm{BR}(\overline{B} \to X_s\gamma)^B_\mathrm{MSSM}}{\mathrm{BR}(\overline{B} \to X_s\gamma)^A_\mathrm{MSSM}} \tag{10.2}$$

when comparing two programs A and B. In addition, we modify the above definitions and specify

$$\Delta_\mathrm{MSSM/SM} \equiv \frac{\mathrm{Max}(\mathrm{BR}(\overline{B} \to X_s\gamma)^i_\mathrm{MSSM/SM}) - \mathrm{Min}(\mathrm{BR}(\overline{B} \to X_s\gamma)^i_\mathrm{MSSM/SM})}{\mathrm{Mean}(\mathrm{BR}(\overline{B} \to X_s\gamma)^i_\mathrm{MSSM/SM})} \tag{10.3}$$

as well as

$$\Delta_\mathrm{MSSM/SM} \equiv \frac{\mathrm{BR}(\overline{B} \to X_s\gamma)^A_\mathrm{MSSM/SM} - \mathrm{BR}(\overline{B} \to X_s\gamma)^B_\mathrm{MSSM/SM}}{\mathrm{BR}(\overline{B} \to X_s\gamma)^A_\mathrm{MSSM/SM}} \; . \tag{10.4}$$

By taking the ratio of the MSSM over SM value of each program, the differences in $\mathrm{BR}(\overline{B} \to X_s\gamma)_\mathrm{SM}$ as well as in the hadronic parameters cancel, enabling us to compare the SUSY-only contributions to $\mathrm{BR}(\overline{B} \to X_s\gamma)$.[1]

---

[1]Alternatively, one could also take the difference MSSM minus SM, but that way the different hadronic parameters do not cancel and $\Delta_\mathrm{MSSM-SM}$ can become numerically unstable.

10.2 Impact on SUSY fits

We evaluate the implication of different $\mathrm{BR}(\overline{B} \to X_s \gamma)$ values on SUSY fits by performing a global Bayesian analysis (see e.g. [87]), obtaining posterior probability density functions (PDFs) of parameters θ and derived observables $\mu(\theta)$.

First we combine our parameters and observables to $\phi \equiv \theta, \mu$ where θ denotes the six pMSSM parameters $\tan\beta$, m_{A^0}, μ, $M_1(= \frac{1}{2}M_2 = \frac{1}{6}M_3)$, A_t, and $M_{\tilde{Q}_3}(= M_{\tilde{U}_3} = M_{\tilde{D}_3})$ as well as the two SM parameters m_t and $\alpha_s(M_Z)$ (which are both treated as nuisance parameters). The derived observables $\mu \equiv \mu_1, \ldots, \mu_6$ with their associated measurements $D \equiv D_1, \ldots, D_6$ and likelihood functions $L(D_i|\mu_i)$ are specified in Table 10.2. Since

i	Observable μ_i	Experimental result D_i	Likelihood function $L(D_i\|\mu_i)$
1	$\mathrm{BR}(\overline{B} \to X_s\gamma)$	$(3.43 \pm 0.22) \times 10^{-4}$	Gaussian
2	Δa_μ	$(23.9 \pm 7.9) \times 10^{-10}$	Gaussian
3	m_t	173.5 ± 1.0 GeV	Gaussian
4	$\alpha_s(M_Z)$	0.1184 ± 0.0007	Gaussian
5	m_{h^0}	125.7 ± 0.42 GeV	Gaussian
6	$m_{\tilde{g}}, m_{\tilde{l}},$	see Table 10.1	$L_6 = 1$ if allowed,
	$m_{\tilde{\chi}_1^\pm}$, LSP		$L_6 = 10^{-12}$ if excluded

Table 10.2: Experimental results [44, 23, 86] from various observables and their respective likelihood functions, e.g. for the Gaussian case $L(D_i|\mu_i) \propto \exp(-0.5((\mu_i-D_i)/\sigma_i)^2)$.

these measurements are independent we can construct the likelihood function $L(D|\mu) = \prod_i L(D_i|\mu_i)$. Finally, we compose the joint likelihood function $L(D|\phi) = L(D|\theta)L(D|\mu)$, choose a flat[2] prior $\pi(\phi)$ and use Bayes theorem to derive the posterior PDF $p(\phi|D) \propto L(D|\phi)\pi(\phi)$.

We approximate $p(\phi|D)$ by drawing a sample of 1.68×10^6 parameter points using the Markov Chain Monte Carlo (MCMC) Metropolis-Hastings algorithm [89]. Our parameter scan employs 24 Markov chains (length of 70000 each) in parallel to sample the eight dimensional parameter space θ within the pMSSM (Table 11.1) and SM intervals (Table 10.2). After discarding the first 30000 steps of each chain ("burn-in") and checking that they converged[3], we mix all chains together to summarise the target distribution. At each step in every chain we use the RGE tool `SPheno` and interface the output via SLHA1 to `SuperIso`, `SusyBSG`, and `micrOMEGAs` to calculate the observables listed in Table 10.2.

Finally, since we are interested in the impact of different $\mathrm{BR}(\overline{B} \to X_s\gamma)$ values $(=\mu_1)$ on SUSY fits we run two exemplary MCMC scans, one with the $\mathrm{BR}(\overline{B} \to X_s\gamma)$

---

[2]Note that for a Gaussian density the reference prior is a flat prior (see e.g. [88] and references therein).

[3]We monitor the level of convergence using within/between chain analyses like trace plots, quantile-quantile plots and the "potential scale reduction factor" $\widehat{R}$ [90].

computation coming from `SuperIso` and one from `SusyBSG`. We analyse the outcome of these separate samples by marginalizing each posterior PDF $p(\phi|D)$ to directly compare these PDF predictions of parameters $p(\theta|D)$ and observables $p(\mu|D)$.

Chapter 11

Results and conclusions

We now present the results of our two analyses introduced in detail in the previous chapter and conclude our findings.

In Table 11.1 we summarise our SM [23] and reduced pMSSM input parameter values which we use in our studies. All pMSSM parameters except $\tan\beta$ are defined at the electroweak scale $Q = \sqrt{m_{\tilde{t}_1} m_{\tilde{t}_2}}$.

11.1 Comparison of $\mathrm{BR}(\overline{B} \to X_s\gamma)_{\mathrm{MSSM}}$

11.1.1 Comparing all programs

In Figure 11.1 we show the distribution of data points as density histograms comparing the programs `SuperIso`, `SusyBSG`, `SPheno`, and `micrOMEGAs` as a function of Δ_{MSSM} and $\Delta_{\mathrm{MSSM/SM}}$ as well as the mean of $\mathrm{BR}(\overline{B} \to X_s\gamma)_{\mathrm{MSSM}}$ from each program. The 68% (95%) probability contours[1] are drawn in grey (cyan). As already anticipated, the programs agree much better with each other when taking the ratio $\Delta_{\mathrm{MSSM/SM}}$, since that way not only the differences in $\mathrm{BR}(\overline{B} \to X_s\gamma)_{\mathrm{SM}}$ but also the hadronic parameters of each program cancel. We can further quantify this feature by taking the favoured data points where the mean of $\mathrm{BR}(\overline{B} \to X_s\gamma)$ lies within the experimental value $\pm 3\sigma$ in Eq. (8.1) and marginalise over $\mathrm{BR}(\overline{B} \to X_s\gamma)$. For Δ_{MSSM} the resulting probability histogram has a maximum at 10.3% and the 68% (95%) probability intervals are $[8.1, 13.1]\%$ ($[5.1, 24.5]\%$). For $\Delta_{\mathrm{MSSM/SM}}$ the maximum is at 2.7% and the 68% (95%) probability intervals are $[1.3, 6.9]\%$ ($[0.7, 19.5]\%$).

Figure 11.2 shows density histograms comparing all codes as a function of $\Delta_{\mathrm{MSSM/SM}}$ and of the reduced pMSSM input parameters. Here we only accept data points when at least one program yields a $\mathrm{BR}(\overline{B} \to X_s\gamma)$ value within the experimental value $\pm 3\sigma$ at that point. The 68% (95%) probability contours are again drawn in grey (cyan). The distinct gaps in the plots as a function of M_1, μ and A_t can be explained as follows: due to the approximate gaugino mass unification relation $M_1 : M_2 : M_3 = 1 : 2 : 6$ and $m_{\tilde{g}} \propto M_3$ together with the lower mass limit $m_{\tilde{g}} \geq 1$ TeV small $|M_1|$ values are disallowed; small

---

[1]We calculate the contours by choosing the minimal area that contains the 68% or 95% of the total volume.

SM Parameter	Value
$\alpha_{\mathrm{em}}^{-1}(M_Z)$	127.932319
G_F	$1.16637 \times 10^{-5}\,\mathrm{GeV}^{-2}$
$\alpha_{\mathrm{s}}(M_Z)^{\overline{\mathrm{MS}}}$	0.1184
M_Z	91.1876 GeV
M_t	173.5 GeV
$m_b(m_b)^{\overline{\mathrm{MS}}}$	4.18 GeV
$m_c(m_c)^{\overline{\mathrm{MS}}}$	1.275 GeV
λ	0.22535
A	0.811
$\overline{\rho}$	0.131
$\overline{\eta}$	0.345

pMSSM Parameter	Value
$\tan\beta(M_Z)$	$[2, 50]$
m_{A^0}	$[100, 2000]$ GeV
μ	$[-3000, 3000]$ GeV
$M_1(= \frac{1}{2}M_2 = \frac{1}{6}M_3)$	$[-1500, 1500]$ GeV
A_t	$[-9000, 9000]$ GeV
$M_{\widetilde{Q}_3}(= M_{\widetilde{U}_3} = M_{\widetilde{D}_3})$	$[300, 3000]$ GeV
A_b, A_τ	0 GeV
$M_{\widetilde{L}_{1,2}}, M_{\widetilde{E}_{1,2}}, M_{\widetilde{Q}_{1,2}}, M_{\widetilde{U}_{1,2}}, M_{\widetilde{D}_{1,2}}$	5000 GeV
$M_{\widetilde{L}_3}, M_{\widetilde{E}_3}$	1000 GeV

Table 11.1: All relevant SM and reduced pMSSM input parameter values used in our analyses.
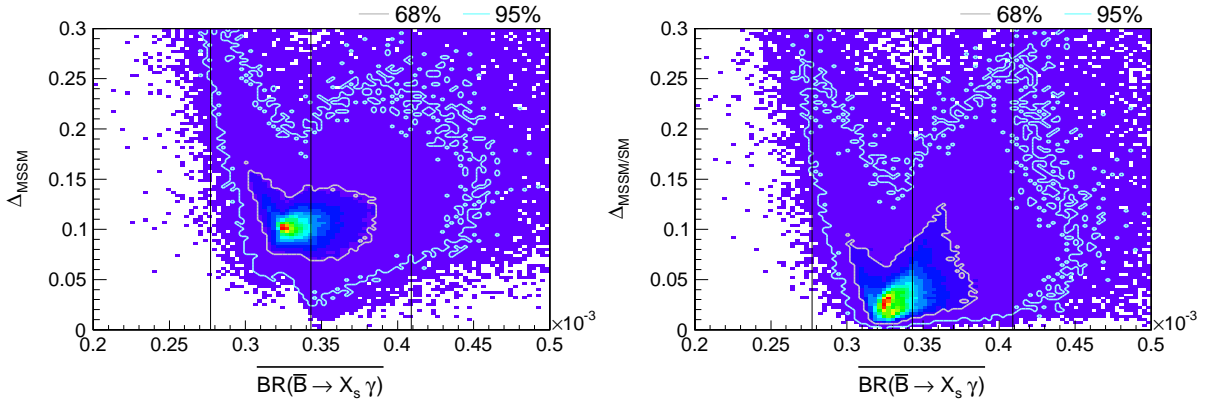
Figure 11.1: Density histograms comparing the programs `SuperIso`, `SusyBSG`, `SPheno`, and `micrOMEGAs` with Δ_{MSSM} (left) and $\Delta_{\text{MSSM/SM}}$ (right) as a function of the averaged BR($\overline{B} \to X_s\gamma$)$_{\text{MSSM}}$ of the four programs. The 68% (95%) probability contours are drawn in grey (cyan). The three vertical lines denote the experimental value BR($\overline{B} \to X_s\gamma$)$_{\text{exp}} \pm 3\sigma$.

$|\mu|$ values are forbidden because of the chargino mass bound $m_{\tilde{\chi}_1^\pm} \geq 103$ GeV and small $|A_t|$ values are disfavoured because of the necessary stop mass splitting needed to obtain a Higgs mass in the desired [121, 129] GeV mass range. The main contributions to BR($\overline{B} \to X_s\gamma$) stem from chargino/stop loops and charged Higgs/top loops, with corrections from gluinos. These contributions become larger for lighter masses and larger $\tan\beta$. Larger contributions can in turn lead to larger discrepancies, which is exactly what can be observed in these plots: larger discrepancies correspond to large $\tan\beta$, small M_1 ($M_2 = 2M_1 \sim m_{\tilde{\chi}_1^\pm}$ and $M_3 = 6M_1 \sim m_{\tilde{g}}$) and small μ ($\sim m_{\tilde{\chi}_1^\pm}$), moderate A_t (for sufficient large stop mass splitting), small $M_{\tilde{Q}_3}$ ($\sim m_{\tilde{t}_1}$), and small m_{A^0} ($\sim m_{H^\pm}$).

In Figure 11.3 we present density histograms comparing all programs as a function of $\Delta_{\text{MSSM/SM}}$ and of some sparticle and Higgs masses. Again we only take data points when at least one program yields a BR($\overline{B} \to X_s\gamma$) value within the experimental value $\pm 3\sigma$. The 68% (95%) probability contours are drawn in grey (cyan). As already explained in the interpretation of the previous figure, larger contributions due to lighter masses in the loops can cause larger discrepancies between the programs. This assumption can be again confirmed by examining the good agreement between larger discrepancies and lighter masses (especially the masses for $\tilde{\chi}_1^\pm$, $\tilde{t}_1$, and $H^\pm$ since they belong to the main contributions) in these plots.
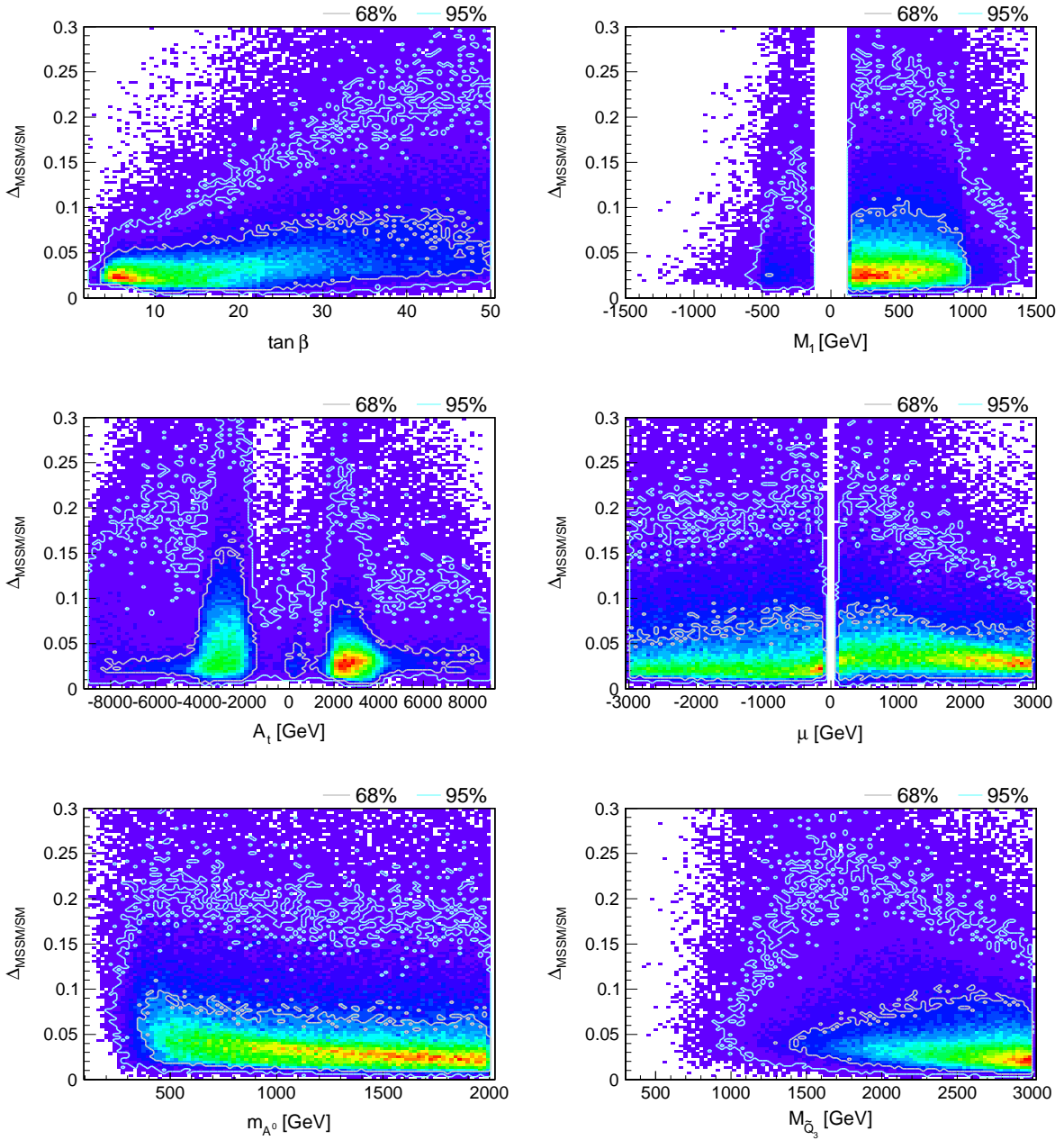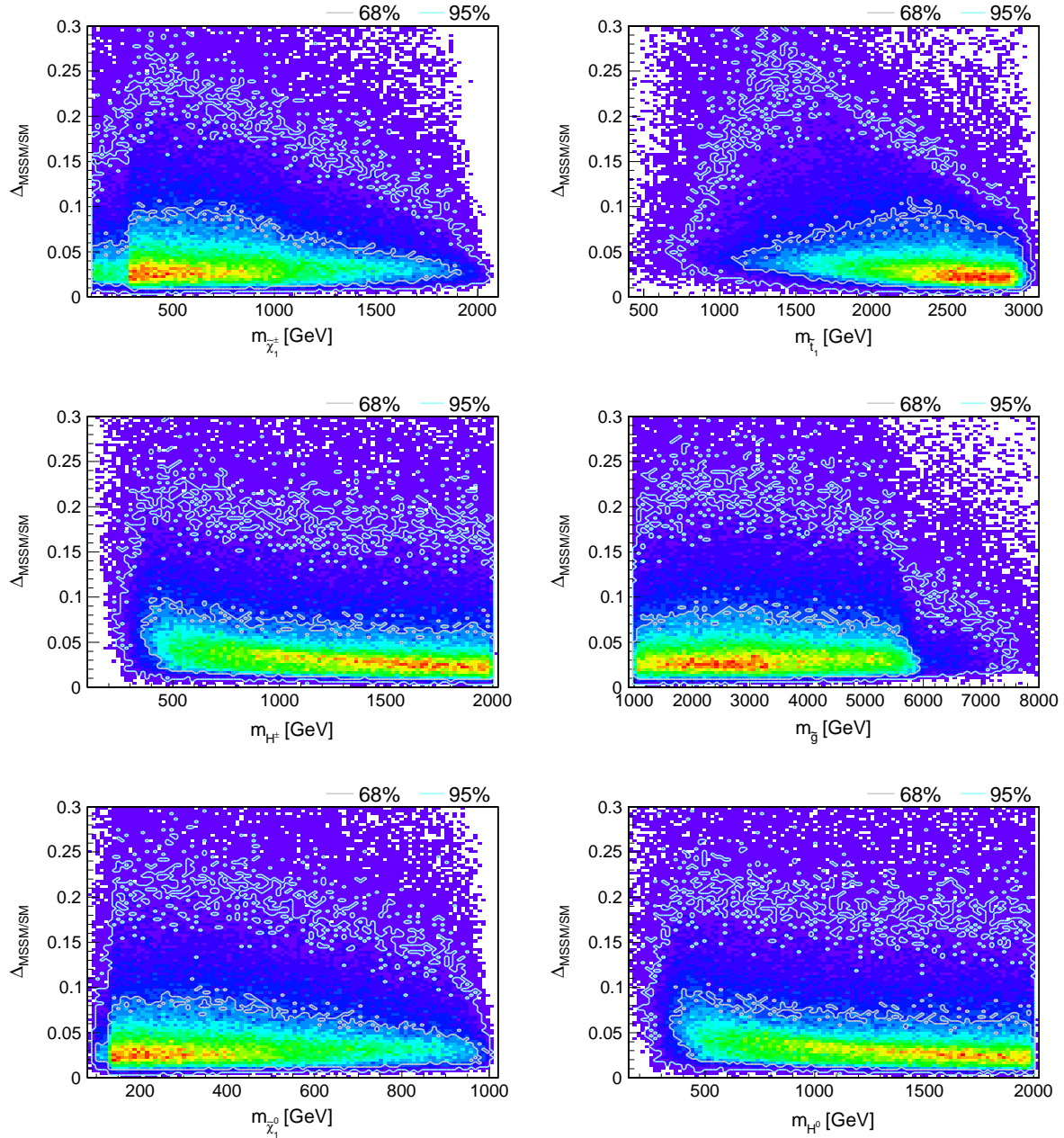
Figure 11.2: Density histograms comparing all programs as a function of $\Delta_{\mathrm{MSSM/SM}}$ and of the pMSSM input parameters. Only data points where at least one program yields a $\mathrm{BR}(\overline{B} \to X_s\gamma)$ value within the experimental value $\pm 3\sigma$ are shown. The 68% (95%) probability contours are drawn in grey (cyan). Note that the relations $M_1 = \frac{1}{2}M_2 = \frac{1}{6}M_3$ and $M_{\widetilde{Q}_3} = M_{\widetilde{U}_3} = M_{\widetilde{D}_3}$ are always implied.

Figure 11.3: Density histograms comparing all programs as a function of $\Delta_{\mathrm{MSSM/SM}}$ and of some sparticle and Higgs masses. Again only data points where at least one program yields a BR($\overline{B} \to X_s\gamma$) value within the experimental value $\pm 3\sigma$ are shown. The 68% (95%) probability contours are drawn in grey (cyan).

11.1.2 Comparing two programs

Now we focus on the comparison of the programs and compare the `SuperIso` results with the results of `SusyBSG`, `SPheno`, and `micrOMEGAs`, respectively.

Figure 11.4 shows a density histogram comparing `SuperIso` with `SusyBSG` as a function of $\Delta_{\mathrm{MSSM/SM}}$ and of $\mathrm{BR}(\overline{B} \to X_s\gamma)$ from `SuperIso`. As always the 68% (95%) probability contours are drawn in grey (cyan). We can see that for most data points the agreement between these two programs with dedicated and up-to-date $\mathrm{BR}(\overline{B} \to X_s\gamma)$ routines is quite good. Taking again only the favoured data points where $\mathrm{BR}(\overline{B} \to X_s\gamma)_{\mathrm{SuperIso}}$ lies within the experimental value $\pm 3\sigma$ and marginalise over $\mathrm{BR}(\overline{B} \to X_s\gamma)$ we obtain for the $\Delta_{\mathrm{MSSM/SM}}$ probability histogram a maximum at 2.2% and the 68% (95%) probability intervals at $[0.2, 4.2]\%$ ($[-4.6, 7.8]\%$).
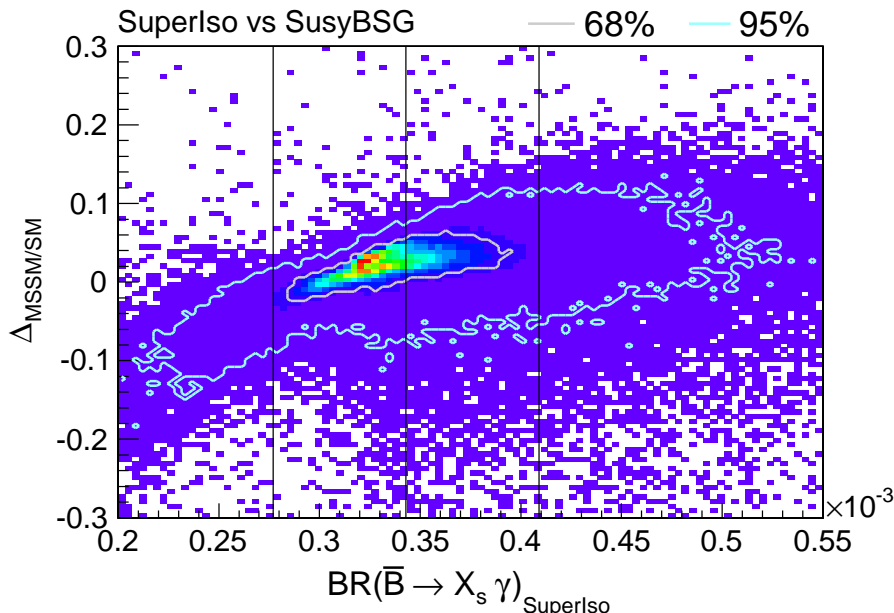

Figure 11.4: Density histogram comparing `SuperIso` with `SusyBSG` as a function of $\Delta_{\mathrm{MSSM/SM}}$ and of $\mathrm{BR}(\overline{B} \to X_s\gamma)$ from `SuperIso` and showing the 68% (95%) probability contours in grey (cyan). The three vertical lines denote the experimental value $\mathrm{BR}(\overline{B} \to X_s\gamma)_{\mathrm{exp}} \pm 3\sigma$.

In Figure 11.5 we plot density histograms comparing `SuperIso` with `SPheno` and with `micrOMEGAs` as a function of $\Delta_{\mathrm{MSSM/SM}}$ and of $\mathrm{BR}(\overline{B} \to X_s\gamma)$ from `SuperIso`. The 68% (95%) probability contours are again drawn in grey (cyan). For most data points the agreement between these programs is reasonably good but slightly worse than compared with `SuperIso` and `SusyBSG`, since both `SPheno` and `micrOMEGAs` do not have the latest $\mathrm{BR}(\overline{B} \to X_s\gamma)$ contributions implemented. Again selecting on the favoured data points where $\mathrm{BR}(\overline{B} \to X_s\gamma)_{\mathrm{SuperIso}}$ lies within the experimental value $\pm 3\sigma$ and marginalise over $\mathrm{BR}(\overline{B} \to X_s\gamma)$ we obtain for the $\Delta_{\mathrm{MSSM/SM}}$ probability histogram the following measures: for the comparison with `SPheno` $\Delta_{\mathrm{MSSM/SM}}$ has a maximum at 0.6% and the

68% (95%) probability intervals at $[-1.8, 4.2]\%$ $([-9.8, 11.0]\%)$ and for the comparison with `micrOMEGAs` the maximum is at 1.0% and the 68% (95%) probability intervals at $[-2.6, 5.4]\%$ $([-11.8, 14.2]\%)$.
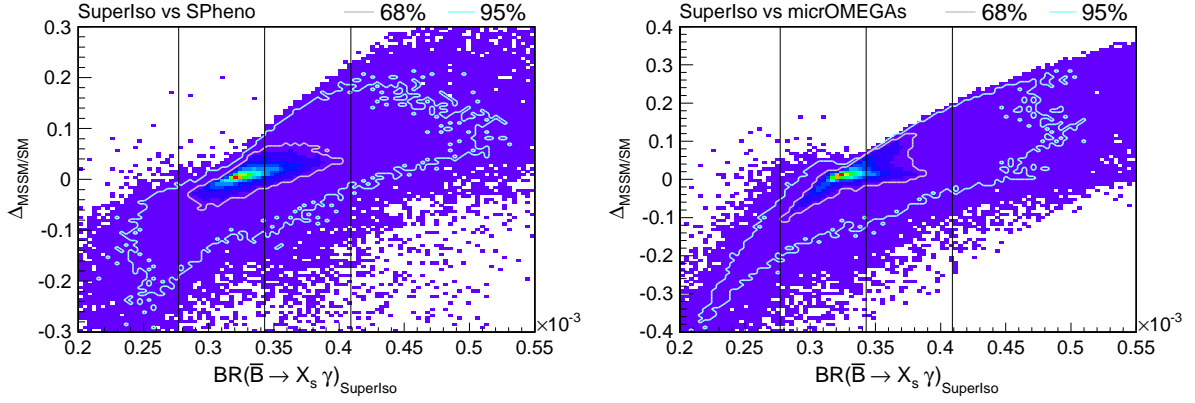

Figure 11.5: Density histograms comparing `SuperIso` with `SPheno` (left) and with `micrOMEGAs` (right) as a function of $\Delta_{\mathrm{MSSM/SM}}$ and of $\mathrm{BR}(\overline{B} \to X_s \gamma)$ from `SuperIso`, showing the 68% (95%) probability contours in grey (cyan). Again, the three vertical lines denote the experimental value $\pm 3\sigma$.

11.2 Impact on SUSY fits

At last we study the impact of $\mathrm{BR}(\overline{B} \to X_s\gamma)$ uncertainties on SUSY fits. In Figure 11.6 we show marginalised 2D posterior PDFs as density histograms derived from our MCMC scans, using Δa_μ from `SuperIso` and $\mathrm{BR}(\overline{B} \to X_s\gamma)$ either from `SuperIso` or from `SusyBSG`. The gap in $\Delta a_\mu \propto \mu$ stems from the chargino mass bound $m_{\tilde{\chi}_1^\pm} \geq 103$ GeV which forbids small $|\mu|$ values. The 68% (95%) Bayesian credible regions (BCR) are shown in grey (cyan). Since both programs use dedicated and up-to-date $\mathrm{BR}(\overline{B} \to X_s\gamma)$ routines with similar results the impact on SUSY fits is rather small. However, we also compared `SuperIso` with `SPheno` having more differing routines which results in a larger influence of $\mathrm{BR}(\overline{B} \to X_s\gamma)$ uncertainties on these fits.
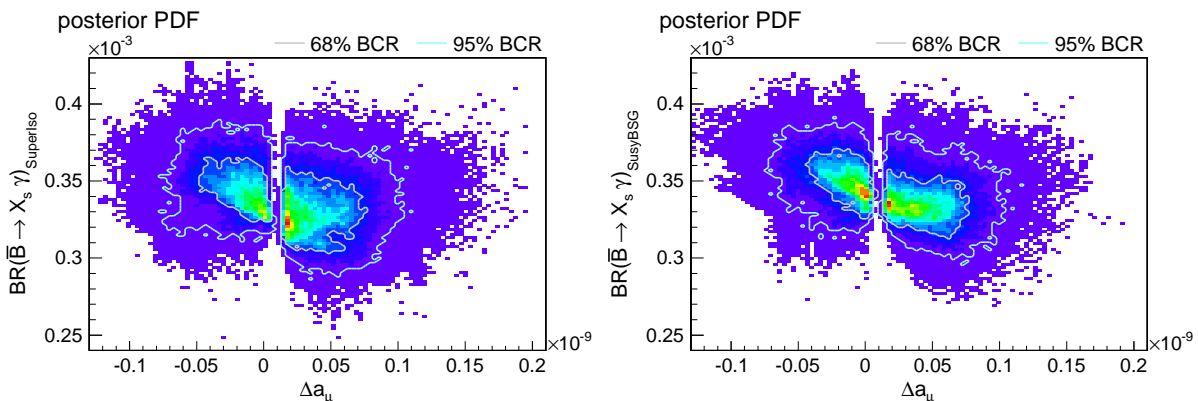

Figure 11.6: Marginalised 2D posterior PDFs using Δa_μ from `SuperIso` and $\mathrm{BR}(\overline{B} \to X_s\gamma)$ from `SuperIso` (left) or from `SusyBSG` (right). The 68% (95%) Bayesian credible regions (BCR) are shown in grey (cyan). The $\pm 3\sigma$ interval of Δa_μ is $[0.02, 4.76] \times 10^{-9}$ (see Table 10.2).

In Figure 11.7 we demonstrate the influences on our SUSY fit in more detail by presenting the marginalised 1D posterior PDFs as a function of the pMSSM input parameters, obtaining different predictions when using $\mathrm{BR}(\overline{B} \to X_s\gamma)$ from `SuperIso` (blue) or from `SusyBSG` (green). The distinct gaps in the plots with μ, A_t and M_1 emerged already in Figure 11.2 and have been explained there. One can observe differing posterior PDF predictions for the parameters m_{A^0}, A_t and μ as well as good agreement for the remaining parameters. The predictions for A_t and μ are negatively correlated for each program because of the off-diagonal stop mass matrix element $m_t(A_t - \mu/\tan\beta)$. As a result, even though one obtains different predictions for A_t and μ the posterior PDFs for $m_{\tilde{t}_1}$ (as seen in Figure 11.9) are in good agreement with each other. The discrepancy in the prediction for m_{A^0} ($\sim m_{H^\pm}$, see also Figure 11.9) may be related to the fact that `SuperIso` and `SusyBSG` are not at the same order for the charged Higgs contributions (NNLO for `SuperIso` vs. NLO for `SusyBSG`).

Figure 11.8 shows additional marginalised 2D posterior PDFs as a function of some pMSSM input parameters, using $\mathrm{BR}(\overline{B} \to X_s\gamma)$ from `SuperIso` (left column) or from
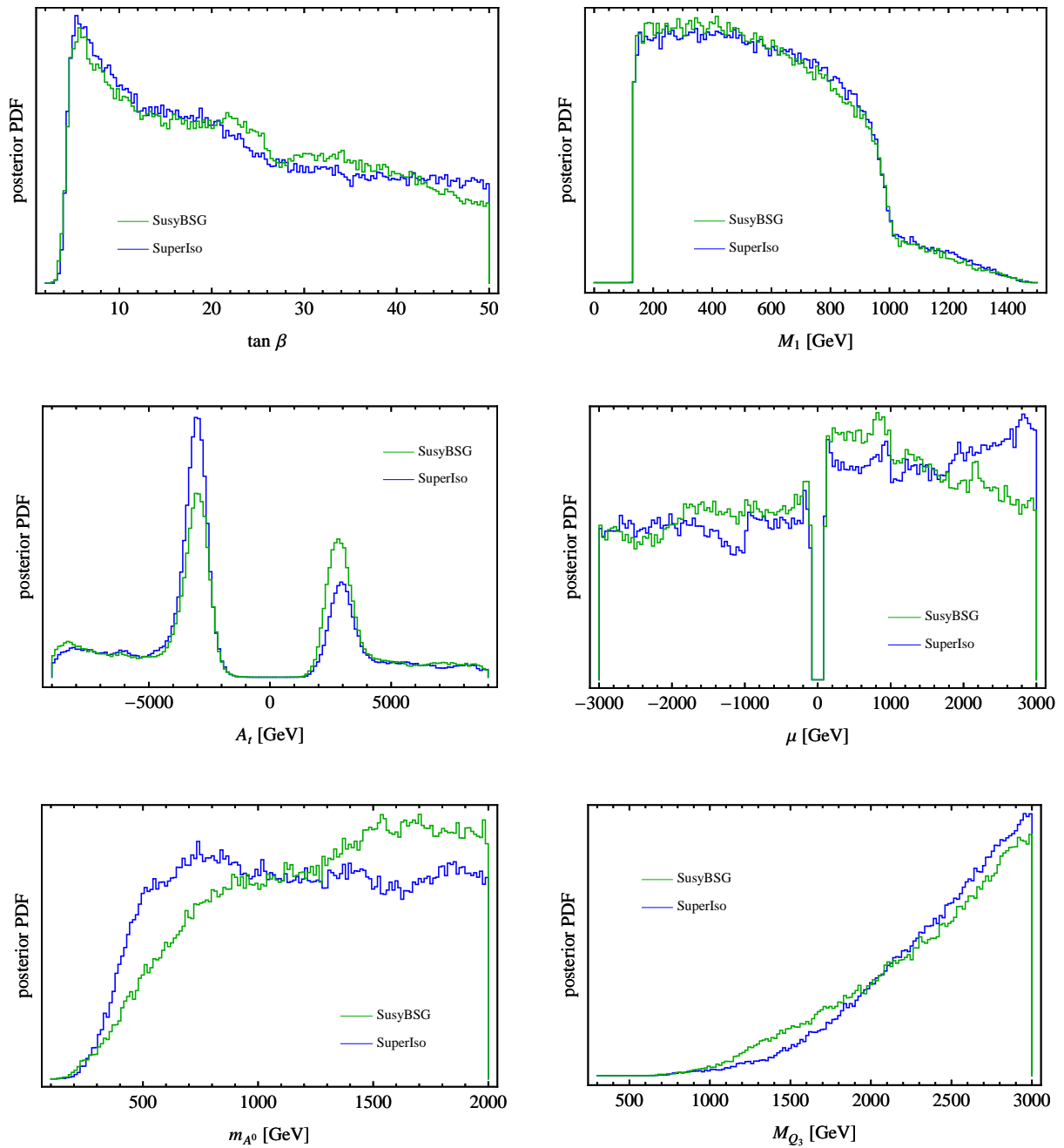
Figure 11.7: Marginalised 1D posterior PDFs as a function of the pMSSM input parameters, using $\mathrm{BR}(\overline{B} \to X_s \gamma)$ from `SuperIso` (blue) or from `SusyBSG` (green). Note that the relations $M_1 = \frac{1}{2}M_2 = \frac{1}{6}M_3$ and $M_{\widetilde{Q}_3} = M_{\widetilde{U}_3} = M_{\widetilde{D}_3}$ are always implied.

SusyBSG (right column). Again one can observe different posterior PDF predictions for the parameters μ, A_t and m_{A^0} when using distinct $\mathrm{BR}(\overline{B} \to X_s\gamma)$ as already seen in somewhat clearer detail in Figure 11.7.
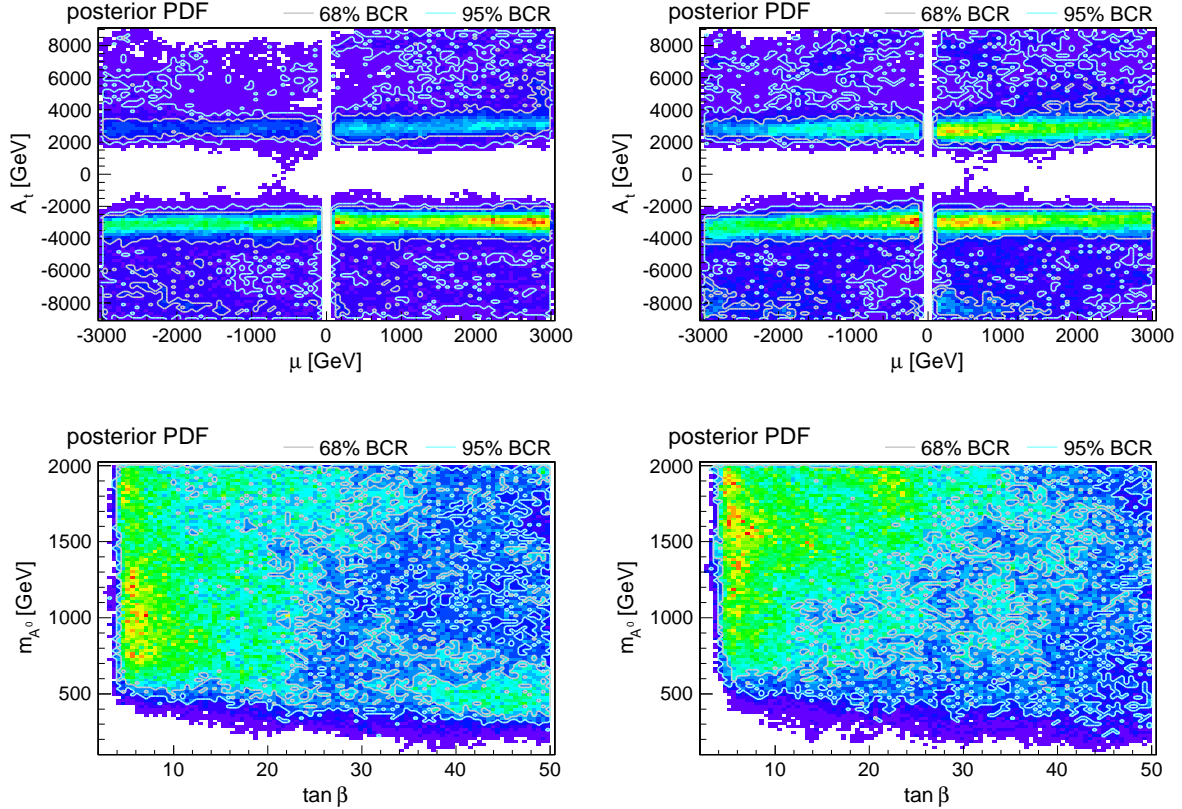

Figure 11.8: Marginalised 2D posterior PDFs as a function of some pMSSM input parameters, taking $\mathrm{BR}(\overline{B} \to X_s\gamma)$ from SuperIso (left column) or from SusyBSG (right column). The 68% (95%) Bayesian credible regions (BCR) are shown in grey (cyan).

At last we show in Figure 11.9 the influences on the marginalised 1D posterior PDFs of some sparticle and Higgs masses, taking $\mathrm{BR}(\overline{B} \to X_s\gamma)$ from SuperIso (blue) or from SusyBSG (green). One can see that the mass predictions are in good agreement with each other, except for the Higgs masses. As already mentioned in the interpretation of Figure 11.7, these discrepancies in the mass predictions for the Higgses $H^\pm$ and H^0 (both $\sim m_{A^0}$) are likely due to different levels of accuracy in the implementation of the charged Higgs contributions.
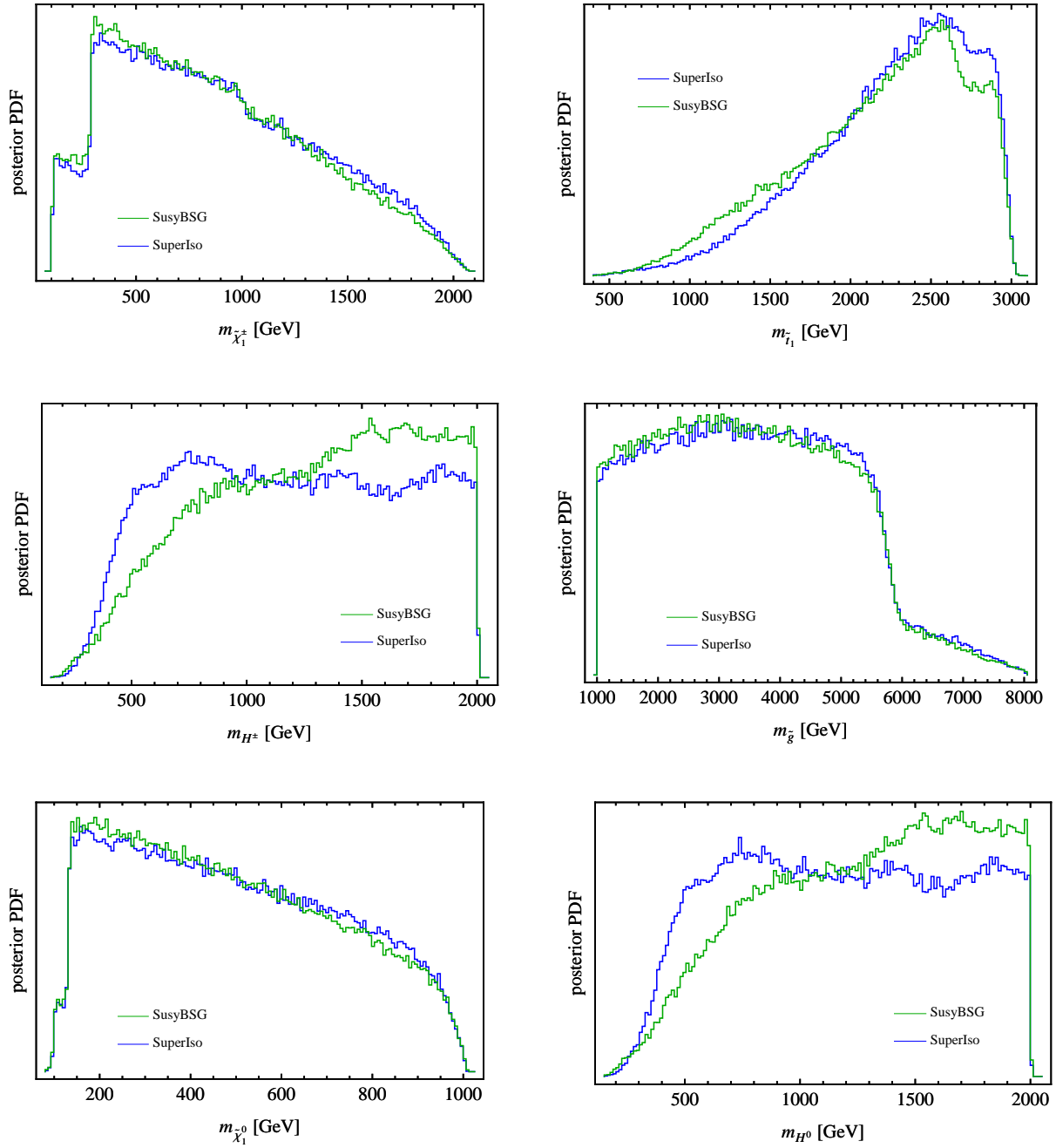
Figure 11.9: Marginalised 1D posterior PDFs as a function of some sparticle and Higgs masses, using $\mathrm{BR}(\overline{B} \to X_s \gamma)$ from `SuperIso` (blue) or from `SusyBSG` (green).

11.3   Conclusions

The rare decay $\overline{B} \to X_s\gamma$ is a sensitive probe for the flavour structure of the SM and beyond and is thus often used as an important constraint for global fits on SUSY models and for general studies of the MSSM. A good assessment of the theoretical and computational uncertainties of this process is therefore very important. In this work we studied these uncertainties and their impact on SUSY fits by way of a detailed comparison of the public $\mathrm{BR}(\overline{B} \to X_s\gamma)$ codes `SuperIso`, `SusyBSG`, `SPheno`, and `micrOMEGAs`. For this we employed two numerical studies in the reduced pMSSM parameter space to assess the following aspects: an in-depth comparison of $\mathrm{BR}(\overline{B} \to X_s\gamma)_{\mathrm{MSSM}}$ via a random scan, and the impact on SUSY fits by way of a global Bayesian analysis using Markov Chain Monte Carlo (MCMC) techniques.

The SM predictions $\mathrm{BR}(\overline{B} \to X_s\gamma)_{\mathrm{SM}}$ of all programs show a notable discrepancy ranging from 2.98 to 3.28×10^{-4} with a relative difference of 9.5%. These differences are mainly due to different hadronic parameters.

When comparing the MSSM predictions $\mathrm{BR}(\overline{B} \to X_s\gamma)_{\mathrm{MSSM}}$ of all programs in our random scan we obtain relative differences Δ_{MSSM} with a maximum at 10.3% and 68% (95%) probability intervals at $[8.1, 13.1]\%$ $([5.1, 24.5]\%)$. However, when comparing the SUSY-only contributions via $\Delta_{\mathrm{MSSM/SM}}$ the maximum is at 2.7% and the 68% (95%) probability intervals are $[1.3, 6.9]\%$ $([0.7, 19.5]\%)$. This better agreement is expected since the discrepancies in the $\mathrm{BR}(\overline{B} \to X_s\gamma)_{\mathrm{SM}}$ predictions are quite large.

Comparing the different $\mathrm{BR}(\overline{B} \to X_s\gamma)_{\mathrm{MSSM}}$ predictions of all programs as a function of the pMSSM input parameters and some sparticle and Higgs masses confirm that larger contributions indeed lead to larger discrepancies. This can be clearly seen from the main contributions (i.e. chargino/stop loops and charged Higgs/top loops, with corrections from gluinos) which become larger for lighter masses and larger $\tan\beta$.

When comparing two codes at a time we obtain good agreement between `SuperIso` and `SusyBSG` since these two programs employ dedicated and up-to-date routines. The associated $\Delta_{\mathrm{MSSM/SM}}$ probability histogram has a maximum at 2.2% and the 68% (95%) probability intervals are $[0.2, 4.2]\%$ $([-4.6, 7.8]\%)$. When comparing `SuperIso` with the other codes the agreement is reasonably good but slightly worse.

We studied the influence of these $\mathrm{BR}(\overline{B} \to X_s\gamma)$ uncertainties on global SUSY fits by performing two MCMC scans contrasting `SuperIso` with `SusyBSG` and comparing the resulting posterior probability density functions (PDFs) of parameters and derived observables. We observe differing posterior PDF predictions for the input parameters m_{A^0}, A_t and μ. However, only m_{A^0} affects the prediction of the mass spectrum with different probabilities for $m_{H^\pm}$ and m_{H^0}. This discrepancy may be related to the fact that `SuperIso` and `SusyBSG` are not at the same order for the charged Higgs contributions.

The impact on SUSY fits is thus rather small since both programs employ similar routines. However, when comparing programs with more differing routines results in a larger influence of $\mathrm{BR}(\overline{B} \to X_s\gamma)$ uncertainties on these fits. We thus conclude that for SUSY fits it is important to use a program that calculates not only the SUSY but certainly also the SM part of $\mathrm{BR}(\overline{B} \to X_s\gamma)$ as precisely as possible.

Appendix A

Contributions to $\tilde{g} \rightarrow \tilde{u}_i \, \bar{u}_g$

Here we specify the complete list of all processes at full one-loop level contributing to the exemplary $\tilde{g} \rightarrow \tilde{u}_i \, \bar{u}_g$ decay which we calculated in detail in Section 6.2.
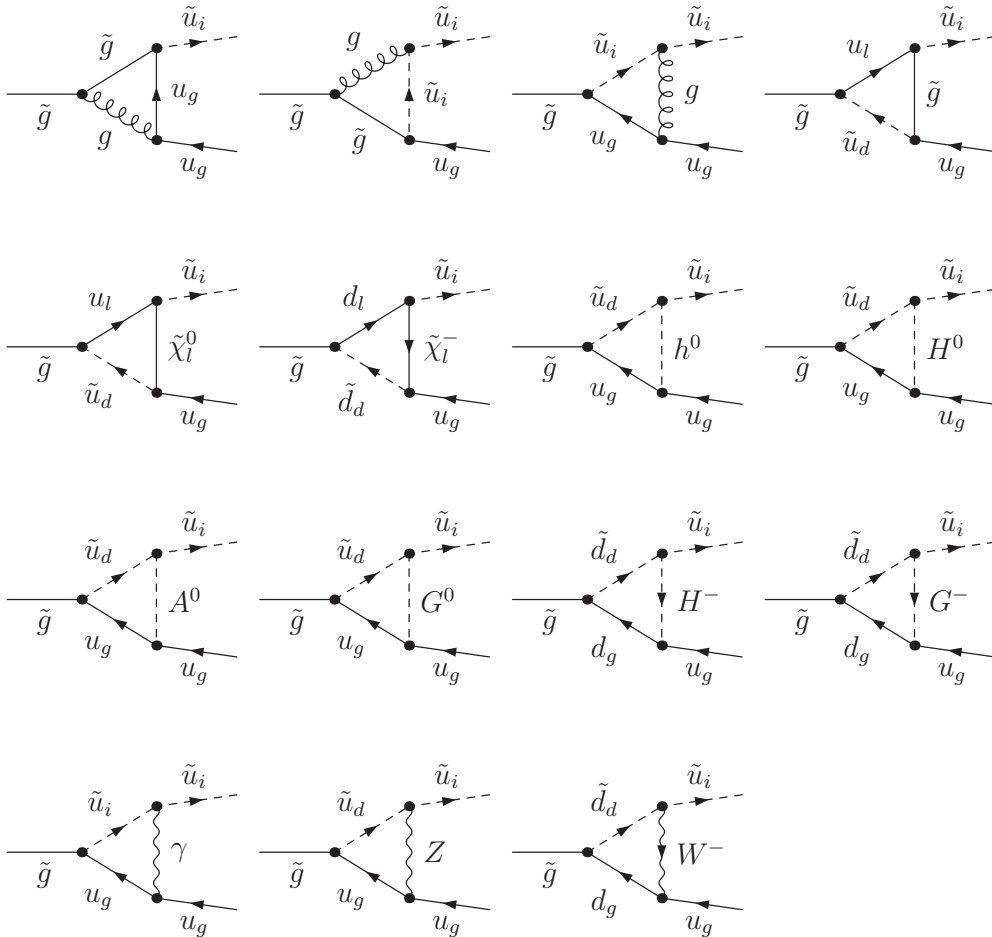

Figure A.1: All vertex contributions to the $\tilde{g} \rightarrow \tilde{u}_i \, \bar{u}_g$ decay. The first row contains the contributions from SQCD only, whereas the remaining diagrams are due to electroweak corrections.
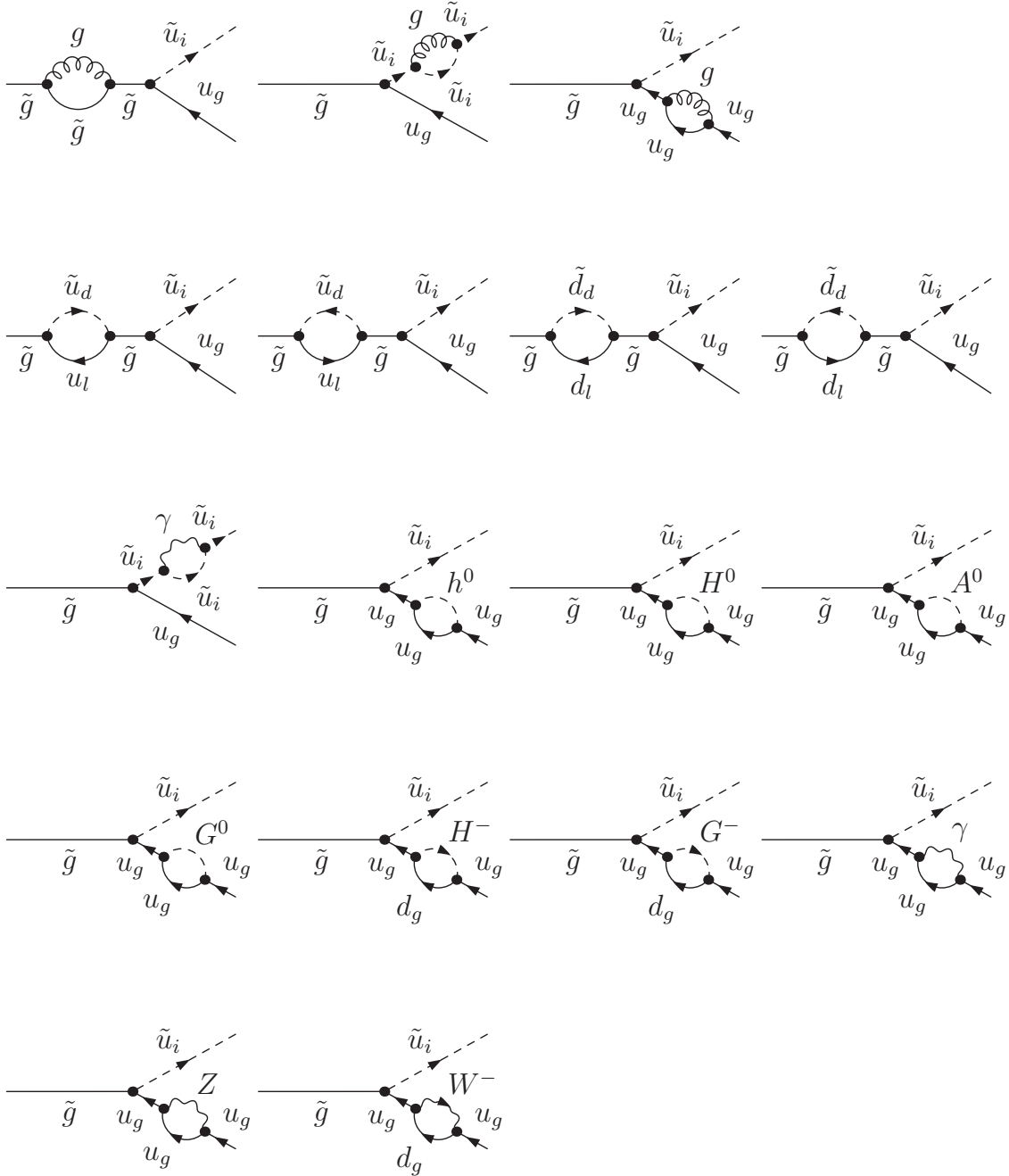
Figure A.2: All diagrams which are needed to calculate all contributions to the $\tilde{g} \to \tilde{u}_i \bar{u}_g$ decay coming from diagonal wave function corrections. The first row contains the SQCD contributions and the remainder contains the electroweak corrections.
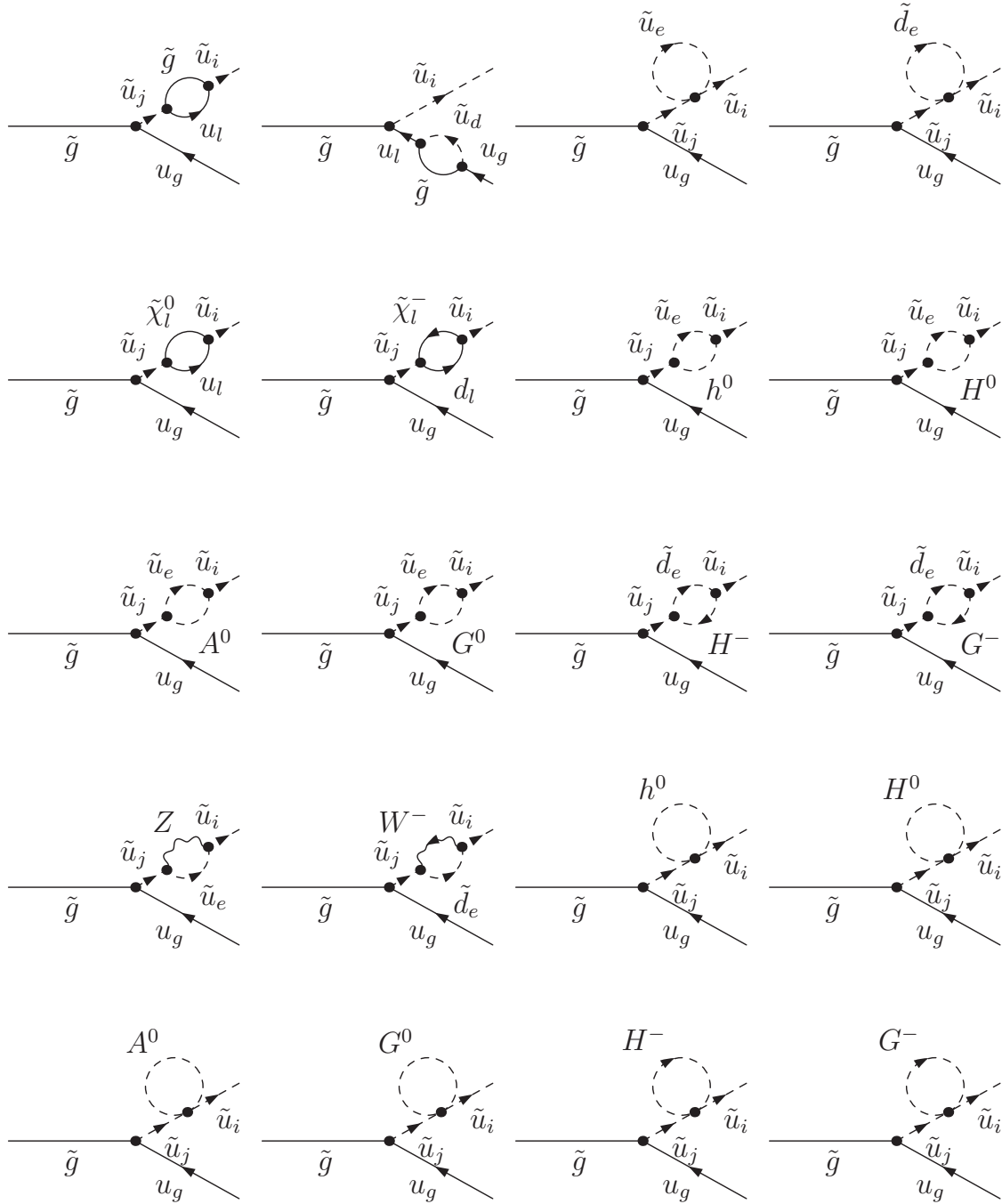
Figure A.3: All 'transition' diagrams which are used to obtain all contributions to the $\tilde{g} \rightarrow \tilde{u}_i \, \bar{u}_g$ decay coming from off-diagonal wave function corrections. The first row contains the SQCD contributions (including the two graphs with four vertices having both SQCD and electroweak couplings) and the remainder contains the electroweak corrections (Part 1).
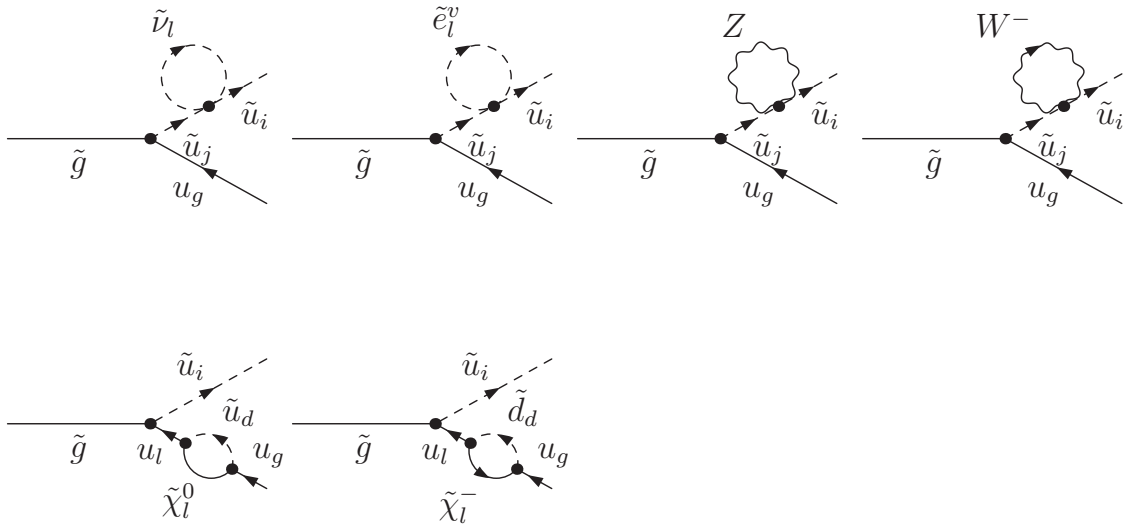
Figure A.4: All 'transition' diagrams which are used to obtain all contributions to the $\tilde{g} \to \tilde{u}_i \, \bar{u}_g$ decay coming from off-diagonal wave function corrections (Part 2).

Appendix B

Flavour Violating Squark Full One Loop Decays

In this appendix we provide further details about our program package, about the installation procedure and the basic usage, and list our exhaustive checks which ensure the correctness of the results produced by our code.

B.1   Details

Based on our calculations of all squark and gluino two-body decay widths in the MSSM with general quark flavour violation (QFV) presented at length in Chapter 6 we developed the first publicly available program package called FVSFOLD (Flavour Violating Squark Full One Loop Decays) written in Fortran, which computes automatically all above-mentioned QFV decays at full one-loop level.[1] For this purpose we adopted the SPA convention along with the $\overline{\text{DR}}$ renormalisation scheme.

For the generation of parts of our Fortran code we used the tools FeynArts 3.7 (FA) and FormCalc 7.3 (FC), which provide the squared matrix element separately for each decay channel. But after this step many crucial parts for the automatic calculation at full one-loop level are still missing!

First and foremost, since FA/FC initially just provide all vertex corrections of a specific process, all remaining coupling and (diagonal and off-diagonal) wave function corrections which are essential for a UV finite result need to be added in a non-trivial way. We include these missing contributions via our original work and our novel approaches already explained in Section 6.2.2 and 6.2.3. For this task we could build upon our extensive set of original renormalisation constants (RCs) derived and rigorously checked in our group over the past years. However, to include also QFV effects in our two-body decays, we had to generalise our set of RCs to include non-minimal QFV in the squark sector. The updated set of RCs including their derivation can be looked up in Section 5.2. Since we included the calculation of coupling renormalisation corrections

---

[1]Currently all decays into Higgses are calculated at tree-level only. We intend to include full one-loop corrections to these decays in the next release. Since we further considered from the beginning the inclusion of CP violating effects we will incorporate them in a later version.

along with the required RCs we provide a possibility to check if the result is truly UV finite, see the remarks in Section 6.2 and below.

Furthermore, to obtain an IR finite result we include soft and hard photon/gluon bremsstrahlung to our decay widths, based on our original work described in Section 6.2.4 and 6.2.5. For this task we build upon previous work done in our group, work that resulted in the development of the bremsstrahlung code in the program package SFOLD [5][2]. However, since we implemented for the first time QFV gluino decays we had to derive the missing soft and hard bremsstrahlung contributions for this novel decay pattern as detailed in the aforementioned sections.

For the convenient usage of our program package we adopt the widely used SLHA2 [29] format for the input and output files. The input file is read in via the SLHA2 I/O tool SLHALib 2.2 [85] and further processed by self-written routines to correctly translate from the SLHA2 parameter convention to the internal convention used by FA/FC. The output file as well as the output on the screen (properly translated back to the SLHA2 convention) are generated by self-written code.

Finally, for an easy-to-use program which automatically calculates all kinematically allowed decays of a given sparticle, we developed an overall framework which executes all necessary steps from the initialisation and calculation of all RCs and all on-shell masses, the calculation of each decay channel, to the final output of the results. For this purpose we could partly reuse the overall framework of the program package SFOLD.

For the execution of our code we use, in addition to the aforementioned SLHA2 I/O library, the LoopTools 2.7 (LT) library for the evaluation of the Passarino-Veltman one-loop integrals.

We want to emphasise that, although we could reuse some general code pieces from the program SFOLD, our code FVSFOLD has been generated and written completely new to incorporate the more general case of QFV in the squark sector, the novel gluino two-body decays, and many improvements mostly related to the calculation of the off-diagonal wave function corrections and of the whole set of RCs. As a result, FVSFOLD contains automatically the quark flavour conserving (QFC) limit of all squark decays as implemented in SFOLD.

B.2   Installation and basic usage

The latest version of FVSFOLD can be obtained from

<div align="center">www.hephy.at/tools/fvsfold</div>

by downloading the most recent *fvsfold-m.n.tar.gz* file. The archive can be unpacked with *tar -xvzf fvsfold-m.n.tar.gz*. The program itself and its required tools (LoopTools and SLHALib) can be quickly installed and set up following the instructions found in the *README* file.

---

[2]SFOLD is the first publicly available program package for calculating all sfermion two-body decay widths at full one-loop level within the flavour-conserving MSSM which has been developed in our group.

FVSFOLD is controlled via the input file *fvsfold.in*. Apart from defining the SLHA2 input and output file name and the decaying sparticle one can also control the bremsstrahlung and resummation as well as a lower bound on the branching ratios to display.

We provide two exemplary SLHA2 input files named *fvsfold_input_example_1.slha2* and *fvsfold_input_example_2.slha2*, containing the general QFV input parameters of scenario A and scenario B from Chapter 7, respectively. These files each contain a complete, minimal and thus mandatory set of parameters which are read in and used by FVSFOLD. All possible other SLHA2 parameters not used in these files are ignored. The associated SLHA2 output files *fvsfold_output_example_1.slha2* ($\tilde{u}_1$ decay) and *fvsfold_output_example_2.slha2* ($\tilde{g}$ decay) provide a simple check if the installation and operation of FVSFOLD is successful. The results in these files should be identical to the results of the respective calls of FVSFOLD except for small numerical deviations depending on the compiler/platform.

In the main file *fvsfold.F* one can further check for IR and UV convergence of the decay widths as well as define the masses of external and loop particles to be either on-shell or $\overline{\mathrm{DR}}$. Furthermore, the output of the SM and MSSM parameters and mass spectra as well as a simple exclusion limit check can be controlled.

For an UV check one sets the divergence Δ (delta_in) to a very high value (e.g. 10^7 instead of the default zero) and then compares the resulting decay widths with the default case when $\Delta = 0$; the relative differences should not exceed small numerical deviations of $\mathcal{O}(10^{-7})$. Please note that for this check resummation needs to be switched off and the masses of loop particles need to be $\overline{\mathrm{DR}}$.

For an IR check one sets the quadratic regulator mass λ^2 (lambda_in) for the photon/gluon to a very high value (e.g. 10^{30}) and then compares the resulting decay widths with the default case when $\lambda^2 = 1$; the relative differences should again not exceed small numerical deviations. Please note that for this check all masses of both external and loop particles need to be $\overline{\mathrm{DR}}$.

B.3 Checks

We performed rigorous checks to ensure the correctness of our results produced by our code. First and foremost, we successfully checked the SQCD and full one-loop decay widths of all squark and gluino decay channels for UV and IR finiteness (see the previous section) using various QFV parameter points.

For various QFC parameter points we compared all masses as well as the tree-level, SQCD and full one-loop decay widths of all squark decay channels from FVSFOLD with the results from SFOLD 1.2, since FVSFOLD automatically (and non-trivially!) contains the QFC limit of all squark decays as implemented in SFOLD. Both programs are in excellent agreement with each other in the QFC limit.

Furthermore, for the same QFV parameter points as above we directly compared the tree-level decay widths of all squark and gluino two-body decays from SPheno 3.2.3 with our tree-level results using the following modifications: since SPheno improves its tree-level decay width formulas by incorporating one-loop corrections into its rotation matrices, we simply take these effective on-shell rotation matrices from the squark,

neutralino, and chargino sector from SPheno instead of our tree-level rotation matrices in the $\overline{\text{DR}}$ scheme. For even better agreement we also set the on-shell masses of all sparticles in our code to the values obtained from SPheno. This direct comparison can be easily enforced by defining the preprocessor variable *SPHENO_COMPARISON* in the main file *fvsfold.F*. Both programs are in very good agreement with each other.

At last we compared all masses as well as the tree-level, SQCD and full one-loop decay widths of all squark and gluino decay channels from FVSFOLD with the results from SPheno without any modifications. The results and conclusions of this extensive comparison by way of two QFV scenarios can be found in Chapter 7.

Bibliography

[1] A. Bartl *et al.*, Phys.Lett. **B679**, 260 (2009), 0905.0132.

[2] A. Bartl *et al.*, Phys.Lett. **B698**, 380 (2011), 1007.5483.

[3] A. Bartl *et al.*, Int.J.Mod.Phys. **A29**, 1450035 (2014), 1212.4688.

[4] A. Bartl *et al.*, Phys.Rev. **D84**, 115026 (2011), 1107.2775.

[5] H. Hlucha, H. Eberl, and W. Frisch, Comput.Phys.Commun. **183**, 2307 (2012), 1104.2151.

[6] W. Frisch, H. Eberl, and H. Hlucha, Comput.Phys.Commun. **182**, 2219 (2011), 1012.5025.

[7] T. Hahn, Comput.Phys.Commun. **140**, 418 (2001), hep-ph/0012260, http://www.feynarts.de/.

[8] T. Fritzsche, T. Hahn, S. Heinemeyer, H. Rzehak, and C. Schappacher, (2013), 1309.1692.

[9] T. Hahn and M. Perez-Victoria, Comput.Phys.Commun. **118**, 153 (1999), hep-ph/9807565, http://www.feynarts.de/.

[10] M. Jimbo *et al.*, (2010), 1006.3491.

[11] K. Iizuka *et al.*, PoS **RADCOR2009**, 068 (2010), 1001.2800.

[12] N. Baro, F. Boudjema, and A. Semenov, Phys.Rev. **D78**, 115003 (2008), 0807.4668.

[13] N. Baro and F. Boudjema, Phys.Rev. **D80**, 076010 (2009), 0906.1665.

[14] S. L. Glashow, Nucl. Phys. **22**, 579 (1961).

[15] S. Weinberg, Phys. Rev. Lett. **19**, 1264 (1967).

[16] A. Salam, *Elementary Particle Theory* (Almqvist and Wiksell, 1969), p. 367.

[17] CMS Collaboration, S. Chatrchyan *et al.*, Phys.Lett. **B716**, 30 (2012), 1207.7235.

[18] ATLAS Collaboration, G. Aad *et al.*, Phys.Lett. **B716**, 1 (2012), 1207.7214.

[19] CMS Collaboration, S. Chatrchyan *et al.*, (2014), 1401.6527.

[20] CMS Collaboration, S. Chatrchyan *et al.*, (2014), 1401.5041.

[21] CMS Collaboration, S. Chatrchyan *et al.*, (2013), 1312.5353.

[22] CMS Collaboration, S. Chatrchyan *et al.*, JHEP **1401**, 096 (2014), 1312.1129.

[23] Particle Data Group, J. Beringer *et al.*, Phys.Rev. **D86**, 010001 (2012), and 2013 partial update for the 2014 edition.

[24] D. J. H. Chung *et al.*, Phys. Rept. **407**, 1 (2005), hep-ph/0312378.

[25] W. J. Marciano, in *Proceedings of the Eighth Workshop on Grand Unification, 16-18 April 1987, Syracuse University, Syracuse, NY*, edited by K. Wali, pp. 185–189, World Scientific, Singapore, 1988.

[26] S. Frank, CP Violating Asymmetries Induced by Supersymmetry, Master's thesis, Johannes Kepler University Linz, 2008, 0909.3969.

[27] S. P. Martin, (1997), hep-ph/9709356.

[28] J. Wess and B. Zumino, Nucl.Phys. B **70**, 39 (1974).

[29] B. Allanach *et al.*, Comput.Phys.Commun. **180**, 8 (2009), 0801.0045.

[30] W. Siegel, Phys.Lett. **B84**, 193 (1979).

[31] G. Passarino and M. Veltman, Nucl.Phys. **B160**, 151 (1979).

[32] A. Denner, Fortsch.Phys. **41**, 307 (1993), 0709.1075.

[33] H. Eberl, *Strahlungskorrekturen im minimalen supersymmetrischen Standardmodell*, PhD thesis, Vienna University of Technology, 1998, http://permalink.obvsg.at/AC02520918.

[34] M. Srednicki, *Quantum Field Theory* (Cambridge University Press, 2011).

[35] H. Hlucha, *Two-body sfermion decays at full one-loop level within the MSSM*, PhD thesis, University of Vienna, 2011, http://ubdata.univie.ac.at/AC09020985.

[36] J. A. Aguilar-Saavedra *et al.*, Eur.Phys.J. **C46**, 43 (2006), hep-ph/0511344.

[37] G. 't Hooft and M. Veltman, Nucl.Phys. **B153**, 365 (1979).

[38] W. Porod, Comput. Phys. Commun. **153**, 275 (2003), hep-ph/0301101.

[39] W. Porod and F. Staub, (2011), 1104.1573.

[40] SSP (SARAH Scan and Plot), http://sarah.hepforge.org/SSP.html.

[41] D. M. Pierce, J. A. Bagger, K. T. Matchev, and R.-j. Zhang, Nucl.Phys. **B491**, 3 (1997), hep-ph/9606211.

[42] M. Antonelli *et al.*, Phys.Rept. **494**, 197 (2010), 0907.5386.

[43] F. Mahmoudi, Habilitation Clermont-Ferrand U. (2012).

[44] Heavy Flavor Averaging Group, Y. Amhis *et al.*, (2012), 1207.1158, online update at http://www.slac.stanford.edu/xorg/hfag.

[45] M. Misiak *et al.*, Phys.Rev.Lett. **98**, 022002 (2007), hep-ph/0609232.

[46] P. Gambino and P. Giordano, Phys.Lett. **B669**, 69 (2008), 0805.0271.

[47] C. Strege *et al.*, JCAP **1304**, 013 (2013), 1212.2636.

[48] J. R. Espinosa, C. Grojean, V. Sanz, and M. Trott, JHEP **1212**, 077 (2012), 1207.7355.

[49] O. Buchmueller *et al.*, Eur.Phys.J. **C72**, 2243 (2012), 1207.7315.

[50] P. Bechtle *et al.*, JHEP **1206**, 098 (2012), 1204.4199.

[51] S. Sekmen *et al.*, JHEP **1202**, 075 (2012), 1109.5119.

[52] S. S. AbdusSalam, B. C. Allanach, F. Quevedo, F. Feroz, and M. Hobson, Phys.Rev. **D81**, 095012 (2010), 0904.2548.

[53] J. A. Conley, J. S. Gainer, J. L. Hewett, M. P. Le, and T. G. Rizzo, Eur.Phys.J. **C71**, 1697 (2011), 1009.2539.

[54] M. Cahill-Rowley, J. Hewett, A. Ismail, and T. Rizzo, (2013), 1307.8444.

[55] A. Arbey, M. Battaglia, A. Djouadi, F. Mahmoudi, and J. Quevillon, Phys.Lett. **B708**, 162 (2012), 1112.3028.

[56] A. Arbey, M. Battaglia, A. Djouadi, and F. Mahmoudi, Phys.Lett. **B720**, 153 (2013), 1211.4004.

[57] C. Bobeth, M. Misiak, and J. Urban, Nucl.Phys. **B574**, 291 (2000), hep-ph/9910220.

[58] M. Misiak and M. Steinhauser, Nucl.Phys. **B683**, 277 (2004), hep-ph/0401041.

[59] M. Gorbahn and U. Haisch, Nucl.Phys. **B713**, 291 (2005), hep-ph/0411071.

[60] M. Gorbahn, U. Haisch, and M. Misiak, Phys.Rev.Lett. **95**, 102004 (2005), hep-ph/0504194.

[61] M. Czakon, U. Haisch, and M. Misiak, JHEP **0703**, 008 (2007), hep-ph/0612329.

[62] A. J. Buras, A. Czarnecki, M. Misiak, and J. Urban, Nucl.Phys. **B631**, 219 (2002), hep-ph/0203135.

[63] M. Misiak and M. Steinhauser, Nucl.Phys. **B764**, 62 (2007), hep-ph/0609241.

[64] M. Ciuchini, G. Degrassi, P. Gambino, and G. Giudice, Nucl.Phys. **B534**, 3 (1998), hep-ph/9806308.

[65] C. Bobeth, M. Misiak, and J. Urban, Nucl.Phys. **B567**, 153 (2000), hep-ph/9904413.

[66] G. Degrassi, P. Gambino, and G. Giudice, JHEP **0012**, 009 (2000), hep-ph/0009337.

[67] M. S. Carena, D. Garcia, U. Nierste, and C. E. Wagner, Phys.Lett. **B499**, 141 (2001), hep-ph/0010003.

[68] G. D'Ambrosio, G. Giudice, G. Isidori, and A. Strumia, Nucl.Phys. **B645**, 155 (2002), hep-ph/0207036.

[69] G. Degrassi, P. Gambino, and P. Slavich, Phys.Lett. **B635**, 335 (2006), hep-ph/0601135.

[70] F. Mahmoudi, Comput.Phys.Commun. **180**, 1579 (2009), 0808.3144.

[71] F. Mahmoudi, Comput.Phys.Commun. **178**, 745 (2008), 0710.2067.

[72] G. Degrassi, P. Gambino, and P. Slavich, Comput.Phys.Commun. **179**, 759 (2008), 0712.3265, up-to-date user manual at http://slavich.web.cern.ch/slavich/susybsg/home.html.

[73] G. Belanger, F. Boudjema, A. Pukhov, and A. Semenov, (2013), 1305.0237.

[74] M. Ciuchini, G. Degrassi, P. Gambino, and G. Giudice, Nucl.Phys. **B527**, 21 (1998), hep-ph/9710335.

[75] T. Becher and M. Neubert, Phys.Rev.Lett. **98**, 022003 (2007), hep-ph/0610067.

[76] G. Belanger, F. Boudjema, A. Pukhov, and A. Semenov, The micrOMEGAs user's manual, version 3.0, online manual at http://lapth.cnrs.fr/micromegas/.

[77] G. Belanger, F. Boudjema, A. Pukhov, and A. Semenov, Comput.Phys.Commun. **174**, 577 (2006), hep-ph/0405253.

[78] A. L. Kagan and M. Neubert, Eur.Phys.J. **C7**, 5 (1999), hep-ph/9805303.

[79] T. Hermann, M. Misiak, and M. Steinhauser, JHEP **1211**, 036 (2012), 1208.2788.

[80] C. Bobeth, A. J. Buras, and T. Ewerth, Nucl.Phys. **B713**, 522 (2005), hep-ph/0409293.

[81] E. Lunghi and J. Matias, JHEP **0704**, 058 (2007), hep-ph/0612166.

[82] C. Bobeth, A. J. Buras, F. Kruger, and J. Urban, Nucl.Phys. **B630**, 87 (2002), hep-ph/0112305.

[83] S. Baek, T. Goto, Y. Okada, and K.-i. Okumura, Phys.Rev. **D64**, 095001 (2001), hep-ph/0104146.

[84] P. Z. Skands *et al.*, JHEP **0407**, 036 (2004), hep-ph/0311123.

[85] T. Hahn, Comput.Phys.Commun. **180**, 1681 (2009), hep-ph/0605049.

[86] CMS Collaboration, CMS-PAS-HIG-13-005 (2013).

[87] R. Trotta, Contemp.Phys. **49**, 71 (2008), 0803.4089.

[88] L. Demortier, S. Jain, and H. B. Prosper, Phys.Rev. **D82**, 034002 (2010), 1002.1111.

[89] D. Gamerman and H. F. Lopes, *Markov Chain Monte Carlo: Stochastic Simulation for Bayesian Inference* (Chapman and Hall/CRC, 2006).

[90] S. Brooks, A. Gelman, G. Jones, and X.-L. Meng, editors, *Handbook of Markov Chain Monte Carlo* (Chapman and Hall/CRC, 2011).

Curriculum Vitae

DI Sebastian Frank

Beatrixgasse 5/17

1030 Vienna, Austria

E-mail: sebastian.frank@gmail.com

Personal Data

Date/Place of Birth	September 27, 1978
	Innsbruck, Austria
Nationality	Austrian
Marital Status	Married

Education

12/2008 — 06/2014	Doctoral studies in natural sciences,
	Technical University Vienna
	Dissertation at the Institute of High Energy Physics,
	Austrian Academy of Sciences
10/1999 — 06/2008	Diploma studies in technical physics,
	Johannes Kepler University Linz
	Diploma thesis at the Institute of High Energy Physics
	Wilhelm-Macke-Award 2009 for the best diploma thesis
09/2003 — 02/2004	ERASMUS exchange semester,
	University of Granada, Spain

10/1997 — 06/1998	Diploma studies in computer science, Johannes Kepler University Linz
09/1989 — 06/1997	Bundesrealgymnasium Sillgasse, Innsbruck

Conference Attendances (selection)

09/2012	Talk given at ÖPG Jahrestagung 2012, Graz, Austria
08/2011	Talk given at SUSY11, Fermilab, Batavia, USA
08/2010	SUSY10, Bonn, Germany
06/2009	Talk given at SUSY09, Boston, USA
07/2008	TOOLS 2008, Munich, Germany

Commitments

10/2004 — 06/2005	Tutor for lectures General Physics 1 and 2
07/2001 — 06/2003	Chairman of the physics students representation Austrian National Union of Students (ÖH)

Skills

Languages	German (native), English (fluent), Turkish (advanced), Spanish (basic), French (basic)
Computer	Very good knowledge of Windows, Mac OS X, Linux, various programming languages (Fortran, Mathematica, MATLAB, C/C++, PHP/mySQL, …)

Interests

Photography, Reading, Traveling, Trekking